Lawrence Berkeley National Laboratory

Title
CHARMED MESON PRODUCTION BY e+e- ANNIHILATION

Permalink
https://escholarship.org/uc/item/5sj3w8rp

Author
Wiss, J.E.

Publication Date
1977-08-01

Charmed Meson Production by e⁺e⁻ Annihilation

James Ernest Wiss
Lawrence Berkeley Laboratory
University of California
Berkeley, California 94720

August 1977

Charmed Meson Production by e^+e^- Annihilation

James Ernest Wiss

ABSTRACT

Compelling evidence will be presented for the production of the lying (D^0, D^+) isodoublet of charmed mesons by e^+e^- annihilation. A study of the recoil mass spectra against these mesons reveals the presence of more massive charmed states, the D^{*0} and D^{*+}, produced in association with the D isodoublet. Mass values and upper limits on the width of the D and D^* are established, and the branching fractions for several D^* decay modes are obtained. An analysis of the production and decay angular distributions shows that the D is probably a pseudo-scalar state and the D^* is probably a vector. Finally, upper limits are obtained for $D^0-\bar{D}^0$ mixing.

ACKNOWLEDGEMENTS

this thesis. Professor George Trilling has taken considerable interest in all aspects of my research and has made numerous useful suggestions. Professor Roy Schwitters has also worked on the D^0, D^+ momentum spectrum and is responsible for several ideas and results described in Chapter 8. Professor J.D. Jackson originally worked out the angular distributions used in the spin analysis and thus provided the inspiration for this work. Professor Mahiko Suzuki also provided wise theoretical council on certain aspects of the work described in this thesis.

It gives me particular pleasure to acknowlege the advice, friend-ship, and assistance of my fellow graduate students , Dr. John Zipse, Susan Cooper, and Dr. Dan Scharre. Thanks a lot gang !

Finally I would like to thank the people who actually helped with the mechanics of getting this work typed and approved. Thanks go to Jeanne Miller who typed this thesis with the patience and spelling acumen necessary to bring it into readable reality. I would also like to thank Professor Gilbert Shapiro and Willy Chinowsky (again) for their rapid reading and useful comments on the contents and style of this work.

Thanks to all.!

TABLE OF CONTENTS

INTRODUCTION

The evidence for the existence of massive, narrow vector mesons
announced in November of 1974 (Augustin 74, Aubert 74, Abrams 74) has
greatly stimulated the high energy physics community during the past three
years. The mystery of the J/ψ (3095) and the ψ' (3684) now appears to be
solved, and a beautiful phenomenology--the spectroscopy of charm--has been
revealed. This thesis will review the evidence for charmed meson produc-
tion by e^+e^- annihilation at SPEAR, and discuss what is now known about
the properties of the SPEAR charmed meson candidates.

We shall begin with a brief discussion of the phenomenology of charmed
mesons emphasizing those characteristics expected for a charmed meson in
the formulation of Glashow, Iliopoulos, Maiani (GIM) (Glashow 70). Evidence for
charm predating the announcement of the SPEAR charmed meson candidates
will then be reviewed, followed by a discussion of the apparatus and
experimental techniques employed in the charm search of the SLAC-LBL
collaboration at SPEAR. Evidence for the existence of narrow, new mesonic
states with masses near 2 GeV/c^2 decaying into $K^\mp \pi^\pm$, $K^\mp \pi^\pm \pi^\pm$, $K^\mp \pi^\pm \pi^+ \pi^-$, and
$K^0 \pi^+ \pi^-$ will then be presented, followed by a discussion of the properties
which identify these new charged and neutral mesons with the predicted
(D^0, D^+) isodoublet of charm. We will then turn to a discussion of
charmed particle phenomena including a study of the recoil spectra
against the new mesons and a discussion of their spin and parity. We
shall conclude by presenting evidence limiting the presence of charm
changing neutral currents.

1. THE PHENOMENOLOGY OF CHARM

We shall explain the concept of charm from the viewpoint of an experimental physicist by reviewing the properties expected for charmed mesons. We begin with a few words concerning the theoretical framework behind the introduction of the charmed quark.

In 1970 Glashow, Iliopoulos, and Maiani (Glashow 70) demonstrated that the inclusion of a fourth quark (c), with the same conventional quantum numbers as the "up" quark (u), would fix a long-standing difficulty with the weak interaction. The application of ideas from spontaneously broken gauge theory to the weak interaction led Weinberg and Salam (Weinberg 67) to the formulation of a unified model for the weak and electromagnetic interaction. It was later shown that their formulation had the hidden, theoretical virtue of being renormalizable--the first renormalizable formulation of the weak interaction. A spectacular prediction of this model is the existence of first order weak neutral currents. The original formulation of their model, in terms of the conventional 3 quarks admitted both strangeness-conserving and strangeness-violating terms offering experimentalists the possibility of seeing neutral current effects without having to perform technically difficult neutrino experiments by searching for such kaon decay modes as: $K_1 \rightarrow \mu^+\mu^-$, $K^+ \rightarrow \pi^+\nu\bar{\nu}$, etc.

The absence of these decays with the rates anticipated for a first order weak process was originally interpreted as evidence against the existence of neutral currents entirely. Because neutral current effects were finally observed in neutrino interactions, the suppression of strangeness changing neutral currents posed a serious problem for the Weinberg-Salam model.

GIM recognized that the inclusion of a new charmed quark would solve this problem by adding a new current able to cancel the strangeness-changing neutral current. Cancellation would only occur if the charmed quark had the same conventional quantum numbers as the up quark (S=0, Q=2/3, B=1/3) and had an additional quantum number (C=1), conserved in strong and electromagnetic interactions, to distinguish it from the up quark. The inclusion of any new quark flavor will spectacularly affect the spectroscopy of the known hadrons by creating a multitude of new hadronic states. Hence in the original GIM formulation the new quark had to be massive enough to avoid upsetting the then-successful 3-quark spectroscopy, but light enough to effect the desired current cancellation. We shall discuss the proper-ties of states containing this quark paired with a conventional $\bar{u}$, $\bar{d}$, or $\bar{s}$ antiquark, i.e. charmed meson states. What should one require of a charmed meson?

A variety of requirements for a charmed meson candidate follow from the presence of an additional conserved quantum number alone. These pro-perties are similar to those which separate the kaon from the pion, which foreshadowed the extension of SU(2) to SU(3) in their time. First of all one expects the lightest charmed members to be hadronically stable and long-lived. If produced with sufficient momentum they might even be expected to leave tracks in an emulsion. At any rate they would give mass distributions compatible with delta functions when analyzed by a conventional spectrometer. In addition, they should be associatively produced by the strong or electromagnetic interaction. They could be produced singly by neutrinos, however.

In light of our knowledge of conventional quarks, one can make the additional observation that a charmed meson, or any new meson containing a new massive quark would appear in an SU(3) triplet consisting of an isodoublet and isosinglet. Throughout this thesis we shall denote the ground state SU(3) charmed meson triplet as D^0, D^+, and F^+ with the latter state being an isosinglet. This charge assignment is determined from the 2/3 charge of the charmed quark. Assuming a meson were found which met these requirements, what more would be expected for a charmed meson--a meson identified with the GIM mechanism?

The unique characteristic of a charmed meson is a preference for the isodoublet states to decay into final states containing single kaons due to the machinations of a $\Delta C = \Delta S$ rule for non-leptonic decays and a $\Delta Q = \Delta S = \Delta C$ rule for semileptonic decays. These rules follow from the structure of the weak current within the GIM model:

$$J^\mu = \bar{u} \, \gamma^\mu (1 + \gamma_5) \, \{d \, \cos\theta_c + s \, \sin\theta_c\}$$

$$+ \bar{c} \, \gamma^\mu (1 + \gamma_5) \, \{s \, \cos\theta_c - d \, \sin\theta_c\}.$$

In the above expression u, d, s, and c are the fields of the up, down, and strange quark, and θ_c is Cabibbo's angle which relates the strength of strangeness-changing and strangeness-conserving semileptonic decays in the conventional, pre-charm theory of weak interactions. This form has the $\gamma^\mu (1 + \gamma_5)$ space-time structure of conventional V-A theories and exhibits Cabibbo quark mixing between the strange and down quark. Because of the "smallness" of Cabibbo's angle ($\tan\theta_c \approx 0.27$), terms proportional to $\cos^2\theta_c$ within the weak Lagrangian: $= (G/\sqrt{2})(J_\mu^\dagger J^\mu + J_\mu J^{\mu\dagger})$ dominate

over mixed terms proportional to $\sin\theta_c \cos\theta_c$ and doubly forbidden terms proportional to $\sin^2\theta_c$. Direct multiplication shows that the Cabibbo enhanced non-leptonic charm-changing Langrangian terms have a flavor structure given by $\bar{c}\,s\,u\,\bar{d}$ or $c\,\bar{s}\,\bar{u}\,d$. This structure implies the selection rules $\Delta C = \Delta S$ and $\Delta I = 1$.

A particularly striking application of the $\Delta C = \Delta S$ rule occurs in the nonleptonic decays of the D^+. Since charm is destroyed in such decays, the $\Delta C = \Delta S$ rule requires the D^+ to decay into states of negative strangeness such as $K^-\pi^+\pi^+$, $K^0\pi^+$, etc. Such $Q = +1$, $S = -1$ final states are exotic. If they were present due to the strong decay of a meson, the meson could not be constructed from a quark-anti-quark pair of the conventional u, d, s quarks. For our two examples, the exotic nature of the final state can be seen from isospin as well. These two decays have $I_z = 3/2$ final states, where as the maximum isospin of a 2-quark meson is 1. Any nonexotic, non-leptonic D^+ decays with single kaons in the final state can be shown to be doubly Cabibbo suppressed and hence rates should be down by a factor of 5×10^{-3} from the exotic decay. Since no experimentally compelling exotic meson candidates exist thus far, the observation of an exotic D^+ decay would provide a striking signal not easily confusable with a conventional K^*.

We see that the content of the GIM paper alone showed that the discovery of charm might be heralded by the appearance of an isodoublet of mesons whose charged member appeared to be a narrow, exotic K^*. The discovery of the Psi particles in November of 1974, and their explanation in terms of charmonia, even told one where to look. We begin with a brief discussion of several facts about the Psi family.
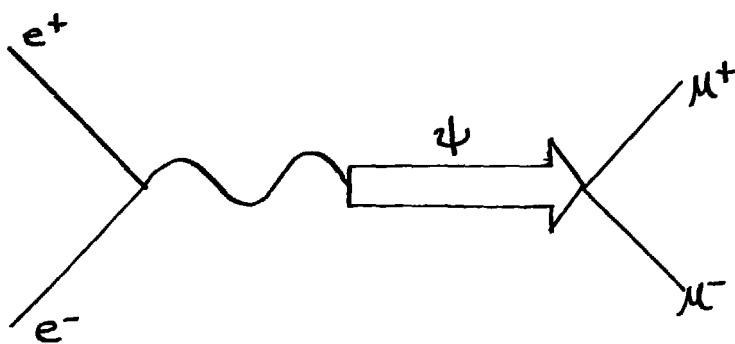
Fig. 1

One photon exchange diagram for ψ production
and subsequent muon pair decay .
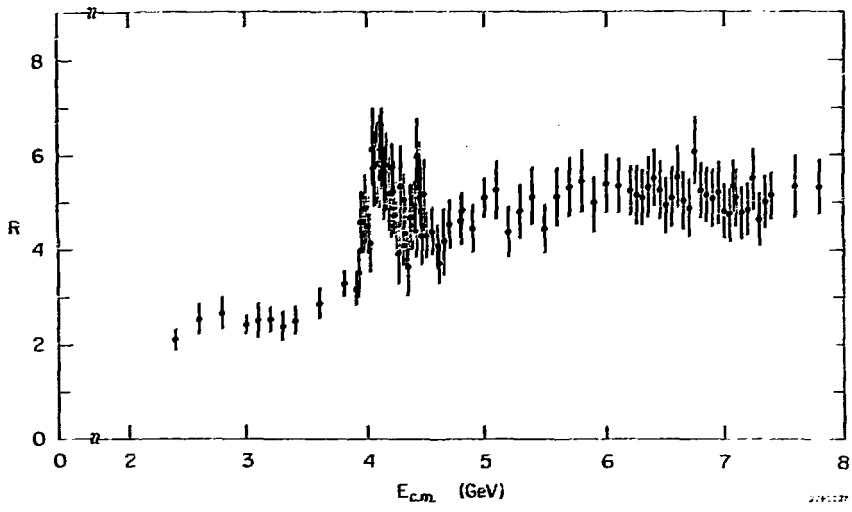
Fig. 2

Plot of R = $\sigma_{Had} / \sigma_{\mu\mu}$ as a function of center-of-mass energy (W) . Not shown are the $\psi(3105)$ and the ψ' (3684) .

The J/ψ (3095) was simultaneously observed in p Be collisions (Aubert 74) and in e^+e^- annihilation (Augustin 74). Fits to the SPEAR e^+e^- annihilation data revealed that the ψ had a total width, Γ, of 69 ± 15 keV, and a width into electron pairs of 4.8 ±.6 keV. Because e^+e^- annihilation is dominated by 1 photon exchange (see Fig. 1), one conjectures that the Psi is a vector meson with photon quantum numbers ($J^{PC} = 1^{--}$). This prejudice was borne out experimentally through the observation of a ψ-photon interference term in μ-pair and e-pair production (Boyarski 75).

A search for additional vector mesons at SPEAR revealed the presence of the ψ' (3684), a broader resonance at 4415 MeV, and considerable--and complicated--resonant structure in the vicinity of $\sqrt{s}$ = 4.1 GeV (see Fig. 2). The ψ' was found to have a total width of Γ = 228 ± 56 keV and a width of 2.1 ± .3 keV into electron or muon pairs. Direct observation of ψ'-photon interference again established the ψ' quantum numbers as $J^{PC} = 1^{--}$. The next highest mass resonance, the ψ(4414), can no longer be considered anomalously narrow. It has a total width of 33 ± 10 MeV and a leptonic pair width of .44 ± .14 keV. (Luth 75)

The property which sets the J/ψ and ψ' apart from the conventional vector mesons, the ρ, ω, and φ, is their very narrow width. The widths of the ρ, ω, and φ are 152, 10, and 4 MeV respectively, whereas the ψ and ψ' have widths on the order of 100 kilovolts. We now believe their narrow width is due to the operation of a phenomenological selection law known as the Okubo-Zweig-Iizuka rule or Zweig's rule for short.

The Zweig rule states that processes involving disconnected quark diagrams are suppressed relative to processes which do not. A disconnected quark diagram is one in which one or more particles can be isolated by
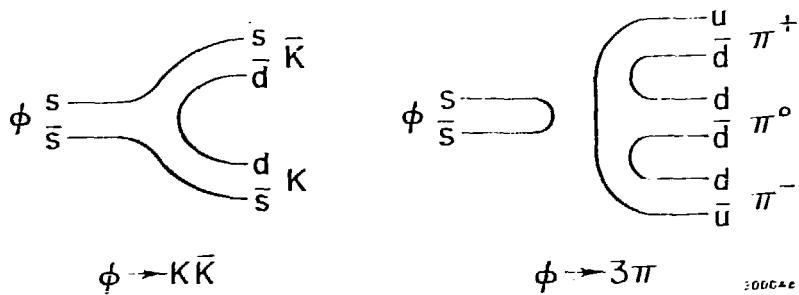
Fig. 3

Illustration of Zweig allowed ($\phi \rightarrow K \bar{K}$)   and
forbidden ($\phi \rightarrow \pi \pi \pi$) decays of the ϕ meson.

drawing a line which does not cross any quark lines. Such a rule was originally invoked to explain the relatively narrow width of the ϕ into 3 π's. The conventional spectroscopic wisdom claims that the ϕ is almost a pure s $\bar{s}$ state, and, as Fig. 3 illustrates, $\phi \rightarrow \pi\pi\pi$ is Zweig suppressed, whereas K $\bar{K}$ is Zweig allowed. Experimentally one does find that K $\bar{K}$ is the dominant ϕ decay mode in spite of the lower phase space, and $\frac{\Gamma(\phi\rightarrow 3\pi)}{\Gamma(\omega\rightarrow 3\pi)}$ = .075 which contradicts phase space arguments as well.

If the ψ and ψ' were comprised of a new quark and antiquark pair (and at the time of their discovery the charmed quark was a likely contender), they too could be anomalously narrow if below the charmed meson pair production threshold. This argument provides a lower limit for the D mass of M_D > 1842 MeV/c^2 (half the width of the ψ'). An upper limit of M_D < 2208 MeV/c^2 can be established through the observation of the broader resonance at 4.415 which is allowed to be broad because it presumably lies above D pair threshold. In light of the complex structure in R = $\sigma_{had}/\sigma\mu\mu$ in the vicinity of the 4.1 (shown in Fig. 2), one might do best looking there for evidence for charmed meson production.

As information on the ψ and ψ' system accumulated, the evidence that the ψ was related to a heavy quark-antiquark bound state mounted. We shall call such an interpretation of the ψ a "charmonium" interpretation, although there is little to link the heavy quark to GIM charm from a study of Psi phenomenology alone. A study of pion multiplicities in ψ decays demonstrated that the ψ has odd G-parity and conserves isospin in its decay. Strong evidence was seen for a p $\bar{p}$ decay mode which demonstrated the isosinglet character of the ψ, expected in a charmonium model.

Although the p p̄ system can couple strongly to an I = 0 or I = 1 resonance, the odd G parity and odd C parity of the ψ shows that the ψ has even isospin and is thus an isosinglet. This last conclusion was corroborated through the observation of a ψ → Λ Λ̄ decay mode. Evidence that the ψ is an SU(3) singlet was provided by the observation that decays of the form ψ → $K_L K_S$ were suppressed relative to analogous decay modes allowed to a C = -1 SU(3) singlet state such as ψ → K K*. (Vanucci 77, Jean-Marie 76)

A particularly striking confirmation of the charmonium picture is the observation of the three well established χ states produced in $e^+ e^-$ annihilation via the chain $e^+ e^-$ → ψ', ψ' → γχ. Three states were found at masses of 3412 ± 3, 3508 ± 4, and 3553 ± 5 MeV/c^2 (Trilling 76). In the charmonium picture one expects a series of c c̄ bound states in analogy with the spectroscopy of positronium. The three observed χ states appear compatible with the $^3P_1$, $^3P_2$, and $^3P_3$ term assignments. Because all three states have been observed in the reaction ψ' → γχ with nearly equal branching ratios of ~7% (Biddick 77), we assume that they have even C-parity. The states at 3412 and 3553 MeV/c^2 are observed to decay into pseudoscalar ππ or KK pairs, thus establishing that they have natural spin parity. Because of the large branching ratio of the ψ' into these states, it is natural to assume the transition is via electric dipole emission; hence all three states have even parity and spins of 2 or less. This means the χ(3412) and χ(3553) have J^P of 0^+ or 2^+. A study of the production angular distribution favors a scalar assignment for the χ(3412). This agreement in quantum numbers for the ^3P states of charmonium provides striking evidence for the validity of the charmonium picture. One has

faith that the 3508 MeV state will be shown to be $J^{PC} = 1^{++}$ in the future and the missing states will be found to complete the picture.

We conclude our discussion of the phenomenology of charm by summarizing the evidence for charmed particle production predating the announcement of the SPEAR charm meson candidates. This material neatly divides itself into evidence provided through the analysis of single events and evidence based on inclusive particle correlations observed in ν interactions.

Perhaps the earliest experimental indication for charmed particle was the appearance of a short (100 μ) gap between a primary and secondary vertex observed within an emulsion exposed to cosmic rays by Niu et al. (Niu 71). The presence of a secondary vertex could be most readily explained as the decay of an ∿2 GeV/c^2 object decaying with proper times on the order of $10^{-12} - 10^{-14}$ seconds. The recent observation of a similar emulsion event in a ν-induced exposure at Fermi National Accelerator Laboratory (Fermilab) has considerably strengthened this earlier, first indication (Cline 77).

The apparent observation of the reaction: $\nu p \rightarrow \mu^- \Lambda^0 \pi^+ \pi^+ \pi^+ \pi^-$ within the Brookhaven National Laboratory (BNL) 15' hydrogen filled bubble chamber provided a particularly well measured example of probable charmed baryon production, although it too was based on one event (Cazzolli 75). This reaction is striking because it violates the well-tested $\Delta S = \Delta Q$ rule for weak interactions and, hence, presumably occurs in two stages: the weak production of a massive new baryon and its subsequent weak decay. Unique mass estimates for the baryon could not be made on the basis of one event since the particle was possibly produced in association with one or more final state pion. Two combinations were found,
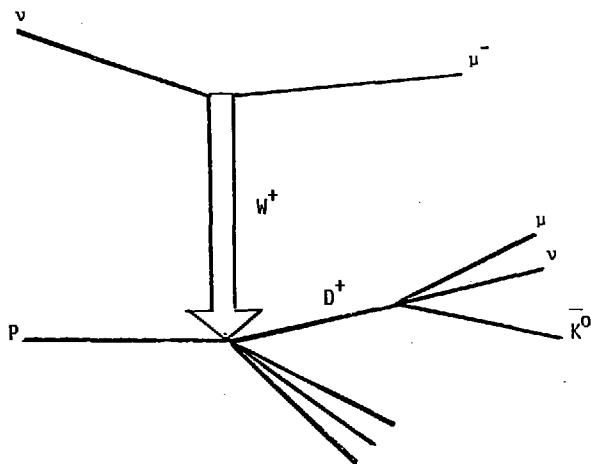
Fig 4

Charmed meson explanation for ν induced

dimuon events .

however, which agreed with charmed baryon mass estimates made by De Rujula, Georgi, and Glashow (De Rujula 76a) using the observed ψ and ψ' masses as a theoretical input. These mass values were later found to be in agreement with the recently discovered charmed baryon candidates observed in an FNAL photoproduction experiment (Knapp 75).

Additional evidence for charm production by neutrinos came from the early observation of neutrino-induced dimuon events produced in FNAL counter experiments (Benvenuti 75, Barish 75). Early studies demonstrated that the two muons tended to have the opposite charge with the μ^- being considerably more energetic than the μ^+ (for an incoming ν rather than $\bar{\nu}$ beam). The μ^+'s were sufficiently energetic, however, to exclude production by conventional sources such as π or K decays.

The observation that $E(\mu^-) > E(\mu^+)$ suggested that the μ^+'s were produced at the hadron-W vertex (see Fig. 4) and presumably represented the decay of a new, massive hadron of mass from 2-4 GeV/c^2. This interpretation was bolstered through the observation of neutrino-induced $\mu^- e^+ \nu^0$ events in heavy liquid bubble chamber exposures at CERN and Fermilab (von Krogh 76, Blietschau 76). As previously discussed, semileptonic decays of charmed particles are expected to result in strange particle production. In addition, dimuons from charmed particle production would be expected to have opposite sign as illustrated in Fig. 4.

We have thus seen that a diversified pattern of experimental observations precedes the discovery of the SPEAR charmed meson candidates. We turn next to a description of the apparatus which made that discovery possible.

2. SPEAR AND THE SPEAR MAGNETIC DETECTOR

The data of this experiment were collected over a 3-year period, from the summer of 1973 to the summer of 1976, by a large collaboration of physicists from the Stanford Linear Accelerator Center (SLAC) and the Lawrence Berkeley Laboratory (LBL) as part of a general survey of high energy electron positron annihilation. The initial goals of this survey were the study of the quantum electrodynamic processes $e^+e^- \rightarrow \mu^+\mu^-$ and $e^+e^- \rightarrow e^+e^-$ in order to investigate the validity of QED at large s and the study of the little understood process: $e^+e^- \rightarrow$ hadrons. Both processes are expected to be dominated by 1γ exchange as illustrated in Fig. 1. Fig. 1 suggests that the study of hadronic production by e^+e^- annihilation will shed light on the constituent structure of elementary particles. Constituent effects should be noticeable for collisions with center-of-mass energies (Ecm) on the order of several GeV's.

In order to obtain such energies with existing technology, it is necessary to employ colliding beams rather than single positron beams against electron targets. Unfortunately one suffers a considerable reduction in luminosity (i.e. the factor multiplying cross section to obtain rate) with colliding beams. This is especially serious for electro-magnetic processes whose cross sections are typically on the order of nanobarns (nb). Storage rings, where many pulses from a conventional accelerator can be stacked into two bunches which collide millions of times per second, enable one to achieve the luminosity necessary to do e^+e^- physics, with the energies necessary to make it interesting.
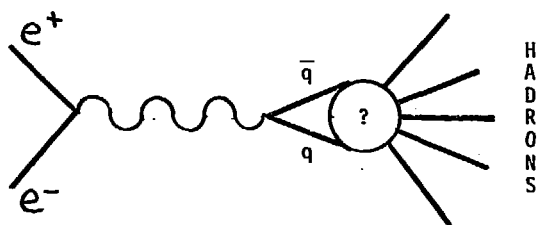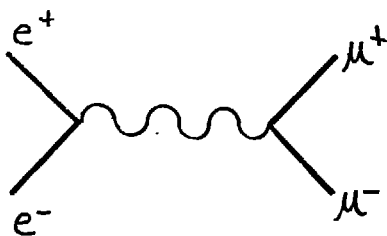
Fig. 1

Illustration of the similarity between hadron production
and muon pair production in the one photon exchange model.

In 1974 the original SPEAR storage ring RF system underwent substantial modification in order to achieve peak luminosity at higher center-of-mass energies. I shall describe the operation of the machine after these modifications, which is relevant operation for the data sample under discussion.

The SPEAR ring is filled with electrons and positrons from the 3-km-long SLAC linear accelerator. Filling generally takes 20 minutes with the luminosity exponentially degrading to about 1/2 over a time period of several hours. The electrons and positrons counter rotate at 1.28 MHz in two bunches, time synchronized to collide in two diametrically opposite intersection regions. Because each beam shares the same magnetic lattice, the beam momenta are equal and opposite to high precision, making the lab system equivalent to the cm system.

The SPEAR Rf system (necessary to pump in the energy lost by the beams to synchrotron radiation) is capable of maintaining center-of-mass energies from $2.5 < E_{cm} < 8$ GeV with a luminosity varying from 10^{-4}- 10^{-2} $\sec^{-1} nb^{-1}$. SPEAR luminosity peaks near $E_{cm} = 7$ GeV and falls quickly as one moves from the peak according to $L = 10^{-2} (E_{cm}/7 \text{ GeV})^4 \sec^{-1} nb^{-1}$ for E_{cm}'s less than 7 GeV. At 7 GeV, muon pairs will be produced with a cross section of 1.8 nb, which, assuming .01 $\sec^{-1} nb^{-1}$ luminosity, gives a rate of .018 events/sec or 1 mu pair per minute. Using the experimental value of $R = \sigma_{had}/\sigma_{\mu\mu} \simeq 6$, one expects 1 produced hadronic event every 10 seconds. Rates are certainly low by strong interaction standards!

The beam profile at either of the two intersection regions is approximately Gaussian in each dimension with $\sigma^x = 1$ mm, $\sigma^y = .1$ mm, $\sigma^z = 50$ mm,

where z is along the positron momentum, and y is the vertical along the ring bending magnet's magnetic field. The spread in z is energy dependent. The value of 50 mm is typical for most of the charm running. The natural energy spread of the beam is due to quantum fluctuations from synchrotron radiation. The energy distribution is expected to be approximately Gaussian with an energy dependent width given by $\sigma_{Ecm}^{synch} = 0.12$ MeV $(Ecm)^2$ where Ecm is measured in GeV.

The center-of-mass energy calibration of the SPEAR ring is conservatively estimated to be good to within ±0.1%. The ring energy is a function of both the geometry of the electron and positron orbit and the strength of the fields present in the ring bending magnets. Magnetic field measurements are obtained with a long flip coil rotating within a reference bending magnet duplicate placed in series with the functioning bending magnets of the ring. The properties of each ring bending magnet were extensively measured prior to installation. For every field measurement made on a ring magnet the same measurement was carried out at the same time on the reference magnet in series with the ring magnet. Hence the magnetic field at any given position in the ring is accessible by a proper measurement of the reference magnet's field. Magnetic measurement by this technique is expected to contribute a relative error of less than 5×10^{-4} to the absolute energy calibration of the ring. This magnetic field error is dominated by uncertainties in the bending magnet fringe fields.

The remaining energy calibration error is due to orbit uncertainties. Deviations of a given orbit from the ring equilibrium orbit is monitored by a set of electrostatic beam position monitors. An absolute measurement of the equilibrium orbit circumference is obtained by measuring the RF
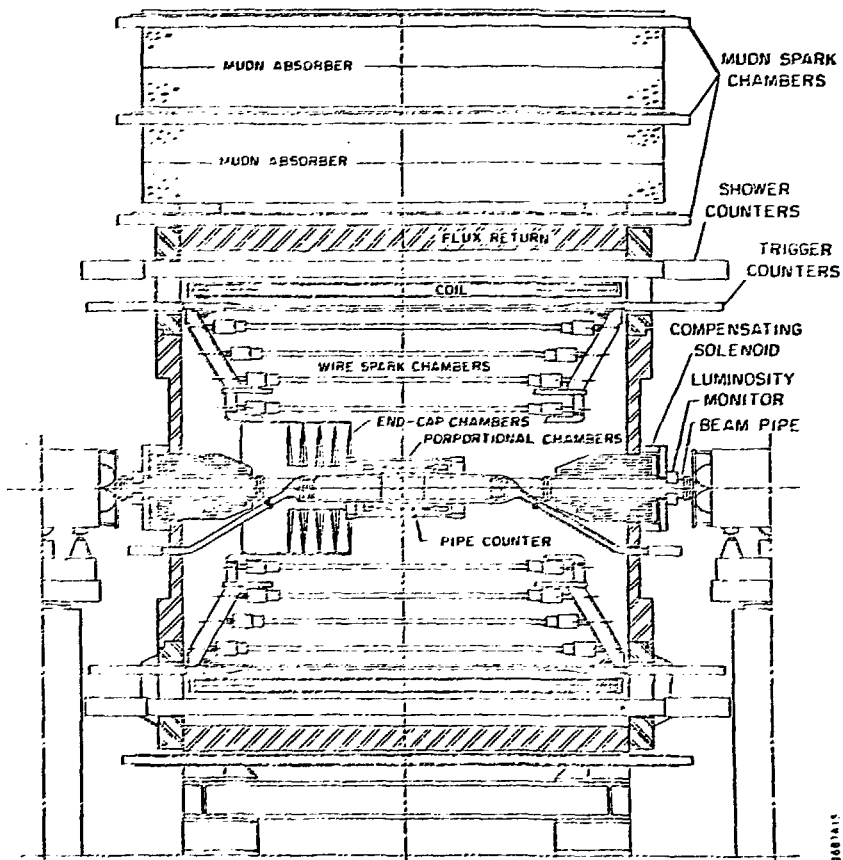
Fig. 2

Diagram of the Mark I   SLAC-LBL
Magnetic Detector.

frequency needed to produce an orbit of minimum distortion from the equili-
brium orbit. The orbit circumference can then be obtained from the speed
of light and the orbit period as determined from the RF frequency.
Circumference measurements obtained through this technique are within
5 mm (out of a total ring circumference of 234 meters) of the design
circumference. The error in energy calibration due to such a ±5 mm
circumference error is ±5 × 10^{-4}.

A. Functional Description of the SPEAR Magnetic Detector

The SPEAR Magnetic Detector is basically a cylindrical array of spark
chambers surrounding the e^+e^- annihilation region concentric with the beam
axis which detects charged particles satisfying $|\cos\theta| \gtrsim .65$ where θ is the
track polar angle with respect to the beam axis. Magnetic momentum analysis
is provided by a solenoid enclosing the cylindrical chambers. The solenoid
provides a nearly uniform 4 kG magnetic field. Time-of-flight particle
identification is provided by a ring of scintillation counters (trigger
counters) just outside the cylindrical spark chambers. Pulse height infor-
mation from a series of lead scintillator shower counter provides some
degree of neutral detection and electron tagging (see Fig. 2). We shall
give a description of the detector components as one travels out from the
beam axis.

After traversing the .15 mm thick corrugated stainless steel vacuum
chamber at 8 cm radius, tracks enter the two .7 cm thick pipe counter
scintillator cylinders at 11 and 13 cm respectively. These counters are
required in the trigger. At 17.3 and 22.4 cm radius a track traverses the

two proportional chambers which cover the polar region of $|\cos\theta| < .83$ and have wire spacings of 2.1 and 2.8 mm respectively. The proportional chamber wires run parallel to the beam axis. At mean radii of 60, 91, 112, and 135 cm, the track traverses the 4 cylindrical wire chambers. Each chamber consists of 2 gaps, one with wires skewed at $\sim\pm2°$ wrt the beam axis, and the other at $\sim\pm4°$. The stereo angle provides information in the z intercept of a track with a given gap. The chambers are constructed of .19 mm diameter aluminum wire spaced 1.1 mm apart. Signals on the wires are read out magnetostrictively using 100 wands. These chambers are supported by a 1.3 cm thick aluminum cylinder outside the outer chamber and by 6 aluminum support posts at a radius of 79 cm.

The major component of the time-of-flight system is a cylindrical array of 48 2.5 cm thick Pilot-Y scintillation counters placed at a 1.5 meter radius. We shall describe the timing system in more detail in a later section. After passing through a 1 radiation length water-cooled solenoidal coil, the tracks penetrate a ring of 24 shower counters consisting of 5 layers of .64 cm thick lead sheets interleaved with .64 cm thick Pilot-F plastic scintillator. This "sandwich" is enclosed in a 1.3 cm thick aluminum box. The shower counters are used in conjunction with adjacent trigger counters as part of the hardwire trigger and provide some electron and photon identification. After traversing a 20 cm thick iron flux return, a track enters a double plane of magnetostrictive spark chambers used to offer π-μ discrimination. Additional π-μ separation is provided over $\sim10\%$ of the solid angle by several additional spark chamber planes interleaved with 5 interaction lengths of concrete.

Storage ring luminosity is monitored by a set of 4 luminosity monitors arranged into 2 small angle counter telescopes placed at ±20 Mrad with respect to the beam axis. Each luminosity monitor consists of a tungsten-scintillator sandwich in back of a solid angle defining scintillation counter. The pulse height of the tungsten-scintillator counter is required to be above a threshold set to discriminate against hadrons and muon pairs in favor of electrons. By demanding a small angle coincidence of back to back pairs, one is monitoring luminosity essentially through the space-like photon exchange Bhabha process $(e^+e^- \rightarrow e^+e^-)$. The luminosity monitors are calibrated from quantum electrodynamics by accumulating large angle Bhabhas and μ pairs with the detector at energies away from known resonances.

B. Momentum Resolution

Two major track fitting algorithms are used in the analysis of data from the SPEAR Magnetic Detector. The single track algorithm (s.t.) finds track parameters which minimize a χ^2 constructed from the closest approach distance of a given track to each of the measured space points. The measured space points are constructed from information from the 2 proportional chambers and 4 wire spark chambers. The track is constructed from a given set of trial track parameters by a 4th order Runge-Kutta integration through the measured field (described by a polynomial with experimentally measured coefficients), and hence is not perfectly helical. The beam constraint algorithm is identical except tracks are assumed to come from the e^+e^- interaction region, and a new point, the beam origin, is added to the χ^2 calculation with appropriate errors. The exact beam
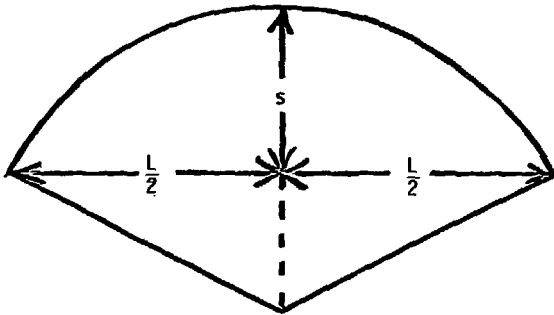
Fig. 3

Illustration of the sagitta (s) of a chord of length L .

origin changes on a run to run basis, but can be computed with sufficient accuracy from a weighted average of closest approach positions of muon pair and Bhabha tracks with respect to a nominal origin.

It is useful to obtain an idealized model for how the momentum resolution of a system like the SPEAR Magnetic Detector depends on such factors as the magnetic field (B), prong transverse momentum ($P_\perp$), and the distance over which a track is measured (L). Ignoring small variations in the detector magnetic field, particles will travel along helical tracks or circles in x-y projection. For high momentum tracks the transverse momentum measurement process can be idealized as the measurement of the sagitta (s) of this circle or the perpendicular excursion of an arc from the straight line of length L, drawn between its end points (illus-trated in Fig. 3). In this model one expects the relative error in trans-verse momentum ($P_\perp$) to equal the relative sagitta error (σ_s) or:

$$\sigma_{P_\perp}/P_\perp = 66.8 \; \sigma_s \; \frac{P_\perp}{L^2}$$

where all linear dimensions are in meters, $P_\perp$ is in GeV/c, and the value 66.8 is appropriate to the 4 kG magnetic field. The effective chord length (L) for the single track fit is 1.18 m, while that for the constrained fit (b.c.) is 1.3 m, which gives for a 4 kG magnetic field $\sigma_{P_\perp}^{s.t} = 48 \; P_\perp^2 \; \sigma_s$ and $\sigma_{P_\perp}^{b.c.} = 37 \; P_\perp^2 \sigma_s$. One obviously does better with the beam constrained fit, but cannot use it for prongs suspected of comprising a K_s, or Λ^0.

Because tracks traverse only 5% of a radiation length of matter while in the tracking fiducial volume, sagitta error is dominated by wand position error rather than by multiple coulomb scattering error for pions with momenta

exceeding 350 MeV/c. One naively expects that sagitta errors are roughly equal to the rms deviations of measured space points from fitted tracks. This latter quantity is determined by many factors including chamber wire spacing, chamber misalignment, and the response of the magnetostrictive read-out system. As a consequence of obtaining the alignment corrections described later in this section, we have observed typical rms deviations in the magnetostrictive spark chamber system of approximately .3 mm after gross misalignment errors are corrected out. In Fig. 4 we show a typical deviation distribution obtained for a sample of muon pair tracks from data taken at the ψ. We have fitted these tracks employing the constraint that they have the momentum appropriate to muon tracks from the ψ. Fig. 4 shows the distribution obtained for the chamber of nominal radius 1.10 m. Superimposed on the histogram is a fitted gaussian resolution function with a linear background term. The fit gives an rms deviation $\sigma = .34 \pm .02$ mm with a centroid shift of $0.03 \pm .02$ mm.

Using this estimate for the sagitta error we estimate:

$$\frac{\sigma_{P_\perp}^{s.t.}}{P_\perp} = 1.6\% \ P_\perp, \ \frac{\sigma_{P_\perp}^{b.c.}}{P_\perp} = 1.3\% \ P_\perp.$$

Although it is experimentally difficult to measure momentum resolution in the momentum region where multiple scattering effects are important, one can naively include these effects in the resolution model by adding a
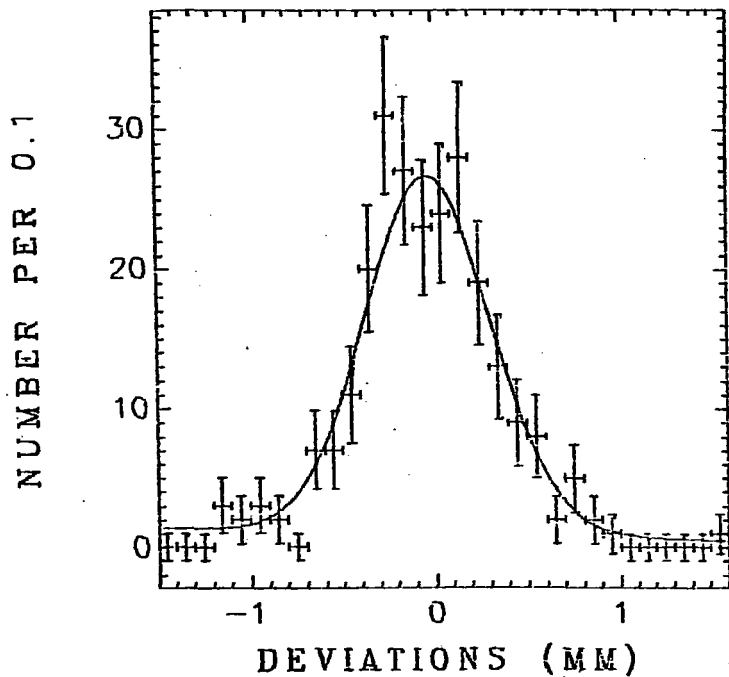
Fig. 4

Deviation distribution for third cylindrical spark chamber. Solid curve is a Gaussian distribution of width $\sigma = 0.34$ mm .
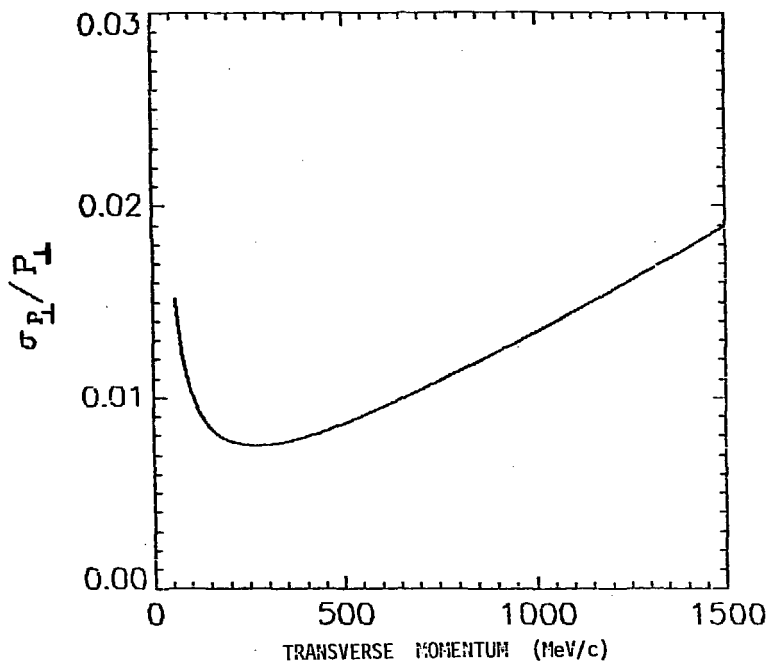
Fig. 5

Momentum resolution of the Spear Magnetic

Detector

sagitta error proportional to the rms coulomb scattering angle in quadrature
to the sagitta error due to position uncertainty. Hence our expression for
the uncertainty in the beam constrained transverse momentum for tracks
traversing all spark chambers is:

$$\frac{\sigma_{P_\perp}^{b.c.}}{P_\perp} = \sqrt{(1.3\% \ P_\perp)^2 + (.6\%)^2(1 + (M/P)^2)}$$

where M is the mass of the track, P is its total momentum, and 0.6% was
chosen to give agreement with Monte Carlo simulations incorporating the
effects of multiple scattering. This function is plotted in Fig. 5.

We turn next to a discussion of the various types of corrections
applied to the data in order to obtain this expected resolution and will
present a simple measurement of the SPEAR Magnetic Detector momentum
resolution using muon pairs from the ψ.

Momentum corrections begin with the determination of 300 alignment
constants used to correct tracks on the space point level. A more complete
description of these constants appears in the thesis of Dr. John Zipse
(Zipse 76). The first 200 of these constants give the azimuthal locations
of the starting and stopping wand fiducials, for the wands used in reading
out the 4 wire chambers. Wand azimuthal location for a spark on a given
wire plane is computed by linearly interpolating the arrival time of the
spark signal relative to the arrival time of the 2 wand fiducial signals.
By arrival times we mean the delay time from the application of the chamber
high voltage pulse to the arrival of the magnetostrictive signal at the
wand sensing coil. The next 74 constants give the orientation and
position of the 16 cylinders (2 cylinders/gap) relative to the magnetic

field centered coordinate system. These constants are followed by 16
constants giving the exact stereo angles of each wire cylinder with
respect to the beam axis. The final 10 constants give the position and
orientation of the 2 proportional chambers relative to the coordinate
system set up by the other constants.

The zero order alignment constants were determined by a survey of the
apparatus upon construction. It soon became obvious, however, that a fine
tuning of the constants was necessary to achieve respectable momentum
resolution. Fine tuning is accomplished in general by an iterative
procedure whereby moments of the deviations of a fitted track from its set
of space points are accumulated and used to compute a modified set of
alignment constants. As iterations proceed, the fitted track becomes
increasingly closer to the actual path of the charged particle through
the detector and the differences between successive sets of alignment
constants will diminish.

One can judge the quality of a given set of alignment constants by
making a scatterplot of momentum divided by beam energy (p/E) for muon
pairs vs. azimuth. It is best to make separate scatter plots for the
positive and negative members of the pair. Relative shift misalignment of
the chambers will create a single cycle, sinasoidal variation in the p/E
vs. θ plot. Relative azimuthal chamber misalignment will shift the positive
particle relative to the negative particle baselines. Wand fiducial misalign-
ment will create sharp local fluctuations in the plot.

The general alignment algorithm works best when one can place
constraints on the tracks used for alignment. For this reason early

alignment work was done with straight, cosmic ray tracks taken with the solenoid off. Unfortunately cosmic rays tend to be vertical and thus offer little information on horizontal chamber alignment. Hence subsequent alignment was performed with back-to-back Bhabha or muon pairs.

These events were fitted as if there were no initial or final state radiation. They were thus assumed to be perfectly back to back in projection (i.e. 0° coplanarity angle) with momenta computed from the SPEAR ring energy. Certainly such assumptions are not technically valid, but they do allow for a considerably improved set of alignment constants as judged from a decrease in azimuthal variation seen in a plot of Bhabha or mu pair momentum vs. azimuth at fixed energy.

Because the coordinates of the beam origin in the magnetic centered coordinate system is a sensitive function of the proportional chamber alignment, it is necessary to determine run-to-run beam origins after tuning the alignment constants. After beam origins are determined, one can finally perform beam constraint and single track fits and write summary (Pass 2) tapes listing the track kinematic parameters.

Separate sets of alignment constants were obtained whenever major structural modifications were made to the magnetic detector by design or accident. Three sets of alignment constants were made: for the period preceeding the installment of the concrete muon identifier, for the period before the fire which destroyed much of the muon system, and for the period after the reconstruction of the system. It is obviously important to determine the alignment constants quickly, near the start of a run cycle, so that Pass 2 processing can begin. For this reason the

alignment constants are often statistics limited, giving less than satis-factory resolution. Hence we make a second level of track correction consisting of an empirical correction to the track momentum as a function of the measured track azimuth. Because these corrections involve only measured quantities, they can be performed with a relatively minor expen-diture in computer time after the bulk of Pass 2 processing is completed.

Mu pair events are used for this purpose. The detector is divided into 36 azimuthal regions and deviations between the expected and measured muon momentum are averaged separately within a given azimuthal region. These averages are used to obtain 36 azimuthal constants Δ^i which are stored on computer files. When analyzing SPEAR data in a summarized format (DST), the user can call a subroutine which automatically corrects the momentum magnitude for all tracks in a given event according to the algorithm:

$$P_{corr} = P_{uncorr} \, (1 + \Delta^i \, P_{uncorr})$$

where "i" is appropriate to the track's azimuthal region. The scaling law implied by this relation is a consequence of believing that this algorithm corrects out systematic sagitta error due to residual chamber or wand mis-alignment.

Muon pair production from the ψ and ψ' has proven quite useful in determining the experimental resolution of the Magnetic Detector. Both resonances are delta functions compared to the mass resolution of the detector, and final state radiation from muons is negligible. One can work out a simple relationship between the mass resolution and the muon momentum resolution by ignoring the μ mass compared to the μ momentum.
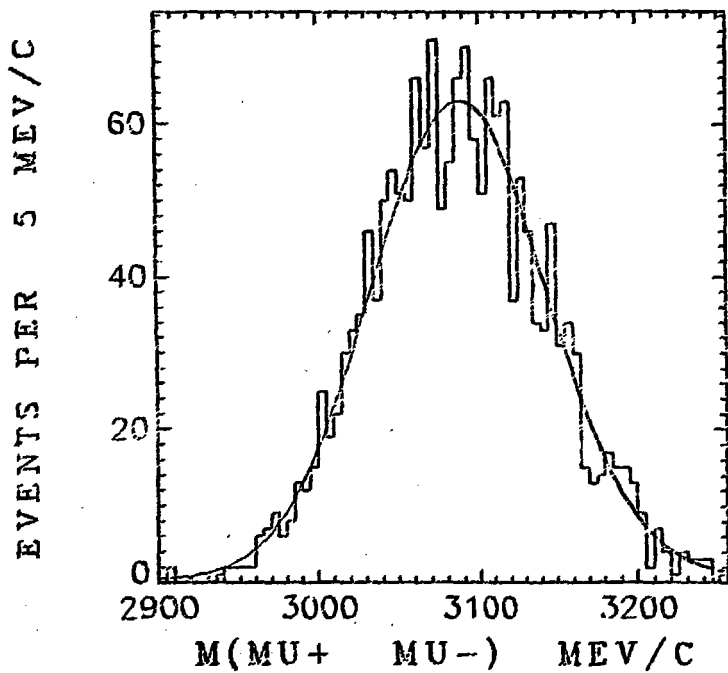
Fig. 6

Muon pair invariant mass histogram for $\psi \rightarrow \mu^+ \mu^-$

The solid curve is a Gaussian of width $\sigma = 54$ MeV/c^2.

In this limit

$$M_\pi = P_{\mu_1} + P_{\mu_2} \quad \text{or} \quad \sigma_{M_\pi} = \sqrt{2}\ \sigma_P.$$

By measuring the muon pair mass resolution, rather than the spread in momentum of either prong, one is ignoring any broadening effects due to initial state radiation or finite beam spread.

Fig 6 shows the invariant mass distribution of muon pairs taken from ψ running. Muon pair candidates are selected from events consisting of 2 prongs of opposite charge which are coplanar within $20°$. Each prong is required to have a momentum exceeding 1/4 of the mass of the ψ and have a lower shower counter pulse height in comparison to the mean pulse height expected for electron pairs of that momentum. We note the momentum requirement on muon prongs could have been tightened up considerably, but backgrounds are quite tolerable with the looser cut. The mass resolution deduced from Fig. 6 is $\sigma_M = 50$ MeV/c^2 which implies $\sigma_p = 36$ MeV/c or $\sigma_p/P = 0.15$ P. This is in excellent agreement with the model described in the previous section. For the purposes of this momentum resolution determination, momenta were obtained from the beam constrained fit corrected for dE/dx loss in the pipe counters and beam pipe.

C. The Time-of-Flight System

A nice description of the hardware aspects of the trigger counter system appears in the thesis of Dr. Scott Whitaker (Whitaker 76). In this section I will give only a brief overview of the timing system and will present several simple measurements of its performance during the acquisition of the "charmed" data sample under discussion.
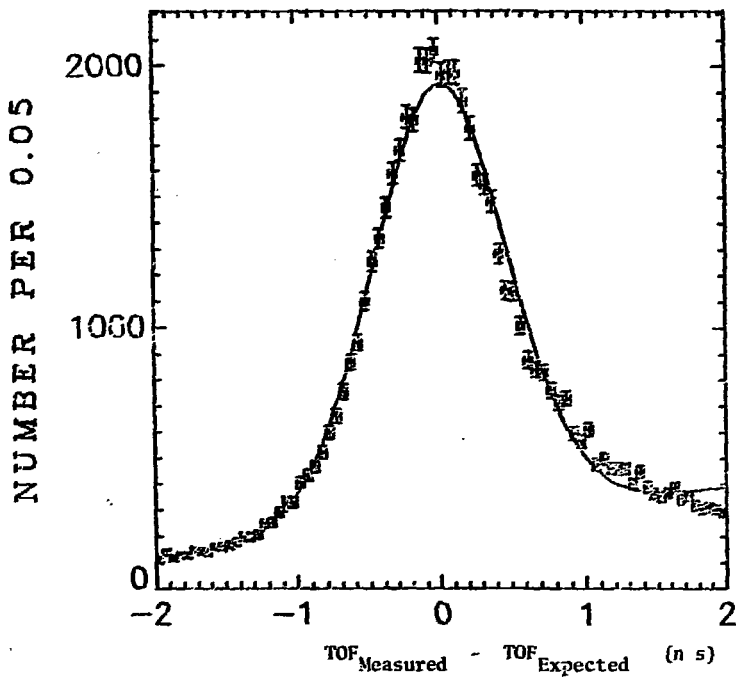
Fig. 7

The difference between the measured and
expected flight times for prongs with momentum
less than 300 MeV/c contained in multibody hadronic
events. Curve is a Gaussian of width $\sigma = 0.47$ ns
over a linear background.

A signal from one of two electrostatic beam pick-up electrodes is used to start the trigger counter TDC's. The beam pick-up signal records the passage of either one of the two 0.3 ns long beam bunches before they collide in the detector center. Each of the 48 trigger counters is viewed on both ends by 2 Amperex 56 DVP photomultiplier tubes. Signals from these photomultipliers, after passing a suitable discriminator threshold, serve to stop the 96 TDC's and provide the basic timing information of the system. A TDC overflow indicates a "no hit" condition for a given trigger counter. Zero order time compensation for the effects of finite light propagation time down the trigger counter is achieved by a simple hardware averaging of the times recorded for each of the two photomultipliers.

Signals from the 96 photomultipliers are also sent to separate ADC's, and pulse height information from each "hit" trigger counter is recorded along with the TDC information. This pulse height information enables one to improve time-of-flight resolution by compensating for "slewing" effects or the tendency for timing signals with large pulse height to prematurely meet the TDC threshold condition. An overall approximate factor of 2 in time resolution was realized due to this innovation on the original Magnetic Detector.

In Fig. 7 we show a fitted histogram of the difference between the measured and expected time-of-flight for prongs with momenta of less than 300 MeV/c. We have computed the expected time-of-flight from the measured prong momentum and calculated flight path assuming that the prong was a pion. These data are from the "charm" running ($3.9 < \sqrt{s} < 4.9$ GeV) which constitutes the data set under discussion throughout this thesis. The fit

in Fig. 7 consists of a gaussian peak over a linear background, with
the background being included to allow for false TDC readings from
multiple hits in a single trigger counter, as well as the kaon tail.
From this fit we obtain a time-of-flight resolution given by $\sigma_{TOF} = 0.472$
± 0.003 ns with a systematic shift of less than 0.01 ns. Errors in the
expected time-of-flight due to uncertainty in the flight path are
expected to be negligible ($\sigma_{TOF}^{Tracking} \simeq 0.05$ ns) and dominated by uncer-
tainty in the polar angle.

The difference between the time-of-flight recorded by the two TDC's
on a given trigger counter provides a useful estimate of the z intercept
of the track along the counter. This estimate (Z_{TOF}) can then be compared
to the more accurate intercept estimate provided by tracking ($Z_{TRACKING}$).
For the data sample under consideration, the distribution of the z
estimate differences is approximately gaussian with a sigma of 5.7 cm
over a nearly flat tail. This tail is presumably due to the presence
of trigger counter accidentals or multiple hits. Throughout this thesis
we shall invalidate flight times satisfying $|Z_{TOF} - Z_{TRACKING}| < 15$ cm,
which should invalidate less than 5% of legitimate flight times and
over 80% of accidental and multiple hit flight times.

Our final measurement of the time-of-flight system concerns the
trigger counter efficiency. We have crudely measured this efficiency to
be ∿93% by examining how often a given counter fires if a track of momentum
exceeding 350 MeV/c is aimed towards the middle 1/3 of the trigger counter.
The value of 350 MeV/c was chosen to insure that the particle would not
stop in the 1.3 cm thick aluminum spark chamber support can between the
spark chambers and the trigger counter array. Because the effects of

accidentals and multiple hits were not eliminated, this represents a less than perfect measurement.

D. Hardware Trigger

The hardware trigger used at the Magnetic Detector involves coincidences between the pipe counters, trigger counters, and shower counters. The trigger used for the data sample under discussion required the below 2 conditions:

1. A coincidence between the inner and outer pipe counters. Each pipe counter is divided into 2 sections by a vertical plane, and valid coincidences require inner and outer counter firings on the same side.

2. Two "tashes" or two trigger and associated shower counter combinations. An associated shower counter lies radially outward from the given trigger counter or is the next closest shower counter. Configurations where there are only 2 tashes which share the same shower counter are invalid.

If the above conditions are met within a 200 ns window after the pulse from the beam pick-up electrode, the spark chambers are pulsed, ADC's and TDC's are started and stopped, and ultimately the event is written on tape. If not, all trigger and shower counter flip-flops are reset to a no-hit condition, and the detector waits for a new electron and positron bunch.

Because of the high efficiency for the pipe and trigger counters, tashing efficiency is essentially determined from the shower counter efficiency. Clearly the probability that an event will trigger the magnetic detector depends primarily on the number of charged tracks within the
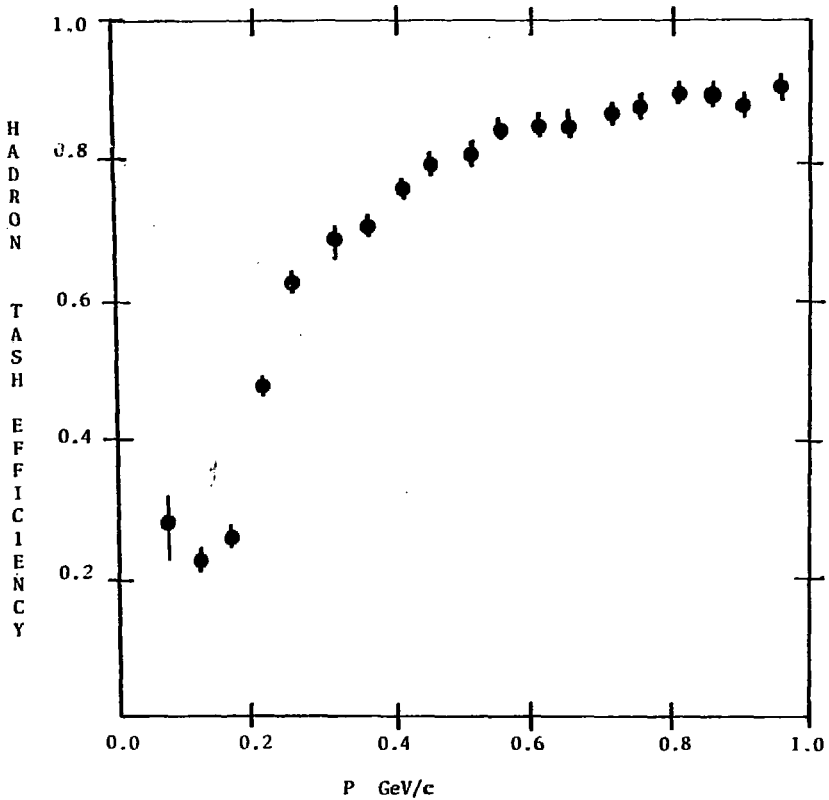
Fig. 8

Hadronic tash efficiency as a function
of prong momentum.   The data in this curve are
dominated by pions.   (Redrawn from th thesis
of Scott Whitaker -- Whitaker 76)

triggering volume and on the momentum of these tracks. For the purposes
of understanding the trigger, it is convenient to introduce a quantity
known as the tashing efficiency. The tashing efficiency is defined as the
number of tracks of a given momentum which fire a trigger counter and its
associated shower counter, divided by the total number of tracks of the
given momentum. It is known (Whitaker 76, Hollebeek 75) that this proba-
bility depends strongly on the prong momentum but weakly on the prong polar
angle θ for prongs satisfying $|\cos\theta| < .60$.

Fig. 8, redrawn from the thesis of Scott Whitaker, shows a measure-
ment of the tash efficiency as a function of the prong momentum. No effort
is made to use time-of-flight information to tag particle type; however
pions are expect to dominate. Bhabha and muon pair events have been
eliminated. As Fig. 8 illustrates, the trigger essentially requires events
to have at least 2 prongs with momenta exceeding 250 MeV/c.

E.   Detector Simulation Program

We have developed a detector simulation program incorporating many
of the previously discussed features of the SPEAR Magnetic Detector. This
program has proven useful in understanding efficiency and resolution
effects for several processes described in this thesis. It is generally
run in conjunction with standard Monte Carlo phase space 4-vector genera-
tion subroutines which serve to generate a user coded process (Friedman 71).

The detector simulation then begins on the space point level.
Tracks are traced through a uniform 4 kG magnetic field to sequential
detector elements. Tracks are scattered at the central radii of the beam

pipe and two pipe counters according to a random multiple coulomb scattering angle drawn from a gaussian distribution. Multiple scattering in the cylinder of wires of the proportional and spark chamber system is simulated in two steps. As a track is traced to successive wire planes, a uniformly distributed random number is drawn to decide whether or not a scattering will occur and through how much wire material the track will traverse. This decision depends on the angle of the track with respect to the wire cylinder normal. A Gaussianly distributed random scattering angle is then drawn and the track is scattered as before. Energy loss effects are incorporated within the subroutine which handles multiple scattering.

Space points are recorded at 6 radii corresponding to the proportional chambers and 4 spark chambers. These points are "wiggled" in z and azimuth according to a Gaussian distribution. Space points are, of course, not recorded for tracks intercepted beyond the physical length of the chambers, thus insuring automatic implementation of the proper geometrical cut. Helix fits are performed for tracks with at least 3 of the possible 4 space points in the spark chambers.

Helix fitting proceeds in 2 steps. A circle fit in xy projection provides an estimate of the track transverse momentum, azimuth, and projected distance of closest approach to the beam origin. The dip angle and z distance of closest approach are determined by a linear fit relating the z chamber intercepts to the accumulated arc length for each space point. These fitting procedures can be done with or without a constraint that the circle pass through the origin in xy projection. We can thus simulate single track as well as beam constraint fits.

Timing information is simulated for tracks intercepting the trigger counter cylinder within the physical length of the counters. A fraction of these events are randomly refused timing information in order to simulate counter inefficiency. Timing information is suppressed in addition for tracks which will range out within the spark chamber support cylinder. The remaining tracks are assigned flight times which are Gaussianly distributed around the correct times. Time-of-flight deduced z information is simulated in an analogous fashion.

Shower counter efficiency is simulated using the measured distribution of Fig. 8 . A record of the trigger and shower counter firings is made for the event as a whole for the purposes of hardware trigger simulation. The trigger algorithm is applied to the simulated shower and trigger firing pattern and only events satisfying the trigger are written out on tape in the same format as real data. This last feature allows one to analyze simulation data with the same programs as real data, although provisions are made for circumventing momentum and flight time correction procedures in the simulation data.

A controversial issue in the simulation of charm processes concerns handling of charged K decays in flight. One (rather arbitrary) solution is to simulate the exponential decay position and drop K tracks falling within a certain cut-off radius from the origin in xy projection. This approach follows from the belief that such K tracks would be badly kinked and hence mis-measured or even dropped by the tracking routines and might have bad timing information as well. The effect of this procedure is to reduce efficiency by a factor of $\exp(-R_c/7.5\, P_\perp)$ where R_c is the cut-off radius, and $P_\perp$ is the kaon transverse momentum in GeV/c.

It is difficult to decide on the proper value for R_c because of the complexities of the fitting and tracking programs. Reasonable guesses run from 0.80 to 1.5 m. We shall generally use $R_c \doteq 1.0$ m but can simulate with the extreme values of R_c to monitor systematic uncertainties in simulations. For the work described in this thesis, the uncertainties presented by R_c are considerably smaller than the uncertainties due to low statistics.

We note that in principle one could diminish the systematic uncertainties present in the above method of handling charged kaon in flight decays by a detector simulation on the magnetostrictive wand level. For such a simulation to have any meaning, tracks due to kaon decays would have to be subjected to the identical tracking and fitting programs used on the raw data--a task unequal to the simple space point simulation program employed here. The tracking algorithm employed in the analysis of the SPEAR data under discussion is known to be efficient for long tracks passing close to the beam axis. How well the algorithm performs for short tracks which are essentially uncorrelated with the beam axis is a matter of speculation. It is my opinion that such a complete treatment of kaon decays is unwarranted for the size of the charmed data sample under consideration.

3. DATA ANALYSIS TECHNIQUES

In this brief chapter, we discuss several analysis techniques used repeatedly throughout this thesis. We begin with a description of track dE/dx corrections, followed by a discussion of the track identification through time-of-flight algorithm.

Minimum ionizing tracks suffer an approximately 3 MeV energy loss while traversing the beam pipe and pipe counters. Unless corrected, these energy loss effects can broaden and shift the positions of invariant mass peaks by non-negligible amounts. We have adopted the following correction algorithm. Three sets of 4-vectors are constructed for each track under the π, K, P particle mass hypothesis. The 4-vectors are the beam constraint track parameters corrected for alignment effects. If the beam constraint fit fails, parameters are taken from the single track fit. The track total momentum is incremented by an amount ΔP_i computed from:

$$\Delta P_i = \begin{cases} \dfrac{3.78 \text{ MeV/c}}{\sin\theta} & \text{for } B_i > .93 \\[2ex] \dfrac{3.:2 \text{ MeV/c}}{\sin\theta \ B_i^{2.65}} & \text{for } B_i < .93 \end{cases}$$

where θ is the track polar angle, and B_i is the track velocity under the given particle hypothesis ($i = \pi$, K, or P). Four-momenta are then constructed from this incremented total momentum and the measured azimuth and polar angle.

As previously noted, time-of-flight particle identification plays a crucial role in charm studies. Although there are numerous ways of using the time-of-flight information, unless otherwise noted we shall employ at
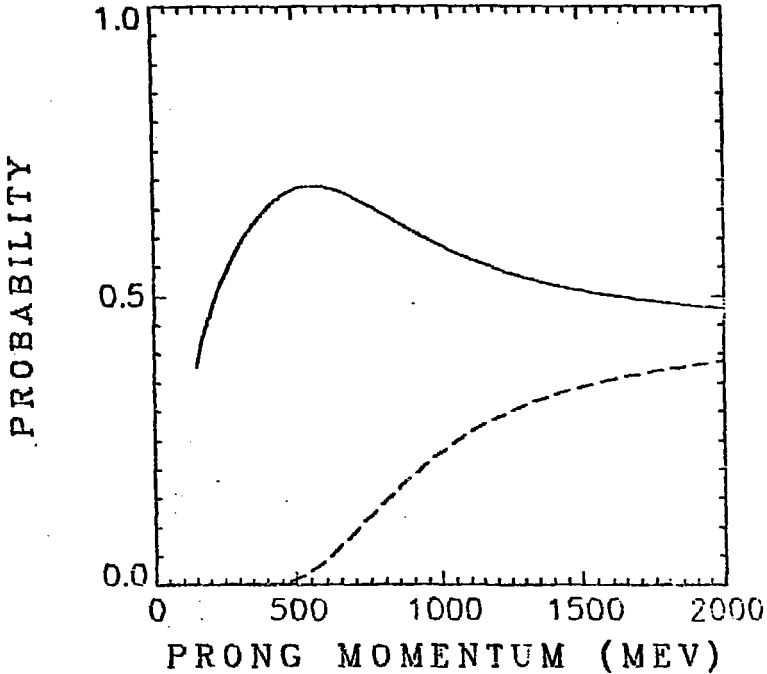
Fig. 1

Results of model calculation of time of flight
tagging algorithm. The solid curve gives the fraction
of true kaons tagged as kaons by the algorithm as a
function of kaon momentum. The dashed curve gives
the fraction of true pions tagged as kaons as a function
of pion momentum.

most mild variations on the following algorithm for tagging tracks with a
definite particle type. For a given track we shall compute separate χ's
between the measured and expected flight times under the kaon and pion
hypothesis. If the track is more consistent with the kaon hypothesis it
is tagged as a kaon; otherwise it is tagged as a pion. Tracks with no
recorded flight times or faulty timing information as judged by z mismatch
are tagged as pions as are tracks with χ's exceeding 3 under both hypo-
theses. This tagging bias towards pions reflects the general observation
that pion production dominates hadron production at SPEAR, especially for
prongs of low momentum.

Such a tagging procedure is of course imperfect and will be of little
use for high momentum prongs. To gauge the efficiency and effectiveness
of the tagging algorithm we have developed a simple analytic model
described in APPENDIX 1 and summarized by Fig. 1. The solid curve of
Fig. 1 shows the fraction of true kaons tagged as kaons as a function of
kaon momentum. The dip below 500 MeV/c reflects the effects of K inflight
decays. We reiterate that prongs not tagged as kaons will be tagged as
pions. The dashed curve of Fig. 1 gives the fraction of pions which
will be tagged as kaons as a function of pion momentum. Thus the upper,
solid curve is basically a measurement of the kaon cut efficiency, whereas
the lower, dashed curve measures pion contamination. These curves show that
the tagging algorithm is reasonably good for prongs of momentum less
than 1 GeV/c.

4. PRESENTATION AND DISCUSSION OF CHARM SIGNALS

Figs. 1 and 2 show the $K^{\mp}\pi^{\pm}$, $K^{\mp}\pi^{\pm}\pi^{\pm}$, and $K^{\mp}\pi^{\pm}\pi^{-}\pi^{-}$ invariant mass distributions for data taken at E_{cm} = 4.028 and 4.415 GeV respectively. These energies were chosen, after the initial charmed meson discovery, to lie at the most prominent peaks of the R = $\sigma_{had}/\sigma_{\mu\mu}$ distribution (Siegrist 76). Approximately equal integrated luminosity was collected at these 2 energies and in a highly non-uniform scan from E_{cm} = 3.9 - 4.6 GeV. This latter sample constituted the data where charmed mesons were initially found by Gerson Goldhaber and Francois Pierre in May of 1976 (Goldhaber 76).

The signals of Fig. 1 are considerably cleaner than those of Fig. 2 Hence we display the 4.028 data in 10 MeV/c^2 bins and the 4.415 data in 20 MeV/c^2 bins. The data of Figs. 1 and 2 were fitted to a Gaussian peak over a linear background. The fit parameters are summarized in the Table.

We estimate possible 10 MeV systematic shifts in these direct mass values. A better set of mass values will be obtained through an analysis of the recoil spectrum presented in Chapter 8.

Measured widths at E_{cm} = 4.028 GeV are consistent with apparatus resolution as determined by Monte Carlo simulation based on the model developed in Chapter 8. Simulation resolutions at 4.028 GeV are 20 MeV/c^2 for the Kπ signal and 9 MeV/c^2 for the K3π signal.

It is relatively easy to account for the detector mass resolution for the Kπ(1865) at E_{cm} = 4.028 GeV. Mass resolution is dominated by momentum measurement error with a smaller contribution coming from Kπ interchange by the time-of-flight algorithm. The recoil study presented

Fig. 1

Charm signals at Ecn = 4.028 GeV .

$E_{cn} = 4.4 \ GeV/c^2$

EVENTS PER 20 MEV/c²

$M_{K^{\pm}\pi^{\mp}\pi^{+}\pi^{-}}$

$M_{K^{\mp}\pi^{+}\pi^{+}\pi^{-}}$

$M_{K^{+}\pi^{-}}$ MeV/c²

Fig. 2
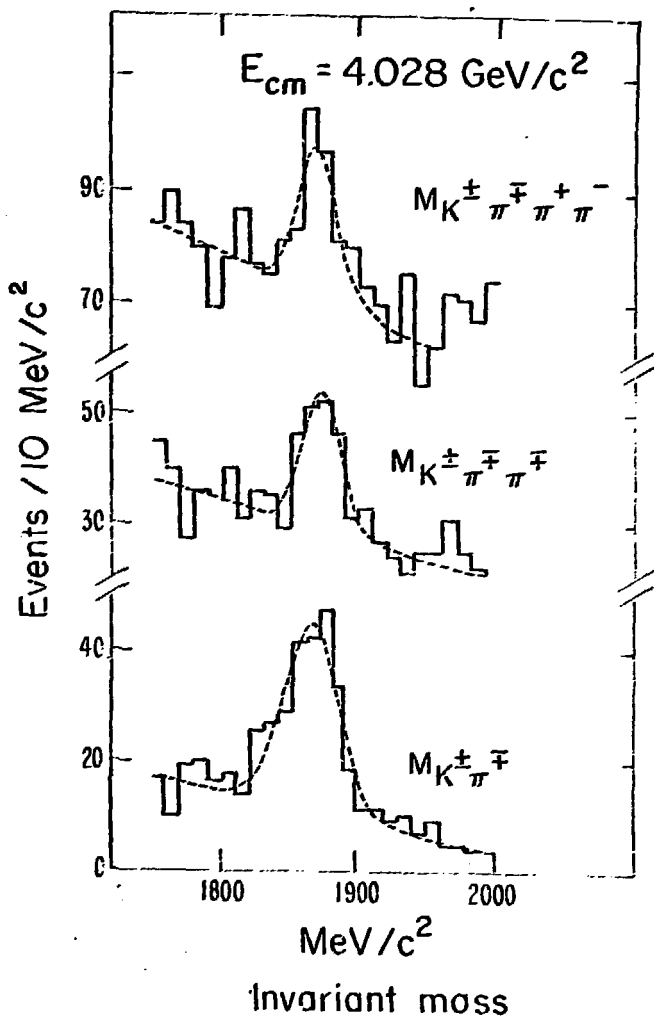
Charm signals at Ecm = 4.415 GeV.

Table 1.

		SIGNAL	MASS	WIDTH
Ecm = 4028	Kπ	171 ± 20	1865 ± 2	20 ± 2
	Kππ	84 ± 19	1872 ± 3	13 ± 3
	K3π	92 ± 30	1869 ± 5	14 ± 5
Ecm = 4415	Kπ	125 ± 34	1876 ± 7	25 ± 7
	Kππ	70 ± 25	1882 ± 9	19 ± 9
	K3π	105 ± 30	1870 ± 5	10 ± 6

All mass units are in MeV/c^2.

All errors are statistical only.

in Chapter 8 shows that the vast majority of $K\pi(1865)$ combinations have velocities of less than 0.3 c. Hence the 2 prongs comprising the $K\pi(1865)$ will be nearly back-to-back with almost equal momenta of ~ 860 MeV/c. Multiple scattering effects are negligible in such a topology; hence the mass resolution in the absence of ambiguity broadening would be:

$$\sigma_M = \frac{2\sqrt{2}}{M} P\sigma_p$$

which for $M_K = 1865$ MeV/c^2, $P = 860$ MeV/c gives $\sigma_M = 15$ MeV/c^2.

The calculation summarized in Chapter 3, Fig. 1 shows that $\sim 7\%$ of neutral 2-prong combinations classified as $K\pi$ will have prongs interchanged and hence suffer an additional ambiguity broadening. Calculations show that interchange effects do not appreciably shift the centers of mass distributions, but rather broaden mass distributions by an amount proportional to the $K\pi$ momentum for momenta of less than 2 GeV/c. By explicit numerical integration we find the RMS invariant mass broadening due to interchange to be $\sigma_M^{AMB} = .07 \sqrt{\langle P_{\pi K}^2 \rangle}$ where $\langle P_{\pi K}^2 \rangle$ is the second moment of the $K\pi$ lab momentum spectrum. In obtaining this expression we assume an isotropic decay of the $K\pi$ (1865) system and integrate over the kaon helicity angle. With knowledge of the momentum spectrum discussed in Chapter 8 we compute $\sigma_M^{AMB} = 47$ MeV/c^2. Including this additional source of broadening for 7% of the events with the 15 MeV/c^2 broadening due to momentum mismeasurement, we obtain a total mass resolution of $\sigma_M \simeq 19.5$ MeV/c^2 which is in excellent agreement with the Monte Carlo estimate.

It is of interest to use this value for the expected resolution of the $K\pi$ (1865) signal to extract an upper limit on its natural full width at maximum (Γ). For the purposes of this measurement, we use $K\pi$ (1865)

signals from the entire charmed data sample $3.9 < E_{cm} < 4.6$ GeV subject to a sharp cut in Kπ missing mass (described and justified in Chapter 9) to improve signal purity.

The Kπ invariant mass distribution is fitted to a signal term over a linear background. The signal term is a Gaussian resolution function numerically convoluted with a Breit-Wigner of various trial widths. Specifically we fit to the form:

$$\frac{dN}{dM} = A \ S(M) + BM + C$$

where

$$S(M) = \frac{1}{\pi(\Gamma/2)} \ \frac{1}{\sigma\sqrt{2\pi}} \ \int_{M-3\sigma}^{M+3\sigma} d\mu \ \frac{e^{-\frac{1}{2}\left(\frac{M-\mu}{\sigma}\right)^2}}{1 + \left(\frac{2}{\Gamma}(M-M^0-\mu)\right)}$$

For a given trial Γ we perform a binned maximum liklihood fit varying A, B, and C. M^0 is fixed at 1865 MeV/c^2, and $\sigma = 20$ MeV/c^2. Denoting the maximum liklihood for a given Γ as $P(\Gamma)$ we extract a confidence level distribution CL (Γ) via:

$$CL \ (\Gamma) = \frac{\int_0^\Gamma P(\Gamma') \ d\Gamma'}{\int_0^{60MeV} P(\Gamma')d\Gamma'} \ .$$

This distribution is shown in Fig. 3a. The 90% CL upper limit is $\Gamma < 22.5$ MeV/c^2 (90% CL). In Fig. 3b we show the Kπ invariant mass distribution with curves appropriate to the best fit value of
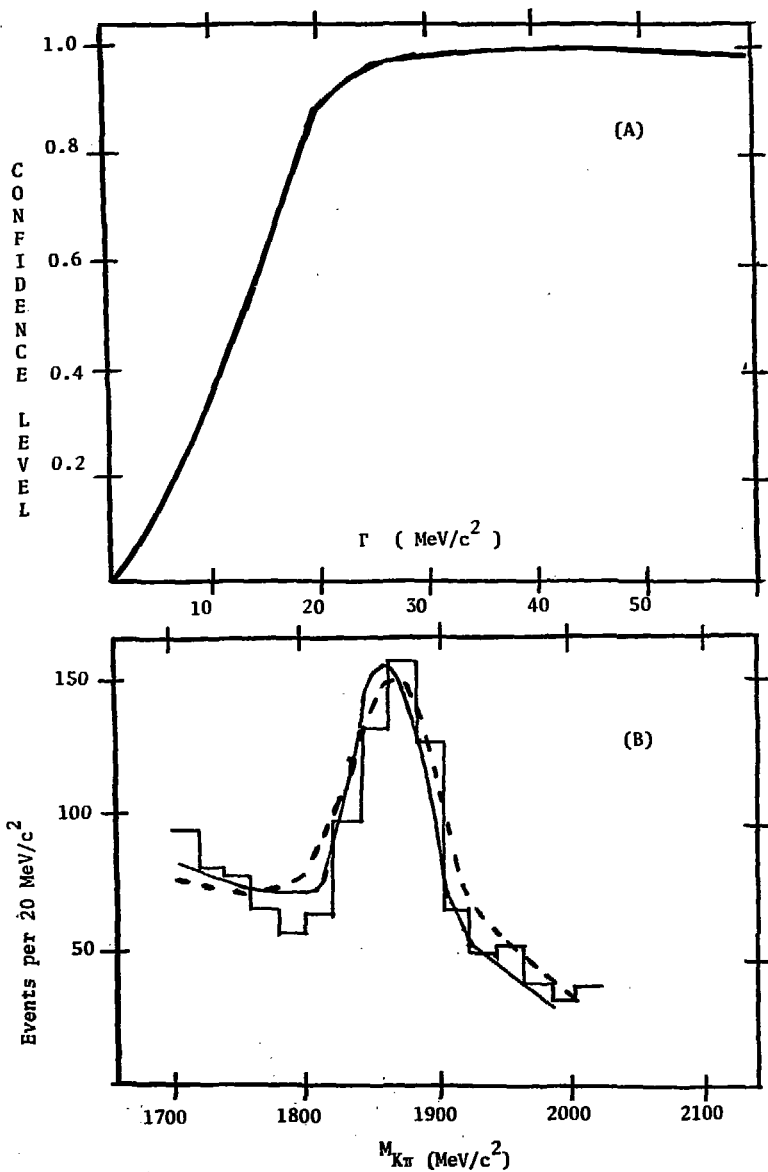
Fig. 3

(A) Confidence level plot for Kπ (1865) natural
     resonant width (Γ).   90% C.L. upper limit is 22.5 MeV/c^2.

(B) Kπ (1865) signal with best fit curve (Γ = 10 MeV,
     solid curve) , and 90% C.L. curve (Γ = 22.5 MeV/c^2 ,
     dashed curve).

$\Gamma(\Gamma = 10 \text{ MeV}/c^2)$ and the 90% CL value ($\Gamma = 22.5 \text{ MeV}/c^2$). The value $\Gamma = 10 \text{ MeV}/c^2$ should not be taken seriously. The data are consistent with $\Gamma = 0$ and a more stringent upper limit will be extracted from a study of the recoil spectrum.

A similar analysis has been applied to the $K\pi\pi$ and $K\pi\pi\pi$ signals. In both cases, one is hampered by larger backgrounds and poorer statistics. Hence, although the mass resolution is better for these signals, the 90% CL upper limits on Γ are comparable. We find $\Gamma < 30 \text{ MeV}/c^2$, and $\Gamma < 35 \text{ MeV}/c^2$ for $K\pi\pi$ and $K\pi\pi\pi$ respectively.

From the preceding discussion it is apparent that new, statistically strong, narrow signals have been observed in two charged states with masses in the vicinity of 2 GeV/c^2. A demonstration that the signals involve kaons, however, is an obviously important component to any argument identifying the new mesons with the charmed (D^0, D^+) isodoublet.

Kaon momenta in the $K\pi\pi\pi$ and $K\pi\pi$ signals nearly always lie below 600 MeV/c where Chapter 3 Fig. 1 shows the time-of-flight tagging algorithm offers good rejection against pions. For the $K\pi$ signal with kaon momenta near 860 MeV/c, contamination is no longer negligible and one can legitimately question whether or not the signal is truly in $K\pi$ or is rather a reflection of a signal in $\pi\pi$ or KK.

Low momentum $D^0 \rightarrow K\pi$ signals would be expected to produce narrow reflection peaks at 1985 MeV/c^2 in K$\bar{\text{K}}$, and at 1745 MeV/c^2 in $\pi\bar{\pi}$. The positions of the three peaks are of course independent of which of the three channels represents the true decay mode of the new resonance. We use the complete charmed data sample from 3.9 - 4.6 GeV = E_{cm}, with no additional kinematic cuts. As Figure 4 shows, all three expected peaks
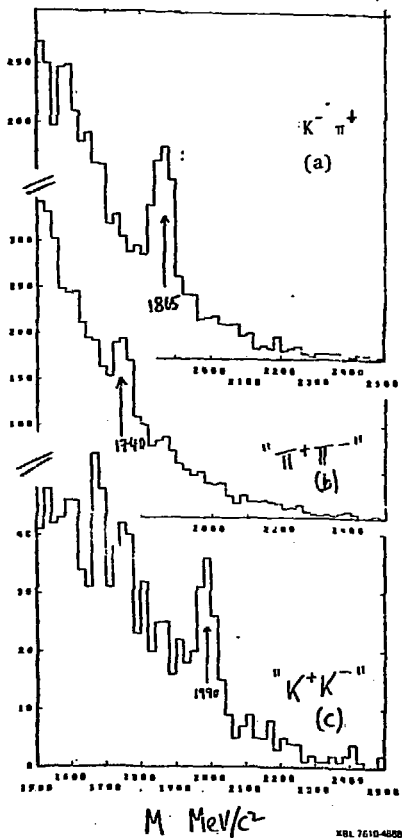
Fig. 4

Positions of time of flight
reflection peaks . The true signal
is in K π . The KK and ππ signals
are misidentified reflections of the
true signal.

Table 2.

		PEAK POPULATIONS			χ^2/dF	C.L.
		$K\pi$	π.	KK		
	DATA	319 ± 33	172 ± 35	65 ± 11		
MODELS	$K\pi(1865)$	337 (.29)	143 (.69)	75 (.83)	1.8/2	41%
	$\pi\pi(1740)$	200 (13.0)	322 (18.4)	39 (5.6)	37/2	$<10^{-5}$
	KK(1990)	211 (10.7)	22 (18.3)	322 (546.0)	575/2	$<10^{-5}$

χ^2 contribution is in ()
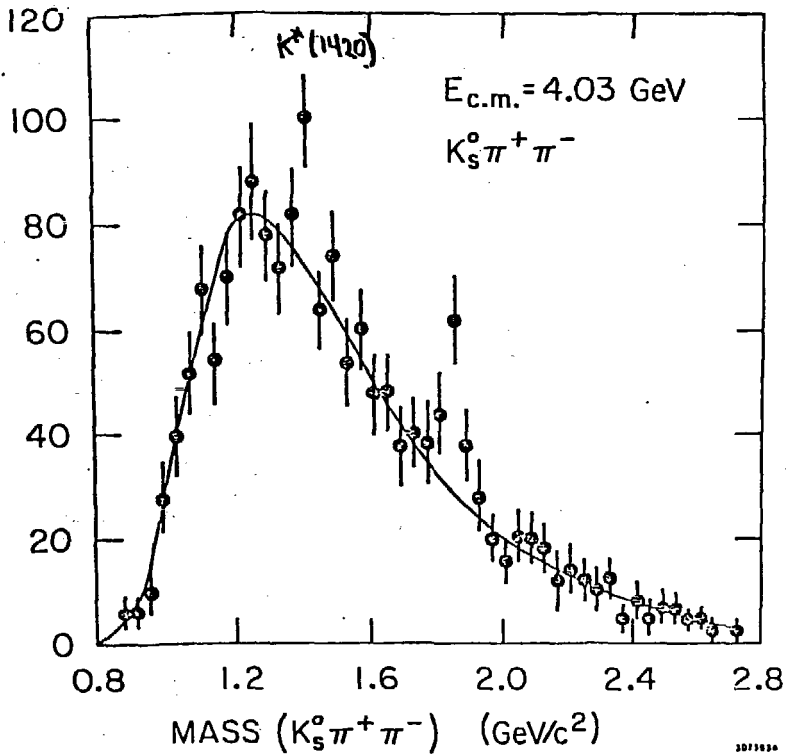
Fig. 5

Evidence for a $K_s^o \pi^+ \pi^-$ decay mode of the D^0.   Y - ordinate
is in units of Events per 40 MeV/c^2 .   Data was collected
at E_{cm} = 4.028 GeV.

are found in the data. Fits to Figure 4, consisting of a Gaussian signal over a smooth background, reveal 319 ± 33 signal combinations classified as $K\pi$, 65 ± 11 signal combinations classified as $K\bar{K}$, and 172 ± 35 signal combinations classified as $\pi\bar{\pi}$. In Table 2 we compare this signal breakdown to the signal breakdown for three simulation models. The three models assume that the true signal is $K\pi(1875)$, $\pi\bar{\pi}(1745)$, or $K\bar{K}(1985)$. The only model with a confidence level exceeding 10^{-5} is $K\pi(1865)$ with a confidence level of 41%. We conclude, therefore, that one is indeed seeing a new particle whose known decay modes involve kaons. As a final demonstration of this fact, in Figure 5 we present the $K_s\pi^+\pi^-$ invariant mass plot obtained by Vera Lüth for the 4.028 GeV Magnetic Detector data. Clear evidence is seen for a $K_s\pi^+\pi^-(1865)$. K_s selection, described in Lüth 77 is both kinematic and geometrical and is estimated to have less than 10% contamination.

We see from the foregoing that reasonably strong evidence for charm exists from the mere observation of the signals in $K\pi$, $K2\pi$, and $K3\pi$ masses in the Spear data near E_{cm} = 4 GeV. The signals were found at the expected energies, with the expected widths and decay modes. Evidence was present at the very onset of charm work that the new mesons were produced associatively in e^+e^- annihilation. This evidence is reviewed in Chapter 6. A final piece of evidence, presented in Chapter 5, considerably strengthens the case that the neutral and charged signals observed near 2 GeV can be identified with the (D^0,D^+) charmed isodoublet.

5. EVIDENCE FOR PARITY VIOLATIONS IN THE DECAYS OF THE D'S

Throughout this Chapter we shall denote the $K\pi(1865)$ as the D^0 and the $K\pi\pi(1875)$ as the D^+. We will begin by analyzing the $D^+ \to K\pi\pi$ Dalitz plot in an effort to investigate the spin and parity of the $K^{\mp}\pi^{\pm}\pi^{\pm}$ final state.

As discussed in Zemach 64, the Dalitz plot for a 3 pseudoscalar final state of a given pure spin-parity exhibits a characteristic pattern of depopulation. For example, the Dalitz plot for a natural spin-parity final state of 3 pseudoscalars must exhibit depopulation along the boundary, owing to the necessity of forming the decay amplitude from an axial vector. Additional areas of depopulation are often found for specific spin-parity assignments due to the operation of additional symmetry requirements. The heavy lines of Figure 1 show the position of zeros in the Dalitz plot expected for various low lying spin-parity assignments of the final state $K^{\mp}\pi^{\pm}\pi^{\pm}$. In order to obtain a relatively clean sample of $K\pi\pi(1876)$ events we make use of the result that for the E_{cm} region, $3.9 < E_{cm} < 4.25$ GeV; the recoil mass(M_{rec}) spectrum shows a sharp spike near 2 GeV. We thus used a data sample with the E_{cm} region chosen as above coupled with a cut $1.96 < M_{rec} < 2.04$ GeV/c^2. Figures 2a and 2b show the resulting exotic and nonexotic $K\pi\pi$ invariant mass distributions. A fit to the spectrum of Fig. 2b was appropriately scaled to serve as a background for Fig. 2a. Figure 2a shows a fit to a Gaussian peak over this background. Figure 3a shows the (folded) Dalitz plot for $K^{\mp}\pi^{\pm}\pi^{\pm}$ events with the additional invariant mass (M) requirement
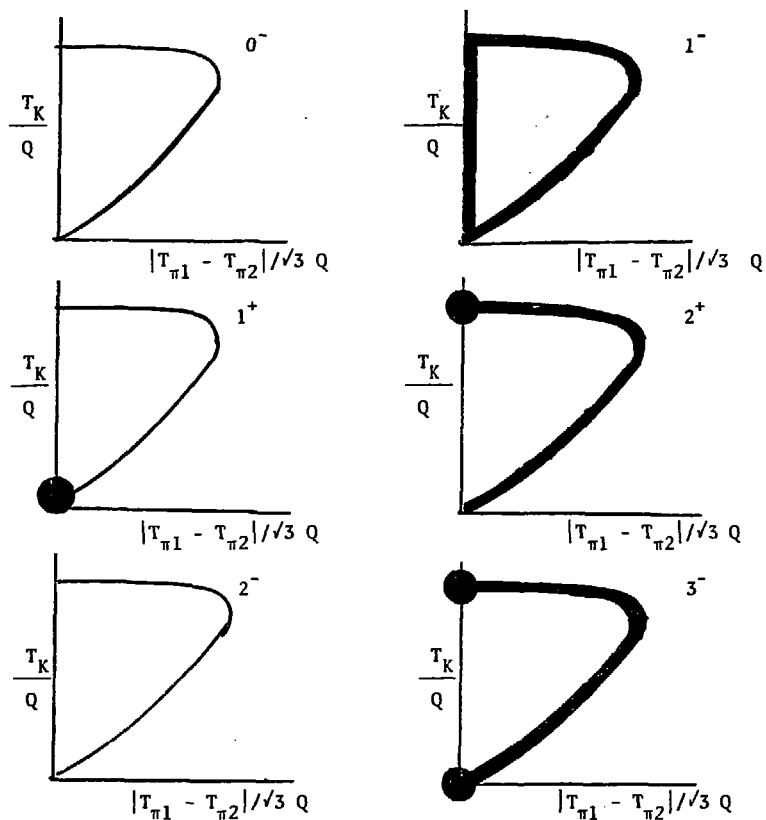
Fig. 1

Location of Dalitz zero's for several spin-parity
assignments of the final state $K^- \pi^+ \pi^+$. Heavy lines
and circles give the positions of the expected zero's.
If a circle overlaps a heavy line , the zero is of a
higher order and the region of depopulation extends farther.
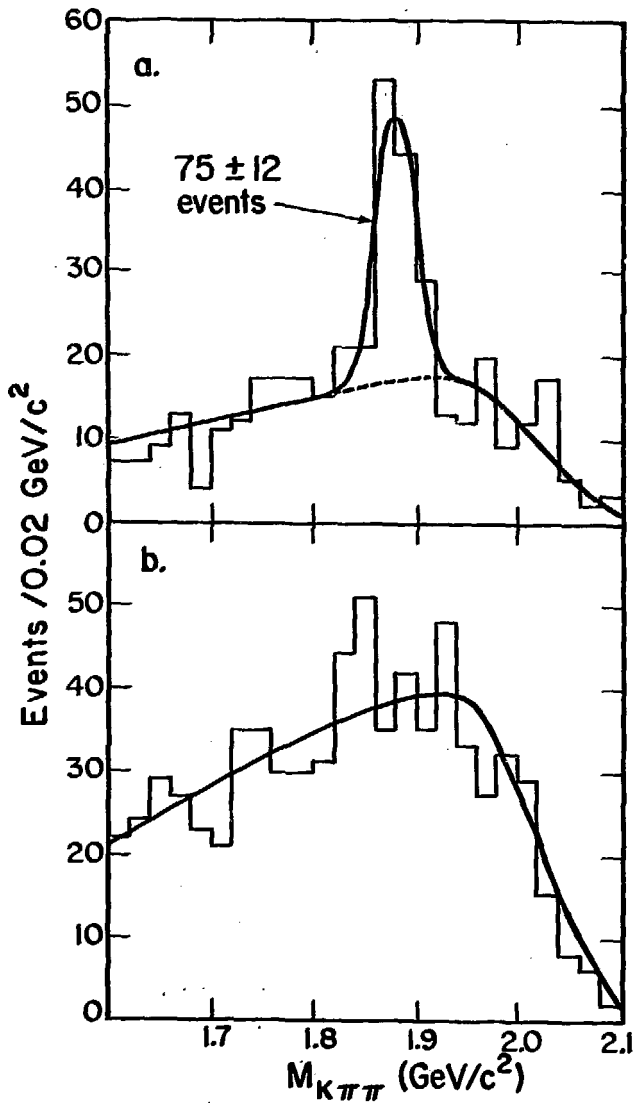
Fig. 2

Kππ invariant mass distributions for
exotic charge combinations (Fig. a.)
and non-exotic charge combinations (Fig. b.).
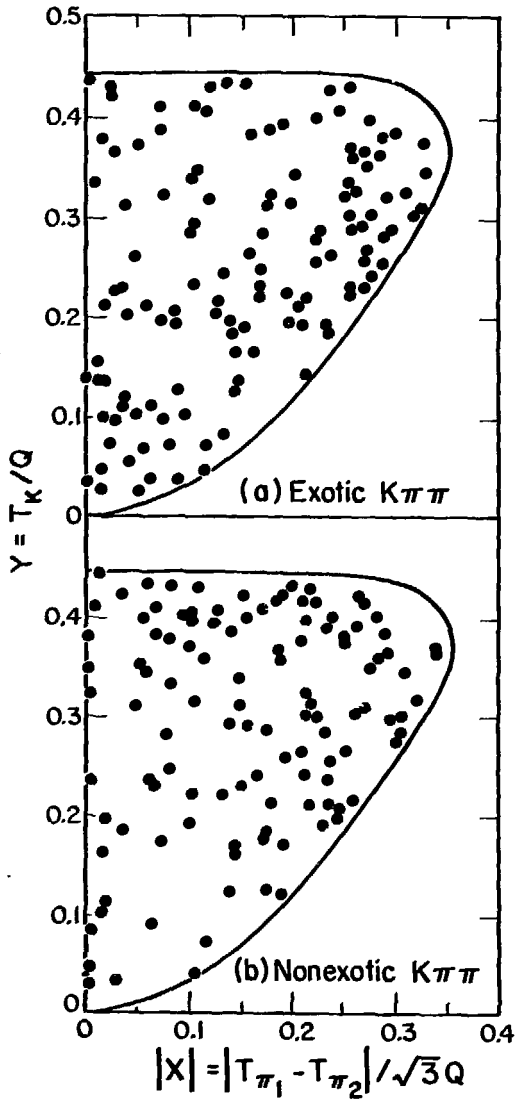
Fig. 3

Dalitz plot for exotic (Fig. a) and non-exotic (Fig. b) charge combinations of $K\pi\pi$. Here T refers to the kinetic energy of a given particle in the D^+ rest frame, and $Q = M_D - M_K - 2 M_\pi$.

The axes are labeled:

$Y = T_K/Q$ (vertical axis)

$|X| = |T_{\pi_1} - T_{\pi_2}|/\sqrt{3}Q$ (horizontal axis)

(a) Exotic $K\pi\pi$

(b) Nonexotic $K\pi\pi$

1.86 < M < 1.92 GeV/c^2. We find a sample of 126 events in the Dalitz
plot of Figure 3a of which we estimate 58 are background. In Figure 3b
we show a background Dalitz plot consisting of 112 nonexotic combinations
$K^{\mp} \pi^+ \pi^-$ satisfying the same mass and missing mass cuts as the exotic
combinations of Figure 3a. Neither plot shows obvious boundary depopu-
lation which argues for a pattern of non-natural parity. Such a super-
ficial analysis has serious drawbacks, although we shall see that it gives
the correct answer.

It is highly desirable to make a statement on the statistical strength
of this observation. This cannot be easily done without knowledge of the
expected extent of the boundary depopulation, i.e. how close must one get
to see a substantial reduction in Dalitz density.

Unfortunately one cannot answer this question from symmetry considera-
tions alone. However, reasonable estimates can be made for specific spin
assignments by using the simplest amplitudes which vanish at the places
required from symmetry considerations. By simplest amplitudes, we mean
the amplitudes involving the least power of particle momentum or kinetic
energy consistent with the requirements of symmetry. The discrepancy be-
tween these expressions and the densities computable in a complete theory
would be expressed as multiplicative form factors. Experience has shown
(Stevenson 62) such functions are generally slowly varying functions of
the Dalitz variables for decays with limited available phase space. In
such cases momenta (K) are small or comparable to the reciprocal range of
interactions (R) and one is effectively approximating the decay amplitude
by a low order expansion in KR. We shall compare our Dalitz distributions
to possible "simplest" matrix elements, although admittedly we are pushing
their range of applicability. We limit our analysis to low lying spin states

and explicitly consider 1^- and 2^+. A final state of three pseudo-scalar particles cannot have pure 0^+ spin-parity.

For $J^P = 1^-$ the matrix element is constructed from an axial vector symmetric under the exchange of the two pions. The essential form of such a quantity is $(T_{\pi_1} - T_{\pi_2}) \vec{\pi}_1 \times \vec{\pi}_2$, where $\vec{\pi}$ represents a pion momentum in the rest frame of the $K\pi\pi(1876)$, and T_π represents its kinetic energy. For the case of unpolarized production one then expects an intensity I_1- given by

$$I_1\text{-} \propto |T_{\pi_1} - T_{\pi_2}|^2 |\vec{\pi}_1 \times \vec{\pi}_2|^2.$$

For 2^+ we construct a symmetric, traceless, second-rank tensor which is also symmetric under the exchange of the two pions. We use $A^{ij} = \Delta\pi^i q^j + \Delta\pi^j q^i$ where $\Delta\pi$ is the difference of the pion momenta and q is their cross product. For unpolarized production one expects an intensity given by:

$$I_{2^+} \propto \sum_i \sum_j A^{ij} A_{ji} = |\vec{\pi}_1 - \vec{\pi}_2|^2 |\vec{\pi}_1 \times \vec{\pi}_2|^2.$$

We note that the pion exchange symmetry implied by Bose statistics creates a zero along the y-axis for $J^P = 1^-$ and a higher order boundary zero at the top edge of the $J^P = 2^+$ Dalitz plot in addition to the boundary zero due to parity and angular momentum considerations.

Owing to our limited statistics we display signal for events falling in either of two Dalitz discrimination regions separately chosen for our two hypothesis 1^- and 2^+. The discrimination region boundaries were chosen as contours of constant 1^- or 2^+ matrix elements. The particular contour chosen was such that the product of detection efficiency
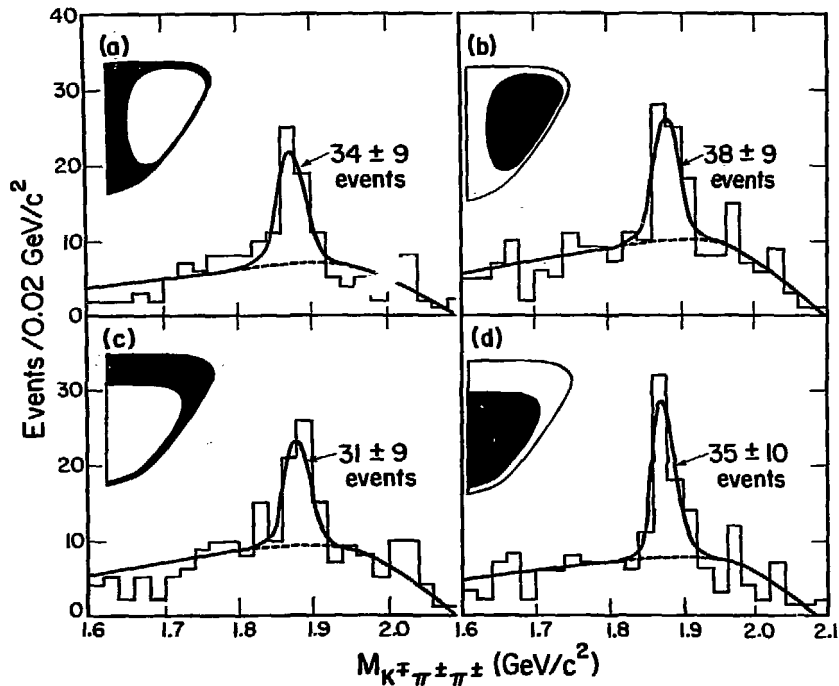
XBL 7610 4114

Fig. 4

The four $K\pi\pi$ invariant mass distributions
for events falling in the shaded Dalitz
plot discrimination regions indicated by
the respective inserts. Region a and b
are used to test $J^P = 1^-$. Region c and d
are used to test $J^P = 2^+$.

times phase space would lead to an expectation of equal numbers of events on either side of the contour, if the matrix element were constant. Events generated using the 1^- or 2^+ matrix elements, of course, will <u>not</u> evenly populate their respective discrimination regions. They will preferentially populate the region where matrix element is large.

The four discrimination regions have nearly equal area in the Dalitz plot owing to the approximately uniform $K\pi\pi$ detection efficiency as judged by Monte Carlo simulation. The only substantial efficiency drop occurs near the upper right hand corner of the Dalitz boundary (large x and large y). This Dalitz region corresponds to a configuration where the pions share a small amount of the available kinetic energy, and the sharing is quite unequal, meaning that one pion is nearly at rest in the D^+ rest frame. Such pions have a laboratory momentum of only 40 MeV/c and are near the magnetic field cut-off momentum for track identification. We perform the simulations with D^+ momentum of 535 MeV/c, which is the momentum expected for the reaction $e^+ e^- \to D^+ D^{*-}$ (2008). Our analysis of the recoil spectrum presented in Chapter 6 will demonstrate the presence of this state of higher charm excitation and show that the assumed reaction does indeed dominate D^+ production near threshold.

In Figure 4 we show the $K2\pi$ invariant mass distributions for events with Dalitz variables in the four discrimination regions. We estimate the signal by a fit of a Gaussian signal over the scaled non-exotic bac: ground. The table below summarizes the results:

	1⁻ REGIONS		2⁺ REGIONS	
	Peripheral	Central	Peripheral	Central
DATA	34 ± 8	38 ± 9	31 ± 9	35 ± 10
PHASE SPACE MONTE CARLO	36	36	33	33
1⁻ MONTE CARLO	7.8	64.2	---	---
2⁺ MONTE CARLO	---	---	10.0	56.0

We see consistency with the phase space Monte Carlo for either discrimination region. The 1^- assignment and 2^+ assignments are ruled out on the 4 and 3 standard deviation level respectively. We argue that, since higher spin-parity assignments will possess boundary zeros, the ample signal in the 2^+ peripheral region argues against these assignments as well.

We conclude that the final state into which D^+ decays is not consistent with being a natural spin-parity eigenstate, unless the spin is improbably high (i.e. 3 or greater). On the other hand the two body decay $D^0 \rightarrow K\pi$ implies that the D^0 has natural spin-parity. We may then infer that either:

1) D^0 and D^+ have different spin-parity assignments. Despite their closeness in mass, they are not members of the same isomultiplet.

or 2) The D^0 (and/or D^+) is actually two particles of opposite parity with nearly degenerate mass (parity doublets).

or 3) The decay of the D^0 or D^+ does not conserve parity, and hence the decay is via the weak interaction.

Although alternatives (1) and (2) are technically valid possible explanations for this effect, they both require an exceptional, and rather unnatural, coincidence in the masses of newly discovered, narrow states. Alternative (3), on the other hand, is quite natural and expected if the new states are indeed the D^0, D^+ isodoublet of charm and must decay into ordinary hadrons weakly.

We note from the preceding that the data appears consistent with a phase space Dalitz distribution. This distribution would be expected for a pseudo-scalar final state. In light of the demonstrated parity violation, however, the Dalitz plot is no longer a useful tool for investigating possible spins for the charmed meson candidates because of possible interference effects between the natural and unnatural parity amplitudes for a given spin. In Chapter 9 we will investigate possible spin assignments for the new mesons using an algorithm not dependent on parity conservation.

This exhausts our evidence for the contention that the $K\pi$ (1865) and $K\pi\pi$ (1875) are the expected D^0, D^+ charmed isodoublet. There appears to be evidence for a 2 sigma enhancement in $\pi^+\pi^-$ (1865) but this is not as yet statistically compelling. When more data are taken and the $K\pi/\pi\pi$ ratio is shown to be consistent with $\cot\theta^2_{Cabibbo}$ this issue should be resolved to anyone's satisfaction. We assume our signals are charmed from here on and explore several properties not crucial to the charmed identification.

6. A QUALITATIVE LOOK AT THE RECOIL SPECTRUM

AGAINST CHARMED MESONS

In Figure 1 a,b,and c we show the recoil spectrum against the $K^+\pi^-$ (1865), the $K^+\pi^-\pi^+\pi^-$ (1865) and the $K^+\pi^-\pi^-$ (1875) for the data collected from $3.9 < Ecm < 4.6$ GeV. In Figure 1 we require the $K\pi$ and $K3\pi$ invariant mass to lie from 1820 and 1900 MeV/c^2, and require the $K2\pi$ invariant mass to lie from 1850 to 1910 MeV/c^2. All three spectra are subtracted spectra , computed with a fixed D^0 mass of 1865 MeV/c^2. For the neutral meson, the backgrounds are taken from adjacent regions of the $K\pi$ and $K3\pi$ invariant mass plots, while for the D$^+$ signal, we use a background taken from the non-exotic $K^+\pi^+\pi^-$ system subject to identical cuts in invariant mass.

As we have noted in Chapter 4 , approximately 60% of the legitamate $D^0 \rightarrow K^-\pi^+$ candidates will be classified as $\pi\,\bar{\pi}$ or $K\,\bar{K}$ by the time of flight tagging system owing to our finite time of flight resolution. Experimentally , such misidentified D^0 candidates can be easily found because they create narrow reflection peaks in the $K\,\bar{K}$ and $\pi\,\bar{\pi}$ invariant mass plots. Except for negligible differences in the energy loss corrections for pions versus kaons, the D^0 momentum will be correctly measured for these reflection D^0 candidates. Thus they can be easily entered in a recoil mass distribution if the recoil mass is computed with a fixed D^0 mass.

All three recoil spectra show evidence for sharp recoil peaks indicating that charm production occurs primarily through two body processes for the energies under discussion. These peaks appear at
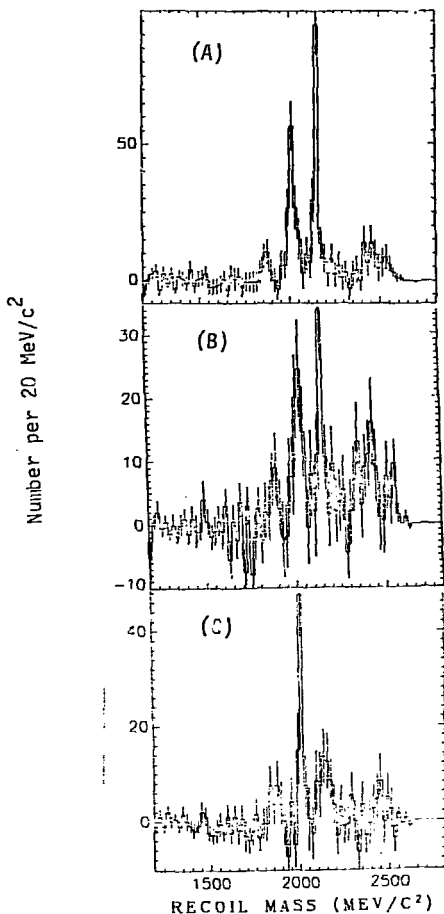
Fig. 1

Subtracted recoil mass spectra against D^0's and D^+'s for the data from 3.9 E_{cm} 4.6 GeV.

    A) Recoil mass against the $K\pi$ (1865)
    B) Recoil mass against the $K3\pi$ (1865)
    C) Recoil mass against the $K2\pi$ (1875)

Spectra are computed using the indicated nominal fixed masses.
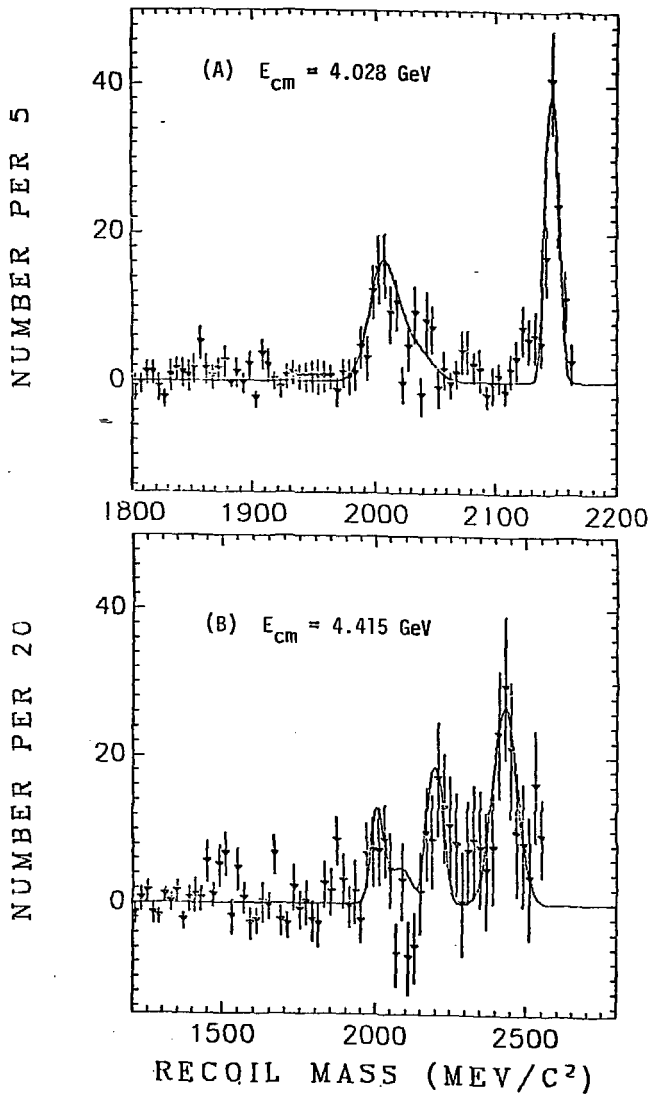
Fig. 2

D^0 subtracted recoil spectra at two fixed energies. Solid curves are explained in text.

nearly the same recoil mass for all three signals, but the area
ratios are quite different for the charged versus the neutral recoil
system.   The peaks shown in Figure 1 appear to represent charm
meson production via the neutral and charged versions of :

$$e^+ e^- \rightarrow D \overline{D} \qquad \text{Reaction (1)}$$
$$\rightarrow D \overline{D}^* + \overline{D} D^* \qquad \text{Reaction (2)}$$
$$\rightarrow D^* \overline{D}^* \qquad \text{Reaction (3)}$$

For D masses near 1870 MeV/c^2 and D* masses near 2010 MeV/c^2 one would
expect the peaks due to Reaction 1 through 3 to lie at 1865 MeV/c^2, 2010
MeV/c^2, and 2150 MeV/c^2 respectively. The sharpness of the peak ascribed
to D* $\overline{D}^*$ production indicates that D*'s can cascade to D's via pion
emission as expected for a pair of mesons which carry a common conserved
quantum number. A quantitative analysis of the recoil spectrum , which
we shall discuss later, shows evidence for D$^{*0} \rightarrow$ D$^0 \gamma$ as well, occuring
at a rate comparable to D$^{*0} \rightarrow$ D$^0 \pi^0$.

In Figure 2a we present the "Kπ" recoil spectrum for data collected
at Ecm = 4.028 GeV. The solid curve of Figure   2a gives the expected
shape of the D^0 recoil system for Reactions 2 and 3   , where D$^{*0} \rightarrow$ D$^0 \pi^0$.
We have computed this curve using a nominal D^0 ,D^{*0} mass of 1865 and 2005
MeV/c^2 and have adjusted peak areas to crudely match the data.

The interpretation of the second peak near 2150 MeV/c^2 as a
kinematic reflection of Reaction 3 may appear surprising in light of
its narrow width. An alternative interpretation is that this peak is
due to the production of a higher mass charm state at 2150 MeV/c^2. This
interpretation is contradicted , however, by the data of Figure 2b , which
shows the D^0 recoil spectrum at Ecm = 4.415 GeV. The solid curve

again gives the positions of peaks due to Reactions 2 and 3. We note that the peak that was at 2150 MeV/c^2 in Figure 2a has shifted to 2200 MeV/c^2. This is what would be expected for a reflection of Reaction 3 , whereas a new resonance at 2150 MeV/c^2 would not be expected to change position when the center-of- mass energy changes.

We note the presence of an enhancement at 2440 MeV/c^2 in the recoil spectrum obtained at Ecm = 4.415 GeV. The solid curve of Figure 2b represents this enchancement by a Gaussian peak centered at 2440 MeV/c^2 with a width of σ = 50 MeV/c^2. Such an enhancement may be due to multibody charm production such as $e^+ e^- \to D^* \bar{D}^* \pi$, or the formation of a new, higher mass charmed state. Higher mass states are expected in the charm theory, but since this enhancement can be tolerably fit by a multiparticle phase space Monte Carlo , we cannot prove that such new states exist.

7. OBSERVATION OF $D^{*+} \rightarrow D^o \pi^+$ AND LIMITS ON $D^o - \overline{D}^o$ MIXING[†]

Up to this point our evidence for the existence of the D^* comes through the observation of structure in the D^o and D^+ recoil spectra . In this section we will present direct evidence for the existence of the D^{*+} by constructing its invariant mass from the $K^- \pi^+ \pi^+$ final state obtained via the sequence $D^{*+} \rightarrow \pi^+ D^o$; $D^o \rightarrow K^- \pi^+$. Because of the low Q value for the reaction $^{*+} \rightarrow \pi^+ \, ^{\sim o}$, the cascade pion moves in the detector frame with ntially the same velocity as the D^{*+}, and hence has only 7% of the D^{*+} momentum . Because of the 4 KG magnetic field of the SPEAR Magnetic Detector, particles having momentum less than about 70 MeV/c will escape detection. Hence in order to observe the π^+ from $D^{*+} \rightarrow \pi^+ D^o$, one must operate where D^{*+} momenta exceeed 1 GeV/c . For this reason, the data reported here come from data collected at center-of-mass energies from 5 to 7.8 GeV. This sample represents a total integrated luminosity of 17,000 nb^{-1} .

Figure 1 shows the $K\pi$ invariant mass distribution for neutral $K\pi$ pairs with momentum exceeding 1.5 GeV/c . In this analysis we employ a previously described time - of - flight weighting algorithm (Goldhaber 76) , rather than the track tagging algorithm described earlier. Under this weighting technique, each track is assigned a weight for being a pion, kaon , or proton, computed from the measured time of flight, T_M , and the time-of-flight expected $(T_i^e$) from the
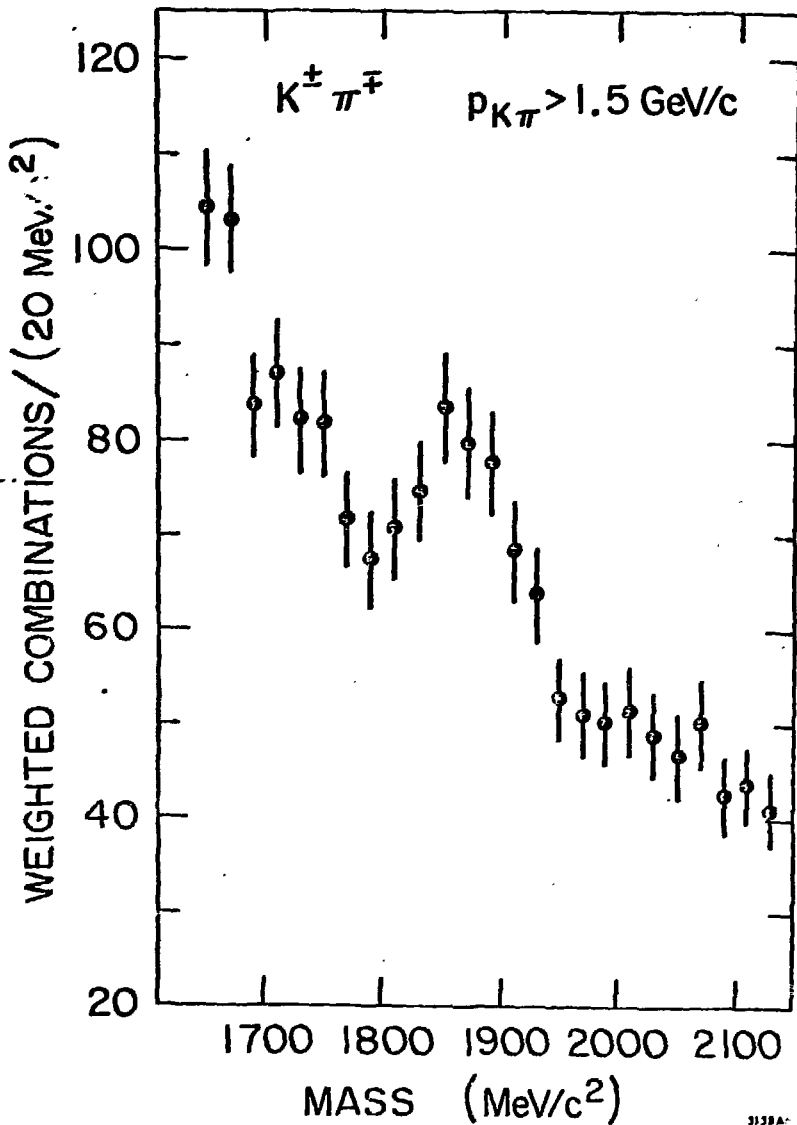
Fig. 1

D^o signal in data collected above
E_{cm} = 5 GeV. Here we require P_D 1.5
GeV.
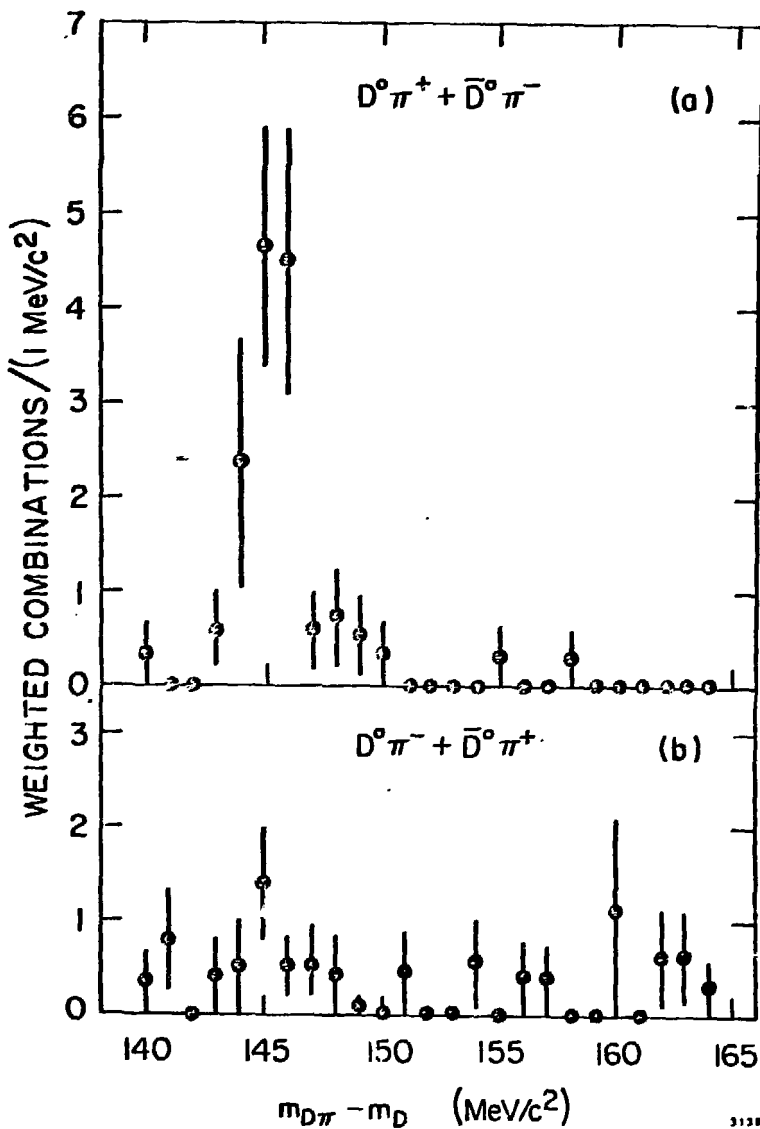
Fig. 2

D^{*+}, D^0 Mass difference plot. D^0's
are selected by requiring their invariant
mass to lie from 1820 - 1910 MeV/c².

measured momentum and flight path   under the given mass hypothesis. The
weight is computed via the expression:

$$W_i \propto \exp \left[-\frac{1}{2} \left(\frac{T_M - T_i^e}{0.35} \right)^2 \right]$$

with W_i normalized such that : $\Sigma \ W_i = 1$, $i = \pi, K, P$.
One can then construct histograms, say the $K\pi$ invariant mass histogram ,
for example, by entering in a given neutral two prong combination with
a weight given by $W_K^1 \ W_\pi^2$. The same two prong combination will enter
the histogram under the assumption that particle 2 is the kaon and
particle 1 is the pion with a new weight $W_\pi^1 \ W_K^2$.

   We see clear evidence for high momentum D^0 production in the data
of Figure 1 . In fact the signal to background is improved by requiring
$P_K > 1.5$ GeV/c. The signal of Figure 1 is considerably broader than
that of Figure 1 of Chapter 3 . This broadening is due to the effects
of $K\pi$ interchange in the calculation of the $K\pi$ invariant mass.
For D^0 's with momenta exceeding 1.5 GeV/c, such $K\pi$ interchange can
cause the computed $K\pi$ invariant mass to shift by nearly 200 MeV/c^2.

   In Figure 2 a and b we show the $D^0 \ \pi^+$ and $D^0 \ \pi^-$ invariant mass
plot. Because the calculation of $M_{D^0 \pi^\pm}$ is dominated by the mass that
one assumes for the D^0 , we plot $M_{D^0 \pi^\pm} - M_{D^0}$ rather than $M_{D^0 \pi^\pm}$.
For this plot we require the D^0 candidate to have a $K\pi$ invariant mass
from 1820 to 1910 MeV/c^2. This mass cut is considerably narrower than
the signal seen in Figure   1 , and hence tends to exclude D^0 candidates
with transposed pion and kaon. A clear peak is seen in the $D^0 \ \pi^+$ mass
difference plot (Figure 2) at $M_{D\pi} - M_{D^0} \approx 145.3 \pm .5$ MeV/c^2 .

Using a nominal D^0 mass value of 1865 MeV/c^2 we find that this peak corresponds to a D^{*+} mass value of 2010 MeV/c^2. This agrees very well with the position of the D^{*+} recoil peak of Figure 1c in Chapter 6. The width of the signal is completely consistent with the resolution of the Magnetic Detector, and serves to set an upper limit on the natural width of the D^{*+} (or D^0) of $\Gamma < 2.4$ MeV/c^2 (90% C.L.) . By comparing the area of the D^0 signal of Figure 2a with the area of the peak of Figure 1, and taking into account the $D^0 \pi^+$ detection efficiency, we estimate that 25 ± 9 % of all D^0's produced with Ecm from 5 to 7.8 GeV and having momentum exceeding 1.5 GeV/c come from the process $D^{*+} \rightarrow \pi^+ D^0$.

A. Limits on $D^0 - \overline{D}^0$ Mixing Effects

The observation of a strong D^{*+} signal in the $D^0 \pi^+$ invariant mass distribution of Figure 2a , and its absence in the $\overline{D}^0 \pi^+$ invariant mass plot of Figure 2b, can be used to set limits on the presence of $D^0 - \overline{D}^0$ mixing effects , a topic receiving considerable attention in the literature (Weinberg 77). Barring the presence of first order, neutral $|\Delta C| = 2$, weak currents, mixing would proceed via virtual Cabibbo suppressed intermediate states, such as $D^0 \rightarrow \pi^+ \pi^- \rightarrow \overline{D}^0$ and hence mixing amplitudes would be on the order of $\tan^2 \theta_{Cabibbo}$ (Gaillard 75) . If , on the other hand, first order charm changing neutral currents existed, $D^0 - \overline{D}^0$ mixing would be nearly complete (i.e. the characteristic time it would take a D^0 to mix into a $\overline{D}^0$ would be considerably shorter than the D^0 lifetime) .

The data of Figure 2 clearly rule out complete mixing , since

complete mixing implies that there should be as many D^{*+} 's observed in a $\pi^+ K^- \pi^+$ (1865) plot as in a $\pi^- K^- \pi^+$ (1865) invariant mass plot. A quantitative measure of possible mixing effects is provided by the mixing ratio , F_M , which we define as:

$$F_M = \frac{N [D^{*+} \to (K^+ \pi^-) \pi^+]}{N[D^{*+} \to (K^+ \pi^-) \pi^+] + N[D^{*+} \to (K^- \pi^+) \pi^+]}$$

where the particles in parentheses are required to be consistent with D^0 's . We find 38 events within $\pm$ 2.5 MeV/c^2 of the peak in Figure 2 a and 11 events within the peak of Figure 2 b. Here we count any combination with a weight greater than 0.1 as an event. After imposing the additional time-of-flight requirement that the K and π , comprising the D^0 have been correctly identified is at least three times the probability that they have been interchanged, the 38 events drops to 26 events, but the 11 events drop to only 3. These latter 3 events are consistent with coming from known background and instrumental effects. We expect 1.4 events from background (i.e. uncorrelated) particle combinations and 0.6 events from residual Kπ interchange. Thus at the 90% confidence level we find $F_M < 16\%$ (Feldman 77)

It is of interest to compare this measurement of $D^0 - \overline{D}^0$ mixing to an independent measurement based on the lack of apparent strangeness violation in events containing a K π (1865) candidate. By apparent strangeness violating events , we mean events with kaons in the recoil sysetem having the same charge as the kaon in the D^0 decay products. Barring mixing, one expects the kaon due to the D^0 decay to be of the

opposite charge as the kaon of the $\overline{D}^0$. This is because the GIM
mechanism favors D^0's decaying into final states containing a K^-, and
$\overline{D}^0$'s decaying into final states containing a K^+. If, on the other hand,
a significant numer of D^0's convert to $\overline{D}^0$'s before decaying , there
will be events with two kaons of the same charge. An additional source
for these events are doubly Cabibbo forbidden decays were the D^0 decays
into a state containing a K^+ rather than a K^-. This will occur on the
level of $\tan^4\theta_{Cabibbo}$ or 2×10^{-4} and is negligible compared to the
statistical accuracy of this measurement.

In order to obtain a purified sample of D^0 's we use $K\pi$ pairs
selected by our standard time-of-flight technique subject to
simultaneous cuts in invariant and recoil mass. We require masses
to lie between 1820 and 1900 MeV/c^2, with recoil masses lying in one of
four bands $1840< M_{rec}< 1900$, $1960< M_{rec}< 2080$, $2120< M_{rec}< 2220$, or
$M_{rec} >2390$. We find a sample of 423 $K\pi$ combinations satisfying these
cuts in the data taken from 3.9 to 4.60 GeV center-of-mass energy.
We estimate that 61% of these combinations are signal (s) , and 39% are
background (b). Within this sample, we find 77 events with one track
classified as a kaon in the recoil system. The below table summarizes
our knowlege of the charges of tracks in the recoil system. We denote
the charge of the tagged kaon in the D^0 as Q_K^D .

	π	K
$Q = Q_K^D$	425	15
$Q = -Q_K^D$	308	62
	733	77

Hence, of the 77 events with a track classified as a kaon in the recoil system, 62 kaon tracks had the opposite charge as the kaon from the D^0, while 15 had the same charge. Defining an asymmetry A_{s+b} equal to the difference of these numbers over their sum we find:

$$A_{s+b} = \frac{62 - 15}{77} = .61 \overset{+}{-} .11$$

We have performed the same analysis for background $K\pi$ combinations taken from two 50 MeV/c^2 sidebands on both sides of the 1865 peak and find $A_b = .37 \overset{+}{-} .12$. Because the background events presumably conserve strangeness, the observation that $A_b < A_{s+b}$ may appear surprising. In fact, the low value for A_b is due to track misidentification by the time-of-flight system. A major D^0 background source are $\pi^+ \pi^-$ pairs with one pion identified as a kaon by the tagging algorithm. This source would be expected to have $A_b = 0$, whereas the portion of the background due to real $K\pi$ pairs will have an A_b near 1. The value $A_b = .37$ then, represents an averaging over the two types of background. If, in fact, $D^0 - \bar{D}^0$ mixing is small, it is quite reasonable that $A_b < A_{s+b}$, since tagged $K\pi$ pairs in the signal region are more likely to contain real kaons.

Using the expression:

$$A_s = \frac{A_{s+b} - f_b A_b}{f_s}$$

with signal and background fractions given by $f_s = .61 \overset{+}{-} .02$ and $f_b = .39 \overset{+}{-} .02$ we obtain a signal asymmetry of $A_s = .76 \overset{+}{-} .19$ which is 4.5 standard deviations from 0 , the value for complete $D^0 - \bar{D}^0$ mixing.

In establishing an upper limit on the strangeness violating fraction F_v , it is important to estimate how often one would get apparent violation due to faulty K identification by our time of flight technique. This number depends on such factors as the track momentum distribution, the number of pions in the recoil system, and the number of D's decaying via K_s , K_L . In order to gauge these effects , we have estimated an intrinsic asymmetry A^* which would be the observed asymmetry expected for purely strangeness conserving events for two different Monte Carlo models. Both Monte Carlo models simulate charm production at 4.028 GeV via the three processes : $e^+ e^- \rightarrow D^0 \bar{D}^0$, $D^0 \bar{D}^{*0}$, and $D^{*0} \bar{D}^{*0}$ using masses and fraction determed by fits to the recoil spectrum discussed in Chapter 8. For each simulation, the D^0 decayed via $K\pi$ with the $\bar{D}^0$ decaying into the channels shown under the column headed " Recoil System". The topologies of the model recoil systems were chosen to roughly match the observed prong multiplicity and momentum spectrum. In addition to computing the Monte Carlo asymmetry, we have computed the fraction of tracks which are kaons (K_f) , and a quantity ξ equal to the total number of recoil tracks (π's and K's) with charge equal to Q_K^D minus the total number of tracks with charge equal to $-Q_K^D$ over the total number of tracks irrespective of charge.

	π	Model 1 K	Recoil System
$Q = Q_K^D$	1100	52	$1/2\ K^+\pi^-\pi^+\pi^-$
$Q = -Q_K^D$	566	337	$+1/2\ K^+\pi^-\pi^0\pi^0$
$A_1^* = .73 \overset{+}{-} .04$		$K_f = .19 \overset{+}{-} .01$	$\xi = .12 \overset{+}{-} .02$

Model 2

	π	K	Recoil System
$Q = Q_K^D$	1093	26	$1/4\ K^+\pi^-\pi^+\pi^-\ +\ 1/8\ K_S\pi^0\pi^0\pi^0$
$Q = -Q_K^D$	821	173	$+1/4\ K^+\pi^-\pi^0\pi^0\ +\ 1/8\ K_L\pi^0\pi^+\pi^-$
			$+1/8\ K_S\pi^0\pi^+\pi^-\ +\ 1/8\ K_L\pi^0\pi^0\pi^0$

$$A_2^* = .74 \overset{+}{-} .05 \qquad K_f = .094 \overset{+}{-} .01 \qquad \xi = .059 \overset{+}{-} .021$$

The quantity ξ is related to the difference in K,π acceptance due to the effects of K decays in flight (it is zero when K decay is negligible). For the data, these quantities are $A_S = .76 \overset{+}{-} .17$, $K_f = .095 \overset{+}{-} .010$, $\xi = .09 \overset{+}{-} .05$ which is in substantial agreement with Model 2 (we neglect the background subtraction for K_f and ξ). The happy fact is that the intrinsic asymmetries A^* are quite stable.

We can now estimate the strangeness violating fraction F_V . We note that the observed signal asymmetry is the average of the conserving asymmetry and the violating asymmetry weighted by their respective signal fractions. For the conserving decays the Monte Carlo predicts an asymmetry A^* which is weighted by $1 - F_V$. For violating decays , the recoil kaon charge is reversed, creating an asymmetry of $- A^*$, which is weighted by F_V . Hence $A_S = (1 - F_V)\ A^* - F_V\ A^*$.
Thus : $F_V = 1/2\ (\ 1 - A_S\ /\ A^*\ ) = -.014 \overset{+}{-} .117$ where the error on A^* incorporates statistical Monte Carlo error only. Going out 1.6 standard deviations we obtain a 90% C.L. upper limit of $F_V < .17$.

The precise relationship between F_V and F_M depends in detail on the D^0 production mechanism. Naively one would expect $F_V = F_M$ for processes of the form $e^+ e^- \to D^0\ D^-\ X^+$ and $F_V = 2\ F_M\ (1 - F_M)$ for processes

of the form $e^+ e^- \rightarrow D^0 \bar{D}^0 X^0$. Here X refers to the rest of the final state. This is because F_M is a direct measure of the probability that a D^0 will mix into a $\bar{D}^0$ within its lifetime. For final states of the type $D^0 D^- X^+$ there is only one D^0 which can mix to create an apparent strangeness violation, while for $D^0 \bar{D}^0 X^0$ there are two D^0 's.

This reasoning is wrong because it neglects the $D^0 - \bar{D}^0$ interference effects possible in $e^+ e^- \rightarrow D^0 \bar{D}^0 X^0$ when X^0 is an eigenstate of C parity. For example , Kingsly shows that if C (X^0) = +1 , as would be the case for $e^+ e^- \rightarrow D^0 \bar{D}^0 \pi^0 \pi^0$, $F_V = F_M$ rather than 2 $F_M(1 - F_M)$ once proper account is taken of the D^0 , $\bar{D}^0$ antisymmetrization. (Kingsly 76)

We have insufficient data to fully analyze the D^0 production mechanism over the full data sample from 4.9 to 4.6 GeV center-of-mass energy, and hence will adopt the most conservative assumption that $F_M = F_V$. Under this assumption our 17% upper limit on F_V serves as an upper limit on F_M . Combining the independent information on F_V and F_M we compute a slightly better upper limit of $F_M < 13$ % (90% C.L) .

8.   ANALYSIS OF THE D^0, D^+ MOMENTUM

SPECTRA AT Ecm = 4.028 GeV

As discussed in Chapter 6   charm meson production at Ecm = 4.028 GeV appears to be dominated by two-body processes such as the charged and neutral versions of:

$$e^+e^- \to D\bar{D} \qquad\qquad \text{Reaction 1}$$
$$D\bar{D}^* + \bar{D}D^* \qquad\qquad \text{Reaction 2}$$
$$D^*\bar{D}^* \qquad\qquad \text{Reaction 3}$$

These mechanisms were deduced from the structure observed in the recoil mass spectra against the D^0 and D^+ shown in Figure 1 of Chapter 6. In this Chapter we quantitatively analyze this structure in order to learn information on the masses of the D and D* mesons, the decay mechanisms of the D*'s, and the relative rates of reactions 1-3.   For this purpose it is convenient to fit momenta spectra at fixed energy rather than recoil spectra.   The momentum variable offers the advantage that momentum resolution is uniform to ±10% over the full range of D momenta   considered, whereas the recoil mass resolution is highly non-uniform.   Before describing the details and results of the momentum spectra fits, we will present the D^0 and D^+ momentum spectra and show that considerable information on D and D* masses can be obtained through just a visual inspection of the data.

A.   The D^+, D^0 Momentum Spectrum

In Figure 1 we show the D^0 (Fig. 1 a) and D^+ (Fig. 1 b) momentum
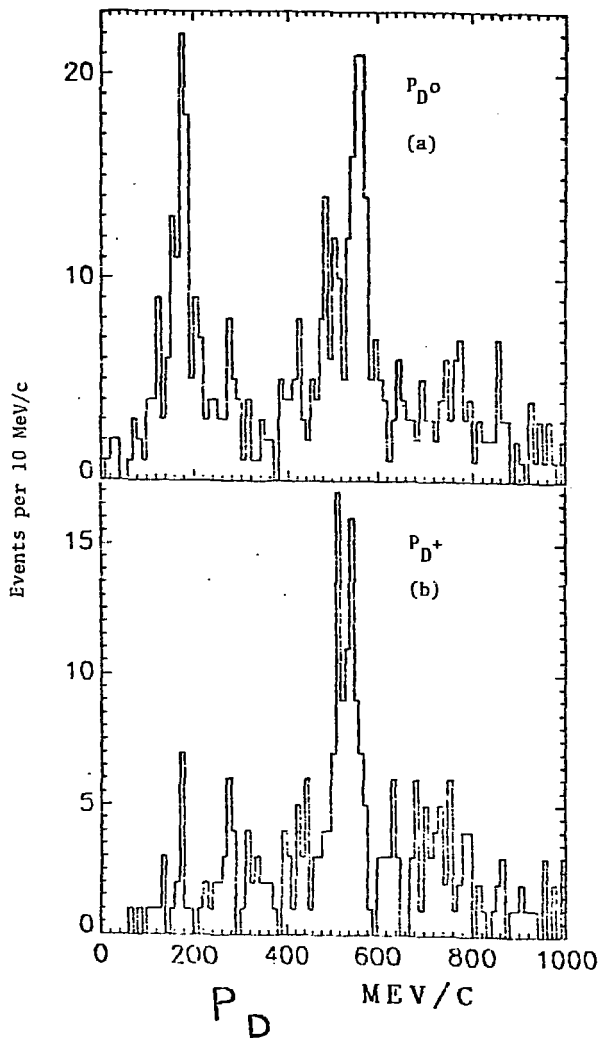
Fig. 1

Momentum spectrum of the D^0 (Fig. a) and
the D^+ (Fig. b) at the fixed energy of
Ecm = 4.028 GeV.

spectrum for data collected at the fixed energy of Ecm = 4.028 GeV. Our D^0, and D^+ selection procedures have been described in Chapter 4 D^0's are obtained from their two-body decay $D^0 \to K\pi$ and D^+'s are obtained through their three-body decay $D^+ \to K\pi\pi$. The D^0 spectrum of Fig. 1a is dominated by two striking peaks. We attribute the first peak, centered at 175 ± 10 MeV/c, to $D^{*0}\bar{D}^{*0}$ production, where $D^{*0} \to \pi^0 D^0$. The second peak, centered at 560 ± 10 MeV is presumably due to $\bar{D}^{*}D^0$ production.

The position of the first peak, which we denote as P_1, provides an accurate measure of the D^{*0} mass. The narrowness of this peak implies that the $Q(= M_{D^{*0}} - M_{D^0} - M_{\pi})$ value for the $D^{*0} \to \pi^0 D^0$ decay must be small compared to the D^{*0} or D^0 mass. Hence the lab velocity of a D^0 from the reaction $D^{*0} \to \pi^0 D^0$ must be quite close to that of the parent D^{*0} or $P_{D^*} = M_{D^{*0}}/M_{D^0} P_1$ where P_{D^*} is the momentum of D^*'s produced via reaction 3. These D^{*0}'s have an energy of Ecm/2, thus a mass given by:

$$M_{D^{*0}} = \sqrt{\frac{1}{4} E_{cm}^2 - \left(\frac{M_{D^{*0}}}{M_{D^0}}\right)^2 P_1^2} \qquad \text{Eqn. 1}$$

Although Eqn. 1 depends on the mass of the D^{*0} and D^0, the dependence is sufficiently weak that nominal values of $M_{D^{*0}} \approx 2005$ MeV/c^2 and $M_{D^0} = 1865$ MeV/c^2 can be safely used. Inserting our value $P_1 = 175 \pm 10$ MeV/c^2 into Eqn. 1, we find $M_{D^{*0}} = 2005 \pm 3$ MeV/c^2. The error is dominated by the ±4 MeV uncertainty on Ecm.

The position of the $D^*\bar{D}$ peak at $P_2 = 560 \pm 10$ MeV/c provides an estimate for $M_{D^{*0}} + M_{D^0}$. One can write the expression for P_2 in terms of the relevant masses and energies as:

$$P_2 = \left[\frac{\left[E_{cm}^2 - (M_{D*0} + M_{D0})^2\right]\left[E_{cm}^2 - (M_{D*0} - M_{D0})^2\right]}{4 \ E_{cm}^2}\right]^{1/2}$$

Assuming $M_{D*0} - M_{D0} < E_{cm}$, this expression can be simplified and rearranged to yield:

$$M_{D*0} + M_{D0} = \sqrt{E_{cm}^2 - 4P_2^2} \qquad \text{Eqn. 2}$$

Using $P_2 = 560 \pm 10$ MeV/c we estimate that $M_{D*0} + M_{D0} = 3869 \pm 6$ MeV/c .

The D^+ momentum spectrum shown in Fig. 1 is dominated by a single peak, centered at a momentum of $P_3 = 535 \pm 10$ MeV/c which we attribute to $D^{*+}D^-$ production. Using the charged analogue of Eqn. 2 we find $M_{D*+} + M_{D+} = 3883 \pm 6$ MeV/c^2.

Hence, from the positions of the three prominent peaks of Fig. 1 a and b, and the observation of the reaction $D^{*+} \rightarrow \pi^+D^0$, discussed in Chapter 7 we have learned:

$$M_{D*+} - M_{D0} = 145.3 \pm .5$$
$$M_{D*0} = 2005 \pm 3$$
$$M_{D*0} + M_{D0} = 3869 \pm 6$$
$$M_{D*+} + M_{D+} = 3883 \pm 6 .$$

These relationships imply crude mass values of:

$$M_{D0} = 1864 \pm 7 \qquad\qquad M_{D+} = 1875 \pm 8$$
$$M_{D*0} = 2005 \pm 3 \qquad\qquad M_{D+*} = 2009 \pm 6$$

and Q values of

$$Q(D^{*0} \to D^0\pi^0) = 6 \pm 8 \qquad\qquad Q(D^{*+} \to D^+\pi^0) = 0 \pm 10$$

$$Q(D^{*0} \to D^+\pi^-) = -9 \pm 9 \qquad\qquad Q(D^{*+} \to D^0\pi^+) = 5.7 \pm .5$$

where all quantities are in MeV/c^2.

The mass values quoted here are in excellent agreement with the values which will be deduced from the complete fit to be discussed shortly. However the values from the complete fit have about 1/2 the errors of these crude values since they use information on the shape of the various peaks as well as their positions.

There are clear indications in the data for the presence of $D^{*0} \to D^0\pi^0$ and $D^{*+} \to D^0\pi^+$. The $D^{*+} \to \pi^+D^0$ decay has been directly observed as discussed in Chapter 7 while the presence of a narrow $D^{*0}\bar{D}^{*0}$ peak in the data of Fig. 1 strongly suggests the presence of $D^{*0} \to \pi^0D^0$. We note that there is the barest hint of a D^+ peak near 200 MeV/c in the data of Fig. 1b. Such a peak, if existing at all, could be due to either $e^+e^- \to D^{*+}D^{*-}$; $D^{*+} \to \pi^0D^+$ or possibly to $e^+e^- \to D^{*0}\bar{D}^{*0}$; $D^{*0} \to \pi^-D^+$. We note that the preliminary Q value for the latter reaction is negative by about 1 standard deviation. The more accurate mass values obtained in the complete fit show that the Q value is negative by about 2 standard deviations. Hence this D^{*0} decay mode is probably kinematically forbidden. In addition, the data of Fig. 1a argues for a substantial amount of $D^{*0}\bar{D}^{*0}$ production. Unless $Br(D^+ \to K^-\pi^+\pi^+)/Br(D^0 \to K^-\pi^+)$ is considerably less than 1, one would expect that the number of D^+ events in the 200 MeV/c peak of Fig. 1b would favorably compare with the number of D^0 in the 200 MeV/c peak of Fig. 1a , if the reactions $D^{*0} \to \pi^-D^+$ and

$D^{*0} \to \pi^0 D^0$ occur at comparable rates. In fact, statistical model estimates (Jackson 76) favor $Br(D^+ \to K^-\pi^+\pi^+)/Br(D^0 \to K^-\pi^+)$ values exceeding 1, thus the smallness (or non-existence) of a D^+ momentum peak near 200 MeV suggests that at best $D^{*0} \to \pi^- D^+$ is a minor decay mode of the D^{*0}. The D^{*0}, D^+ mass values obtained through the fit favor excluding it completely.

We have thus seen that there is considerable information in Fig. 1 We have used the positions of the 3 prominent peaks to deduce the masses of the D^0, D^+, D^{*0}, and D^{*+}. The relative area of the $D^{*0}\bar{D}^{*0}$ and $D^{*0}\bar{D}^0$ peaks of Fig. 1a suggests that these reactions occur with comparable rates and dominate D^0 production at Ecm = 4.028 GeV. There is a small peak at 750 MeV/c in Fig. 1a, which, if present, would be due to $D^0\bar{D}^0$ production, but clearly this must be a minor source of D^0 production.

In this next section we discuss the expected shapes of the various contributions to the D^0, D^+ spectrum as a prelude to discussing the complete D^0, D^+ spectral fit.

B. The Shape of Contributions to the D^0, D^+ Momentum Spectra

We begin by analyzing the expected shapes of the various contributions to the D momentum spectrum in the limit of perfect detector resolution. These shapes can then be later folded with an appropriate resolution function to obtain realistic shapes which incorporate momentum uncertainties.

The various D sources can be characterized as direct sources and secondary sources from D^* decays. Neglecting any natural width for the D and D^*, direct sources such as $e^+e^- \to D\bar{D}$ will provide delta function
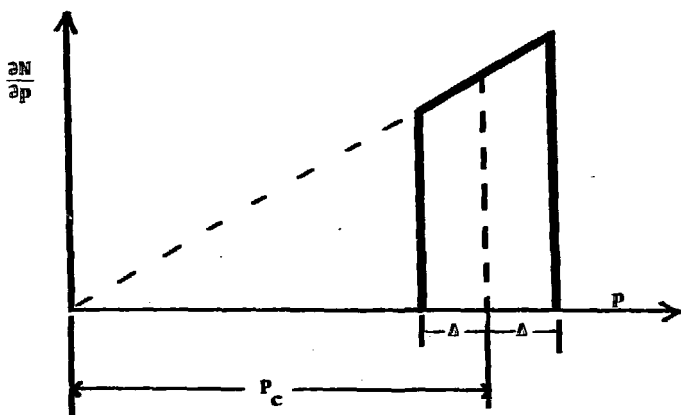
Fig. 2

Momentum spectrum for secondary D 's arising
from isotropic two-body D* decays.

contributions to the D momentum spectrum. The shape of the momentum spectrum of D's from secondary sources such as $D^* \to \pi D$ or $D^* \to \gamma D$, can be deduced from the polar angular distribution of D's in the D^* helicity frame. For example, isotropic D^* decay distributions produce the ramped, secondary-D momentum spectrum illustrated in Fig. 2. From the Lorentz transformation $E_D = \gamma(E_D{}' + P_D{}'\beta\cos\theta')$ where γ and β are boost parameters appropriate to the D^* lab velocity, we see that a flat $\cos\theta'$ distribution implies a flat D energy distribution. This implies a linear D-momentum distribution since $dN/dp = dN/dE \; dE/dp$ and $dE/dp = p/M_D$ (for non-relativistic D's).

If one assumes that the D is a pseudoscalar and the D^* is a vector as suggested by the conclusion of Chapter 9 the two D^* decay angular distributions can be computed for D production via reaction 2 as shown in Appendix 2. The D^* decay distribution for D^*'s produced via reaction 3, however, cannot be computed from first principles. For computational simplicity, we have calculated the spectral shapes for secondary D's assuming isotropic D^* decay angular distributions for both $D^* \to \gamma D$ and $D^* \to \pi D$. A comparison of the spectral shapes so obtained with a Monte Carlo simulation employing the correct (anisotropic) D^* decay distributions for D's produced via reaction 2 will show that this is an excellent approximation.

Monte Carlo simulations show that the D^0 and D^+ momentum resolution functions for a given momentum is well represented by a sum of two Gaussian distributions of different widths. We have deduced the momentum resolution functions by performing high statistics simulations for D^0's and D^+'s produced at momenta of 180, 550, and 760 MeV/c. The following table gives the

widths (σ_i) of the two Gaussians and their respective weights (a_i). It was obtained by fitting the simulated momentum spectrum to a sum of two Gaussians.

Table 1

	P	a_1	σ_1	a_2	σ_2
D^0	180	0.33	9.7	.67	18.9
	550	0.26	30.0	.74	16.5
	760	0.39	31.0	.61	18.0
D^+	180	0.52	13.3	.48	21.4
	550	0.58	12.6	.42	21.8
	760	0.71	14.5	.29	26.2

The three momenta of 180, 550, and 760 MeV/c were chosen to correspond to typical D momenta for D's produced via $D^*\bar{D}^*$, $D\bar{D}^*$, and $D\bar{D}$. In computing the folded spectral shape for a given process we use the most appropriate of the 6 resolution functions. That is, even though the ramped distribution for D secondaries from $D^* \to \gamma D$ extends over a momentum range of nearly 300 MeV/c, we fold the ramp with the resolution function appropriate to the ramp's center rather than a function with a continuously variable Gaussian width.

Direct D^0's have a normalized momentum spectrum given by the appropriately displaced resolution function or:

$$D(P) = \sum_{i=1}^{2} \frac{a_i}{\sigma_i \sqrt{2\pi}} e^{-\frac{1}{2}\left(\frac{P-P_c}{\sigma_i}\right)^2}$$

Eqn. 3

where a_i is the weight of the term in the resolution function of width σ_i and P_c is the position of the direct D^0 momentum peak. Secondary D^0's produced under the assumption of isotropic D^* decay have a momentum spectrum given by:

$$D(P) = \int_{P_c - \Delta}^{P_c + \Delta} dP' \frac{P'}{2\Delta P_c} \sum_{i=1}^{2} \frac{a_i}{\sigma_i \sqrt{2\pi}} e^{-\frac{1}{2}\left(\frac{P-P'}{\sigma_i}\right)^2}$$

where P_c and Δ are defined in Fig. 2. Performing this integral we obtain:

$$D(P) = \frac{1}{2\Delta P_c} \sum_{i=1}^{2} a_i [S(P, P_c + \Delta, \sigma_i) - S(P, P_c - \Delta, \sigma_i)]$$

where

$$S(x, \alpha, \sigma) = \frac{x}{2} \, \text{Erf} \, \frac{\alpha-x}{\sqrt{2}\sigma} - \frac{\sigma}{\sqrt{2\pi}} e^{-\frac{1}{2}\left(\frac{\alpha-x}{\sigma}\right)^2}$$

and

$$\text{Erf}(y) = \frac{2}{\sqrt{\pi}} \int_{0}^{y} dy' \, e^{-y'^2}$$

Eqn. 4.

We note that both Eqn. 3 and Eqn. 4 are normalized such that

$$\int_{-\infty}^{\infty} D(p) \, dp = 1$$

The complete D momentum spectrum due to reactions 1-3 can be written as a linear combination of the functions given in Eqns. 3 and 4. In general the values of Δ and P_c are relatively complicated functions of the relevant masses and energies. However, considerable simplification in these expressions occurs near threshold where the problem is essentially non-relativistic.

We consider a D* of mass M* and momentum P* decaying into a D of mass M by either $D* \to \gamma D$ or $D* \to \pi D$. Non-relativistically, the D laboratory momentum $\vec{P}$ is $\vec{P} = (M/M*)(\vec{P*}) + \vec{P'}$, where $\vec{P'}$ is the momentum of the D in the D* rest frame. Provided that $|\vec{P'}|/M \leq |\vec{P*}|/M*$, one notes that

$$\frac{M}{M*}|\vec{P*}| - |\vec{P'}| < |\vec{P}| < \frac{M}{M*}|\vec{P*}| + |\vec{P'}|.$$

From the definition of P_c and Δ we see: $P_c = (M/M*)|\vec{P*}|$ and $\Delta = |\vec{P'}|$.

For $D* \to D\pi$, $\vec{P'}$ can be computed from non-relativistic energy conservation:

$$\frac{|\vec{P'}|^2}{2M_\pi} + \frac{|\vec{P'}|^2}{2M} = M - M* - M_\pi \equiv Q_\pi.$$

Thus:

$$\Delta = |\vec{P'}| = \sqrt{\frac{2M_\pi M}{M_\pi + M}} \quad \sqrt{Q_\pi} = 16\sqrt{Q_\pi} \qquad \text{Eqn. 5}$$

where Q_π and Δ are in MeV.

For $D* \to \gamma D$, $\vec{P'}$ is equal to the energy of the γ in the D* rest frame. Hence:

$$\Delta = |\vec{P'}| = \frac{M*^2 - M^2}{2M*} = \frac{M* + M}{2 M*} Q_\gamma = 0.97 Q_\gamma \qquad \text{Eqn. 6.}$$

We see from Eqns. 5 and 6 that the spectral half width Δ essentially measures the Q value for the given D* decay. In particular, we know Q_π for the reaction $D*^0 \to \pi^0 D^0$ is quite small (~ 5 MeV/c^2), and thus small changes in Q_π can greatly effect the width of the $D*^0 \bar{D}*^0$ peak. Changing Q_π from 5 to 6 MeV, for example, broadens the unfolded $D*^0 \bar{D}*^0$ full width by nearly 7 MeV/c. We estimate that the $D*^0 \bar{D}*^0$ peak of Fig. 1a has a full width of less than 100 MeV/c. Neglecting momentum resolution, this sets a conservative upper limit on Δ of 50 MeV/c and, using Eqn. 5, an upper
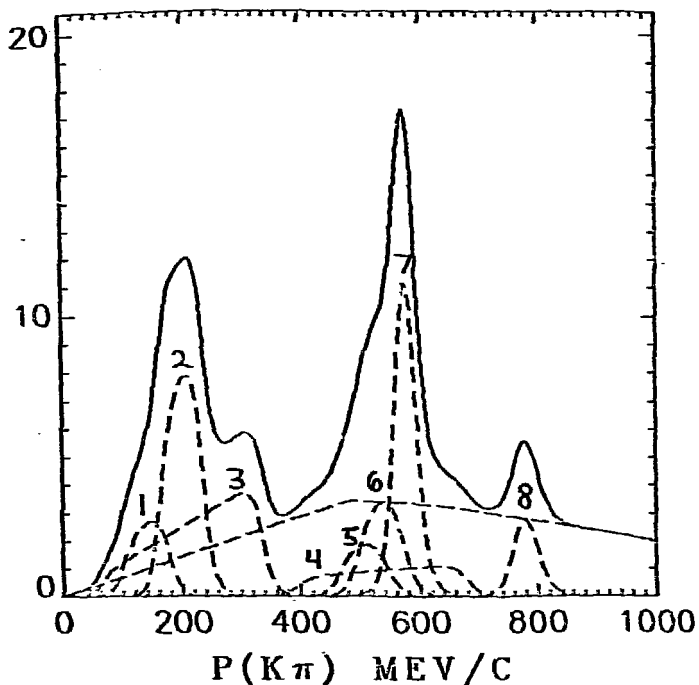
Fig. 3
Illustration of contributions to D^0 momentum
spectrum at E_{cm} = 4.028 GeV

$$e^+e^- \to D^{*+}D^{*-}, \quad D^{*+} \to \pi^+D^0 \qquad (1)$$

$$D^{*0}\bar{D}^{*0}, \quad D^{*0} \to \pi^0D^0 \qquad (2)$$

$$D^{*0}\bar{D}^{*0}, \quad D^{*0} \to \gamma D^0 \qquad (3)$$

$$D^{*0}\bar{D}^0, \quad D^{*0} \to \gamma D^0 \qquad (4)$$

$$D^{*+}D^-, \quad D^{*+} \to \pi^+D^0 \qquad (5)$$

$$D^{*0}\bar{D}^0, \quad D^{*0} \to \pi^0D^0 \qquad (6)$$

$$\bar{D}^{*0}D^0 \qquad \text{Direct } D^0 \qquad (7)$$

$$D^0\bar{D}^0 \qquad \text{Direct } D^0 \qquad (8)$$

Unlabeled dashed curve is the background.
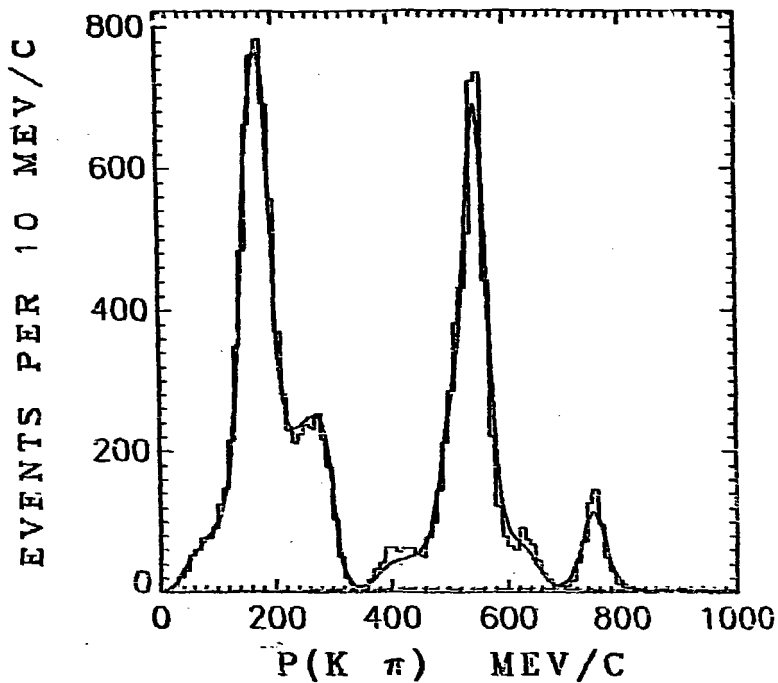
Fig. 4

Comparison of the fitting function to a full
high statistic Monte-Carlo.

limit on Q_π < 10 MeV/c^2 which is appreciably lower than previously obtained limit.

In Fig. 3 we show these various computed contributions to the D^0 momentum spectrum produced at Ecm = 4.028 GeV. The masses and areas of these contributions are typical of values obtained from the momentum spectrum fit, although we have adjusted them within errors for illustrative purposes.

In Figure 4 we use the expressions developed here to fit a Monte Carlo D^0 momentum spectrum. This simulation employed the proper D^* decay angular distributions for D^*'s produced via Reaction 2, although it was fit under the assumption of isotropic D^* decay. The simulation parameters were chosen to be close to our best estimates of the true parameters. The parameters returned by the fit were found to be in excellent agreement with those used in the simulation. We thus conclude that the fitting procedures must be relatively unbiased.

For the fits described in this Chapter we used a D^0 relative detection efficiency given by:

$$E_0(P) = \begin{cases} 1.20 & P \le 0.35 \text{ GeV/c} \\ 1.0 & P > 0.35 \text{ GeV/c} \end{cases}$$

and assumed that the D^+ detection efficiency is uniform over the full range in momentum. The success of the fit to the Monte Carlo spectrum, which automatically incorporates efficiency effects, shows that this somewhat arbitrary D^0 efficiency is adequate for our purposes. The 20% efficiency rise for low momentum D^0's reflects the fact that slow D^0's decay into nearly collinear $K\pi$ pairs which have higher geometrical efficiency than non-collinear pairs.

C. Backgrounds

The signal to background ratio for the D^0 candidates of Fig. 1a is 1 : 1, while that of the D^+ candidates of Fig. 1b is 1 : 2. It is possible to improve the D^0 signal to background ratio considerably by the use of the time-of-flight tagging algorithm described in Chapter For this analysis, however, we have boosted statistics by including D^0 candidates classified as "$K^+ K^-$" and "$\pi^+ \pi^-$" as well as $K\pi$.

Included as a contribution to Figure 3 is a smoothed momentum distribution appropriate to background $K\pi$ combinations which satisfy the D^0 selection criteria. The background momentum spectrum shown in Fig. 3 is of the form:

$$B(P) = \begin{cases} \dfrac{\Gamma_1^2 P/\mu}{4(P-\mu)^2 + \Gamma_1^2} & \text{For } P \leq \mu \\[3mm] \dfrac{\Gamma_2^2}{4(P-\mu)^2 + \Gamma_2^2} & \text{For } P > \mu \end{cases}$$

where μ, Γ_1, and Γ_2 are obtained from a fit to a sideband deduced background spectrum. The same functional form, with different values of μ, Γ_1, and Γ_2 serves as a D^+ background momentum spectrum.

D. The Loosely Coupled Fit

We have performed two basic fits of the joint $D^0 D^+$ momentum spectrum. The first of these fits, the "loosely coupled" fit, involves a minimal number of assumptions and hence a maximal number of free parameters. This joint D^0, D^+ fit is parameterized essentially in terms of the D^0, D^+, D^{*0} masses and the area under each of the various D^0, D^+ spectral contributions. The mass of the D^{*+} is computed from the known D^{*+},D^0 mass

Table 2.   Definition of loosely coupled fit area parameters

The area parameters are: F2N, F1N, F10, F2C, F1C, F10, BGN, BGC, and FD.
The fraction of non-background D^0's arising from sources is given below:

	Source	Fraction
1	$D^0\bar{D}^0$	F0N
2	$D^0\bar{D}*^0$	$\frac{1}{2}$ F1N
3	$\bar{D}^0D*^0$; $D*^0 \rightarrow \pi^0D^0$	$\frac{1}{2}$ (1 − BGN) F1N
4	$\bar{D}^0D*^0$; $D*^0 \rightarrow \gamma D^0$	$\frac{1}{2}$ (BGN) F1N
5	$D*^0\bar{D}*^0$; $D*^0 \rightarrow \pi^0D^0$	(1 − BGN) F2N (1.2)
6	$D*^0\bar{D}*^0$; $D*^0 \rightarrow \gamma D^0$	(BGN) F2N (1.2)
7	$D*^+D^-$; $D*^+ \rightarrow \pi^+D^0$	$\frac{1}{2}$ (FD) F1C
8	$D*^+D*^-$; $D*^+ \rightarrow \pi^+D^0$	(FD) F2C (1.2)

The fraction of non-background D^+'s arising from various sources is given
below:

	Source	Fraction
9	D^+D^-	F0C
10	D^+D*^-	$\frac{1}{2}$ F1C
11	D^-D*^+; $D*^+ \rightarrow \pi^0D^+$	$\frac{1}{2}$ (1 − BGC) F1C
12	D^-D*^+; $D*^+ \rightarrow \gamma D^+$	$\frac{1}{2}$ (BGC) F1C
13	$D*^+D*^-$; $D*^+ \rightarrow \pi^0D^+$	(1 − BGC) F2C
14	$D*^+D*^-$: $D*^+ \rightarrow \gamma D^+$	(BGC) F2C

The factor of 1.2 expresses the higher efficiency assumed for D^0's of
momentum less than 350 MeV/c.

Table 3. Results from simultaneous fits to the D^0, D^+ momentum spectra at $E_{cm} = 4.028$ GeV.

	Fit parameter	Loosely Coupled Fit	Tightly Coupled Fit	Estimated values
Masses in MeV/c²	m_{D^0}	1864 (1.5)[a]	1862 (0.5)[a]	1863 ± 3[b]
	m_{D^+}	1874 (2.5)	1873 (2.0)	1874 ± 5
	$m_{D^{*0}}$	2005 (0.5)	2007 (0.5)	2006 ± 1.5
	$m_{D^{*+}}$	2009 (1.5)	2007 (0.5)	2008 ± 3
Branching ratios	$BR(D^{*0} \to \pi D^0)$	0.45 (0.05)	0.75 (0.05)	0.55 ± 0.15
	$BR(D^{*+} \to \pi^+ D^0)$[c]	--	0.60 ± 0.15	--
	$\dfrac{BR(D^+ \to K^- \pi^+ \pi^+)}{BR(D^0 \to K^- \pi^+)}$[c]	--	1.60 ± 0.60	--
D^0 source fractions	$D^0 \bar{D}^0$	0.05 (0.03)	0.05 (0.02)	0.05 ± 0.03
	$D^0 \bar{D}^{*0} + \bar{D}^0 D^{*0}$	0.42 (0.04)	0.34 (0.04)	0.38 ± 0.08
	$D^{*0} \bar{D}^{*0}$	0.47 (0.05)	0.32 (0.05)	0.40 ± 0.10
	$D^{*+} D^- ; D^{*+} \to \pi^+ D^0$	0.03 (0.02)	0.09 (0.04)	0.06 ± 0.05
	$D^{*+} D^{*-} ; D^{*+} \to \pi^+ D^0$	0.03 (0.03)	0.20 (0.07)	0.11 ± 0.10
D^+ source fractions	$D^+ D^-$	0.05 (0.05)	0.09 (0.05)	0.09 ± 0.05
	$D^{*+} D^- + D^+ D^{*-}$	0.65 (0.07)	0.58 (0.06)	0.62 ± 0.09
	$D^{*+} D^{*-}$	0.26 (0.08)	0.33 (0.08)	0.29 ± 0.10

[a] Quantities in parentheses are statistical errors from the fitting process.

[b] Errors quoted include estimated systematic uncertainty.

[c] These values can only be obtained under the assumptions of the isospin constrained fit. The quoted errors do not reflect possible breakdown of these assumptions.

difference, $M_D^{*+} - M_{D^0} \approx 145.3$ MeV/c^2, which was obtained in Chapter 7.

The use of this relation naturally couples the D^0 and D^+ spectra and thus motivates a single joint D^0, D^+ spectral fit. The reaction $D^{*+} \rightarrow \pi^+ D^0$, which we call the "feed-down" reaction, provides a second reason. One expects <u>two</u> feed-down peaks, located in the D^0 spectrum near 200 MeV/c and 560 MeV/c for D^{*+}'s produced via the charged versions of Reactions 2 and 3. The widths of these peaks are equal and computable from the known D^{*+}-D^0 mass difference. The position of the Reaction 3 feed-down contribution is computable from the beam energy and the D^{*+} mass alone, while the position of the Reaction 2 feed-down contribution is sensitive to $M_{D^{*+}} + M_{D^+}$. This last quantity is essentially determined by the position of the peak near 550 MeV/c in the D^+ spectrum which provides a further reason for a combined D^0, D^+ spectral fit.

Other than the 3 independent mass values, the loosely coupled fit has 9 additional parameters describing the area under the various spectral contributions. In Table 2 we define these area parameters by using them to compute the fraction of D^0's and D^+'s arising from each of the fourteen D sources. With the exception of FD, these parameters have a physically transparent meaning. FD is a measure of the $D^{*+} \rightarrow \pi^+ D^0$ branching fraction multiplied by the ratio of branching fractions $BR(D^0 \rightarrow K^- \pi^+)/BR(D^+ \rightarrow K^- \pi^+ \pi^+)$.

We have performed this fit for a variety of starting parameters, resolutions, and background parameterizations. Typical results of this fit are presented in Table 3. The statistical errors on the mass values for a given loosely coupled fit are less than 1 MeV/c^2. However the systematic errors as judged by the different fits are typical of the errors quoted in column 3 of Table 1. For easy comparison with the "tightly
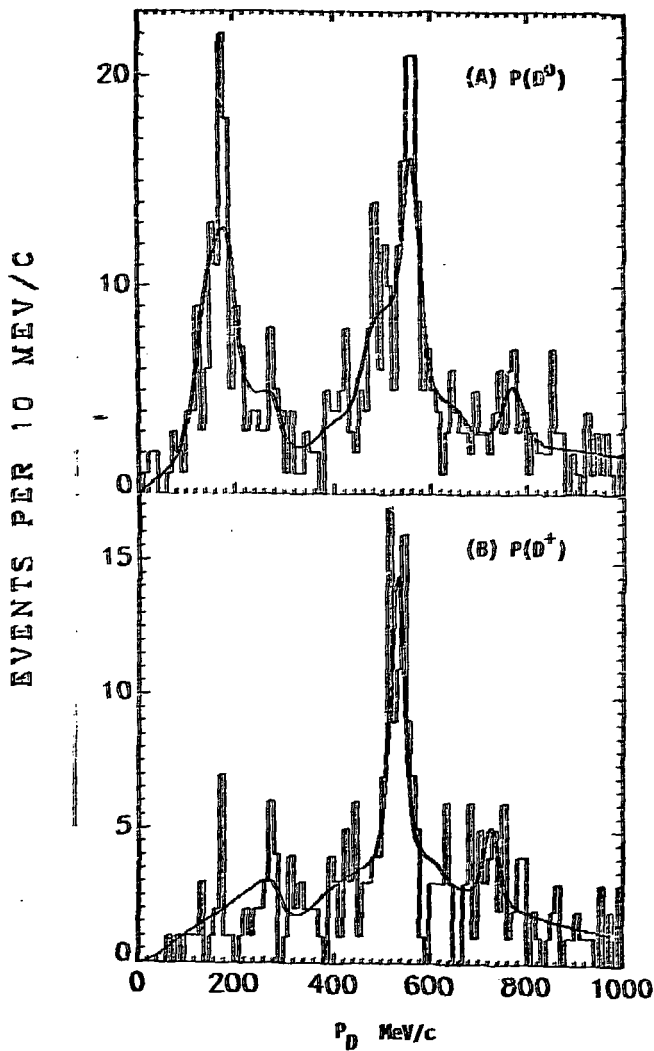
Fig. 5

Results of the simultaneous fits to the D^0, D^+
momentum spectrum at E_{cm} = 4.028 GeV

coupled" fit to be described shortly, we present the D^0, D^+ source fractions (normalized to unity) computed from the area parameters rather than the parameters themselves.

The fit is compared to the data in Figure 5. Although the fit has an acceptable overall χ^2 (typically 210 for 188 D.F.), it clearly has difficulty in matching the width of the $D^{*0}\bar{D}^{*0}$. The width of this peak is consistent with a $Q(D^{*0} \to \pi^0 D^0)$ value of ~ 2 MeV/c^2 rather than ~ 7 MeV/c^2 as indicated in Table 3. Such a discrepancy could arise from systematic mismeasurement of the D^0 momentum. Differentiation of Eqns. 1 and 2 show that the Q value discrepancy could be caused by an ~ 40 MeV/c systematic shift of the position of the $D^{*0}\bar{D}^{*0}$ peak or by an ~ 7 Mev/c shift in the position of the $D^{*0}\bar{D}$ peak, or by some combination of the two.

A systematic shift of ~ 7 MeV/c out of 560 MeV/c appears unreasonably large from instrumental considerations--a shift of ~ 40 MeV/c out of 175 MeV/c is out of the question. If one attributes the discrepancy to systematic mismeasurement of the $D^{*0}\bar{D}^0$ peak, the value of the D^0 mass would rise to 1869 MeV/c^2 rather than 1864 MeV/c^2. However, because of the $M_{D^{*+}} - M_{D^0}$ constraint, the $M_{D^{*+}}$ mass must rise to 2014 MeV/c^2, which puts $D^{*+}D^{*-}$ production at 4.028 GeV perilously close to threshold. As previously stated, there is evidence for substantial $D^{*+}D^{*-}$ production in contradiction to this solution. In light of these considerations, we favor the solution presented in the table.

The success of the "loosely coupled" fit in fitting the D^0, D^+ momentum spectrum shows that D production at Ecm = 4.028 GeV is dominated by the two-body processes of Reactions 1-3. In order to estimate the

$\dfrac{\partial N}{\partial P}$

200   400   600   P

MeV/c
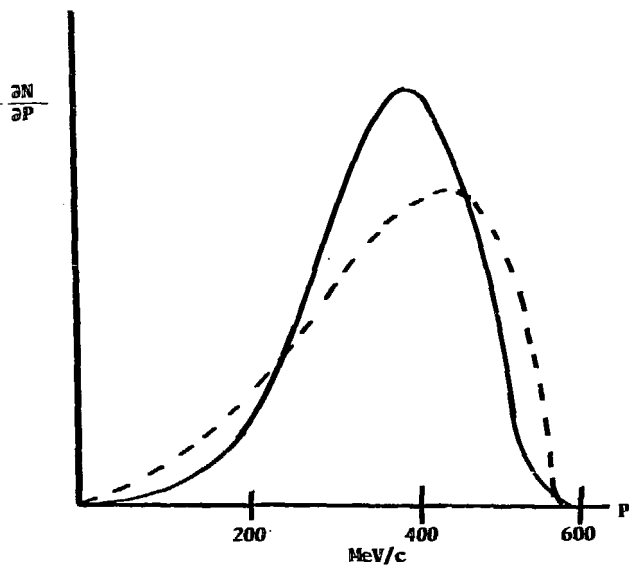
Fig. 6

Expected momentum spectrum for D's produced
via $e^+ e^- \rightarrow D \bar{D} \pi$ at Ecm = 4.028 GeV.
Dashed curve gives a phase space momentum
spectrum. Solid curve is computed with the
matrix element described in the text.

the presence of D production through multibody processes, we have performed a fit of the loosely coupled variety where we have included a spectral contribution from the process $e^+e^- \rightarrow D^0 \bar{D}^0 \pi^0$. The shape of this contribution is shown by the solid curve of Fig. 6. The dashed curve of Fig. 6 is a phase space distribution. The solid curve is obtained from the dashed curve through a multiplication of $|\vec{P}_1 \times \vec{P}_2|^2$, where $\vec{P}_1$ and $\vec{P}_2$ are the laboratory momenta of the D^0 and $\bar{D}^0$. This multiplicative factor causes the $D^0\bar{D}^0\pi^0$ Dalitz plot to be depopulated on the boundaries. As discussed in Chapter 5 such a boundary depopulation is required for a final state comprised of 3 pseudoscalars in the spin-parity state $J^P = 1^-$ (i.e. the spin-parity of the intermediate photon). Evidence that the D^0 is a pseudoscalar will be presented in Chapter 9.

The spectrum of Fig. 6 is seen to peak in the vicinity of 400 MeV/c in a region where experimentally there are at most a few D^0's above background. For this reason, this special loosely coupled fit prefers no $D^0\bar{D}^0\pi^0$ contribution and sets the 90% confidence level upper limit that less than 10% of D^0's produced at Ecm = 4.028 GeV are produced via $e^+e^- \rightarrow D^0\bar{D}^0\pi^0$. Three-body production due to $e^+e^- \rightarrow D^+D^0\pi^-$ would produce a spectrum very similar to that of Fig. 6 owing to the relative closeness of the D^0 and D^+ mass; hence the 10% upper limit applies to three-body production in general. D^0 production by four or more body processes should be negligible compared to three body production, in light of the exceedingly limited available phase space.

E. The Tightly Coupled Fit

The tightly coupled fit to the joint D^0, D^+ momentum spectra uses

various theoretical assumptions linking the areas of the various D^+ spectral contributions to those of the D^0 and thus reduces the number of free parameters. In this fit we use isospin considerations to relate the charged and neutral production cross sections for Reactions 1-3 and quark model considerations to relate the various D^{*+} decay branching ratios to those for the D^{*0}.

The tightly coupled fit allows one to estimate quantities which cannot be estimated from the loosely coupled fit. By relating total D^0 production to D^+ production, one obtains an estimate for the ratio of branching ratios: $BR(D^0 \to K^- \pi^+)/BR(D^+ \to K^- \pi^+ \pi^+)$. This ratio and the quark model assumptions allow one to estimate the D^{*+} feed-down branching ratio: $BR(D^{*+} \to \pi^+ D^0)$. Because this fit couples area information to mass information through phase space and angular momentum barrier factors, it provides an independent estimate of the quantities of Table 3. Comparison of the results of these two fits allows for estimates of the systematic uncertainties of the fitting procedure. Lastly, the success or failure of such a fit bears on the validity of the isospin and quark model assumptions.

Our first assumption is that, apart from phase space and angular momentum barrier considerations, $\sigma(D^0 \bar{D}^0) = \sigma(D^+ D^-)$, $\sigma(D^{*0} \bar{D}^0) = \sigma(D^{*+} D^-)$, and $\sigma(D^{*0} \bar{D}^{*0}) = \sigma(D^{*+} D^{*-})$. In the conventional charm model, the D and D^* are assumed to have even relative parity, and hence all three final states ($D\bar{D}$, $D\bar{D}^*$, and $D^* \bar{D}^*$) couple to the time-like photon in a P-wave. Thus angular momentum-phase space corrections follow a p^3 law, where p is the center-of-mass momentum of the D or D^*. Assuming that the (D^0, D^+) and (D^{*0}, D^{*+}) system form isodoublets, as expected in the conventional

charm model, our assumed equality of charged and neutral cross sections is equivalent to assuming that the D and D* are produced in states of pure $I = 1$ or $I = 0$ isospin. The equivalence of these assumptions can be easily seen by writing the amplitude for the charged and neutral versions of one of the Reactions 1-3 in terms of an isosinglet amplitude A_0 and an isotriplet amplitude A_1. Using the Condon and Shortley phase convention for the Clebsh-Gordon coefficients, we find:

$$A_{Charge} = \frac{1}{\sqrt{2}} \ (A_1 - A_0)$$

$$A_{Neutral} = \frac{1}{\sqrt{2}} \ (A_1 + A_0).$$

Squaring these amplitudes we find:

$$|A_{Charge}|^2 = \frac{1}{2} \ (|A_1|^2 + |A_0|^2) \left[1 + \frac{2ReA_0{}^*A_1}{|A_0|^2 + |A_1|^2} \right]$$

$$|A_{Neutral}|^2 = \frac{1}{2} \ (|A_1|^2 + |A_0|^2) \left[1 - \frac{2ReA_0{}^*A_1}{|A_0|^2 + |A_1|^2} \right].$$

Hence the difference of the phase space reduced cross sections for the neutral and charged versions of Reactions 1-3 directly measures the isosinglet-isotriplet interference term. A popular production mechanism for charmed mesons in e^+e^- annihilation is (De Rujula 76):
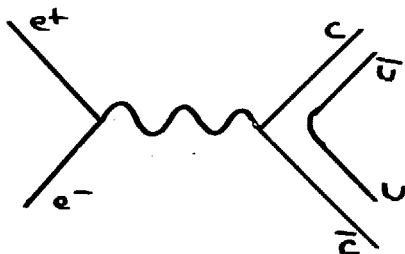
Because the charmed quark is assumed to be an isosinglet, this model will automatically satisfy our isospin production assumption.

Our second assumption is that, neglecting phase space and angular momentum barrier factors, the rate of D^{*+} radiative decay is suppressed relative to D^{*0} radiative decays according to:

$$\frac{\Gamma(D^{*+} \rightarrow \gamma D^{+})}{\Gamma(D^{*0} \rightarrow \gamma D^{0})} = \frac{1}{S} \qquad \text{Eqn. 7}$$

where theoretical estimates of S range from 4 to 25, depending on the magnetic moment of the charmed quark (Ono 76). D^{*} to D radiative decays are assumed to occur via quark spin-flip, due to coupling of the photon and the quark magnetic moment. In the limit of negligible charmed quark magnetic moment, radiative D^{*} decays will occur by a spin flip of the light quark with a rate proportional to the square of the light quark's charge. The radiative width of the D^{*0} meson which contains a $\bar{u}$ quark of charge -2/3 will thus be 4 times larger than the radiative width of the D^{*+} meson which contains a $\bar{d}$ quark of charge +1/3. The fit used for the entries in column 3 of Table 3 assumes S = 4. Most of the entries are stable to changes in S within the quoted errors. We will discuss later the entries which depend on S.

Our assumptions on the relationship between the D^{*+} and D^{*0} radiative widths, when coupled with the assumption that D^{*} pionic decays conserve isospin, allow us to compute the complete set of D^{*+} decay branching ratios in terms of the branching ratio for $D^{*0} \rightarrow D^{0}\gamma(B^{0}_{\gamma})$ from the equations below:

$$\frac{\Gamma(D^{*+} \rightarrow \pi^{+}D^{0})}{\Gamma(D^{*+} \rightarrow \gamma D^{0})} = 2S \left[\frac{1-B^{0}_{\gamma}}{B_{\gamma}}\right] \left[\frac{M_{D^{*0}} - M_{D^{0}}}{M_{D^{*+}} - M_{D^{+}}}\right]^{3} \left[\frac{M_{D^{*+}} - M_{\pi^{+}} - M_{D^{0}}}{M_{D^{*0}} - M_{\pi^{0}} - M_{D^{0}}}\right]^{3/2} \qquad \text{Eqn. 8}$$

$$\frac{\Gamma(D^{*+} \rightarrow \pi^0 D^+)}{\Gamma(D^{*+} \rightarrow \pi^+ D^0)} = \frac{1}{2} \left[\frac{M_{D^{*+}} - M_{\pi^0} - M_{D^+}}{M_{D^{*+}} - M_{\pi^+} - M_{D^0}} \right]^{3/2} \qquad \text{Eqn. 9}$$

The factors of 2 and 1/2 in Eqns. 8 and 9 come from Clebsh-Gordon coefficients. The mass ratios in these expressions are approximations for p^3 phase space angular momentum barrier factors in the same spirit as the approximations of Eqns. 5 and 6. Here the p^3 factor refers to the momentum of the D in the D* rest frame in either pionic or radiative D* decay. If one assumes that parity is conserved in D* decays and that the D and D* have even relative parity, either D* decay mode has its decay products in a P-wave, thus giving a p^3 phase space angular momentum barrier factor.

The foregoing considerations allow us to reduce the number of fitting parameters from the 12 required in the loosely coupled fit to 8 in the tightly coupled fit. This reduction is accomplished as follows. Using the area parameters defined by Table 2 we note that under the assumptions of the tightly coupled fit the parameters FOC, FIC, and F2C are computable from the D meson masses and FON, FIN, and F2N can be written in terms of these and a new parameter α which is a function of the $D^0 \rightarrow K^- \pi^+$ and $D^+ \rightarrow K^- \pi^+ \pi^+$ branching ratios. Specifically, one has the relationships:

$$FOC = \frac{N_{K\pi}}{N_{K\pi\pi}} \alpha \ FON \left[\frac{ECM - 2M_{D^+}}{ECM - 2M_{D^0}} \right]^{3/2}$$

$$FIC = \frac{N_{K\pi}}{N_{K\pi\pi}} \alpha \ FIN \left[\frac{ECM - M_{D^+} - M_{D^{*+}}}{ECM - M_{D^0} - M_{D^{*0}}} \right]^{3/2}$$

$$F2C = \frac{N_{K\pi}}{N_{K\pi\pi}} \alpha \ F2N \left[\frac{ECM - 2M_{D^{*+}}}{ECM - 2M_{D^{*0}}} \right]^{3/2}$$

where

$$\alpha \equiv \frac{\epsilon_{K\pi}}{\epsilon_{K\pi\pi}} \quad \frac{BR(D^{*+} \to K^-\pi^+\pi^+)}{BR(D^0 \to K^-\pi^+)} \quad .$$

In the above expressions, $N_{K\pi}/N_{K\pi\pi}$, the ratio of $D^0 \to K^-\pi^+$ to $D^+ \to K^-\pi^+\pi^+$ signal events, is necessary because F0C, F1C, and F2C are <u>fractions</u> of D^+'s arising from Reactions 1-3 respec⁻ ⁻ly rather than the absolute number. The efficiency ratio $\epsilon_{K\pi\pi}/\epsilon_{K\pi}$ was computed via Monte Carlo simulation to be $\epsilon_{K\pi\pi} = .15$, $\epsilon_{K\pi} = .35$ for the cuts employed in the data. Last, the parameters BGC and FD were computed from α, and the radiative D^{*0} branching ratio were gotten from Eqns. 8 and 9.

In Table 3 we show typical results of the tightly coupled fit. These entries represent a composite of results from tightly coupled fits performed with a variety of starting positions, resolutions, and background parameterizations. Comparison of columns 2 and 3 of the table shows that the tightly coupled and loosely coupled fits are in essential agreement, except for the percentage of D^0's due to D^{*+} decays and the D^{*0} radiative branching ratio. The large amount of D^{*+} feed-down required by the tightly coupled fit is a consequence of the assumed suppression of D^{*+} radiative decays.

We see from the table that both fits attribute 1/3 of the total D^+ production to $D^{*+}D^{*-}$ production. Because the fits chose D^{*+},D^+ values which place the reaction $D^{*+} \to D^+\pi^0$ just at threshold or right below threshold, the substantial observed $D^{*+}D^{*-}$ signal in the D^+ spectrum is presumably due to radiative D^{*+} decays. Because the radiative D^{*+} branching ratio is forced to be small, the amount of $D^{*+}D^{*-}$ production must

be quite large, and much of it will appear in the D^0 spectrum as a feed-down contribution. The tightly coupled fit avoids attributing the entire narrow peak in the D^0 spectrum near 200 MeV/c to feed-down by raising the D^{*0} radiative branching ratio above the value found in the loosely coupled fit. We see from Eqn. 8 that by raising the D^{*0} radiative branching ratio from 0.45 to 0.75 the tightly coupled fit manages to increase the D^{*+} radiative branching ratio from 10.5% to 31%. Lastly we note that in order to accommodate the large $D^{*+}D^{*-}$ feed-down D^0 contribution, the tightly coupled fit forces $M_{D^{*0}}$ to equal $M_{D^{*+}}$, making the feed-down spectral contributions indistinguishable from $D^{*0}\bar{D}^{*0}$; $D^{*0} \rightarrow D^0\pi^0$.

We have previously noted that there is considerable theoretical uncertainty in the expected suppression of D^{*+} radiative decays relative to D^{*0} radiative decays. In order to understand the effects of this uncertainty, we have performed tightly coupled fits at values of $S = 8$ and 16, as well as the value $S = 4$ used in Table 3 (see Eqn. 7). We have found that increasing S from 4 to 16 causes the D^{*0} radiative branching fraction (B_γ^0) to increase from 0.75 to 0.90. All other fitted parameters change by amounts which are negligible compared to their errors. We note that this response keeps the quantity $S[(1-B_\gamma^0)/B_\gamma^0]$ stable to about 25% in spite of the factor of 4 variation in S. From Eqn. 8 we see that the fit is thus changing $(BR(D^{*0} \rightarrow \gamma D^0)$ in order to keep $BR(D^{*+} \rightarrow D^+\pi^0)$ relatively stable. Although the χ^2 of the tightly coupled fit is still acceptable for fits with large values of S, the values for B_γ^0 in excess of 0.75 no longer fit the triangular momentum spectrum of the data due to $D^{*0} \rightarrow \gamma D^0$.

We have seen from the foregoing that it is possible to fit the joint D^0, D^+ momentum spectrum under the two major assumptions of the tightly coupled fit. The tightly coupled fit attributes a rather large fraction of D^0 production at 4.028 GeV to the feed-down reaction $D^{*+} \rightarrow \pi^+ D^0$ in sharp contrast to the more empirical loosely coupled fit. As discussed in Chapter 7 the feed-down reaction contributes substantially to D^0 production above Ecm = 5 GeV so this conclusion of the feed-down fit may be correct. The feed-down fit does, however, force the D^{*0} radiative branching ratio to be uncomfortably high, in contradiction with theoretical estimates (Ono 76) and one's visual impression of the data. The confirmation or rejection of the feed-down fit's assumption will have to await the acquisition of more data.

F.   The Relative Rates of Reactions 1-3

It has been suggested (De Rujula 76a) that, apart from phase space and angular momentum barrier factors. Reactions 1 through 3 should be produced in the ratios 1 : 4 : 7. Such a prediction postulates that D mesons are produced in $e^+ e^-$ annihilation by a diagram in which the virtual time-like photon couples directly to a $c\bar{c}$ pair as in the diagram below:
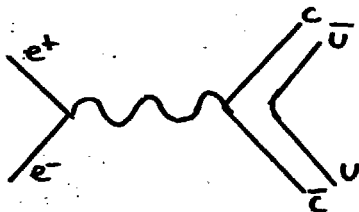
It further suggests that spin correlations between the c and u quark should be negligible in light of the large mass (or low magnetic moment)

of the charmed quark. This later assumption implies that the $D\bar{D}$, $D\bar{D}^*$, and $D^*\bar{D}^*$ photon couplings should be universal, and hence the cross sections should be proportional to the phase space angular momentum barrier factors multiplied by the number of available spin configurations for a given final state. Naively, if one assumes that the D is a pseudoscalar and and the D^* is a vector, one would expect spin counting ratios of 1 : 6 : 9 for Reaction 1-3 respectively. As Close 76 has shown, however, some of these configurations violate parity conservation at the production vertex hence the proper ratio is 1 : 4 : 7.

The data of Table 3 contradict this prediction. Using the table's entries for the D^0 production fractions, and applying a p^3 correction factor computed from the table's D^0 and D^{*0} mass estimates we find that reactions 1-3 are produced in the ratio 0.2 ± 0.1 : 4.0 ± 0.8 : 128 ± 41 rather than 1 : 4 : 7. These errors incorporate uncertainties in p^3 due to uncertainties in the D^{*0} and D^0 mass. Various theoretical explanations for this discrepancy have appeared in the literature ranging from anomalous form factors (Lane 76), to production of axial vector charmed particles (Suzuki 76), to finally $D^* - \bar{D}^*$ molecules (De Rujula 77).

9. SPIN ANALYSIS OF THE NEW MESONS

Although we have insufficient data to determine uniquely the spin-parity assignments of the newly discovered charmed meson candidates, we can discriminate between several low spin possibilities. We denote the neutral low lying candidate with a nominal mass of 1865 MeV/c^2 as the D, with the presumed excited state observed near 2006 MeV/c^2 in the recoil spectrum against the D as the D*. In this section we will discuss the following possible J^P assignments for the D and D*:

D	D*
$0^{\pm}$	$0^{\pm}$
$0^{\pm}$	$1^{\pm}$
$1^{\pm}$	$0^{\pm}$

It is apparent that higher possible assignments will have to wait for the future.

It is, of course, intrinsically interesting to determine the spin and parity of any new state, but there are other reasons for this work as well. One reason is that it is not really theoretically obvious what the low lying charmed meson spin parity assignments should be. In the conventional wisdom, the lowest lying charmed meson is a pseudoscalar, and the first excited state is a vector meson. Such a belief follows from the assumption that the hyperfine quark splitting of charmed mesons should be of the same sign as the hyperfine splitting between the ρ and the π. However we note that the D*-D mass difference is considerably smaller than the mass splitting within an SU(4) multiplet; hence it may

be dangerous to extrapolate to SU(4) results that are known to hold in SU(3). Such a fear has added justification in light of the reduced magnetic moment of the charmed quark due to its larger mass. In static quark theories it is the interaction of the two quark magnetic moments which give rise to the splitting between ground and first excited state quark multiplets. Such considerations have led some theorists to speculate that the lowest lying charmed meson is indeed a vector rather than a pseudoscalar (Brochard 76) (Altarelli 75).

If the lightest charmed states are pseudoscalars, purely leptonic two-body dedays of these mesons will be strongly suppressed by the helicity selection rules responsible for pions decaying leptonically to muons rather than phase-space favored electrons. Because of this suppression, one estimates that purely leptonic D^0 decays should be negligible relative to semileptonic and hadronic decays (Gaillard 75). From the expression (Commins 73) for the decay rate of a pseudoscalar of mass m_D decaying into a lepton of mass m_ℓ and a neutrino:

$$\frac{1}{\tau} = \frac{G^2 f^2}{8\pi} \; m_\ell^2 m_D \left[1 - \frac{m_\ell^2}{m_D^2} \right]^2$$

we see that

$$\frac{\Gamma(D^+ \to \mu^+ \nu)}{\Gamma(D^+ \to e^+ \nu)} \approx \left[\frac{m_\mu}{m_e} \right]^2 \approx 4 \times 10^4.$$

Hence purely leptonic D^+, $\hat{D}^-$ decays could not be a significant source of the SPEAR e-μ events (Perl 76) because these decays would strongly favor $\mu^+ \mu^-$ production rather than eμ production.

Considerable spin parity information on the charmed mesons comes

almost for free. The likely D^* to D cascade mechanisms are $D^* \to \pi D$ or $D^* \to \gamma D$. Strong evidence exists for both as shown in Chapter 8 and the existence of either implies that the D and D^* cannot both be spinless. $D^* \to D\gamma$ violates angular momentum conservation along the photon axis if both mesons are spinless. The presence of the decay $D^* \to \pi^0 D$ implies that the D and D^* have odd relative parity if both are spinless, but then they could not couple to a photon in a P-wave without violating parity conservation in the electromagnetic production process. As shown in Chapter 8 $e^+ e^- \to \bar{D}^* D^0$ is the dominant production mode for charmed mesons near threshold, however.

Observation of the pionic cascade implies that the D and D^* must have even relative parity if one meson has zero spin and the other has spin 1, as in our two remaining possibilities considered here. This observation is quite helpful because it allows for unique predictions of production and decay distributions for the reaction $e^+ e^- \to D\bar{D}^*$, $D \to K\pi$ owing to the elimination of one of the two independent production helicity amplitudes. We turn next to a brief discussion of the expected joint production and decay distributions for the remaining cases. Our conclusions can be easily reached through an application of the Jacob-Wick helicity formalism, but we shall employ arguments based on the form required for amplitudes by rotational and gauge invariance. We feel comfortable in using non-relativistic approximations in deriving these results because of the low D^* velocity ($\beta \approx .3$) present in $D\bar{D}^*$ production at $E_{cm} = 4.028$ GeV.

Defining vectors as in Figure 1 we can write the production amplitude for $e^+ e^- \to D\bar{D}^*$ as proportional to $\vec{S} \cdot \vec{\varepsilon} \times \vec{P}$, where $\vec{S}$ refers to the spin of either the D or D^* and $\vec{\varepsilon}$ refers to the transverse polarization
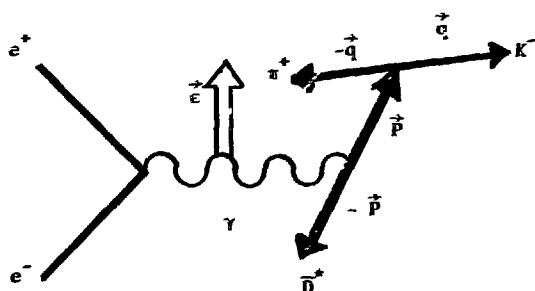
$$e^+ e^- \rightarrow \vec{D}^* D^0 \; ; \; D^0 \rightarrow K^- \pi^+$$

Fig. 1

Definition of vectors used in text. $\vec{P}$ is the center-of-mass vector of the D^0 , $\vec{\epsilon}$ is the transverse virtual photon polarization vector, and $\vec{q}$ is the K^- momentum in the D^0 rest frame.

vector of the virtual photon. (See Appendix 2.) The assumed trans-
versality of the virtual photon follows from quantum electrodynamic
arguments applied at the $e^+e^-\gamma$ vertex in the limit $E_{cm} \gg m_e$ (m_e is the mass
of the electron). (See Cabibbo 61 and Schwitters 75.) A spinless D will
of course decay isotropically in its own rest frame, whereas a spin 1 D
will decay with an amplitude proportional to $(\vec{S} \cdot \vec{q})$. (See Appendix 2.)
Hence the joint production and decay amplitudes for our two remaining spin
parity possibilities are:

$$\text{Amp} \propto \vec{S} \cdot \vec{\epsilon} \times \vec{P} \times \left\{ \begin{array}{ccc} & J^P(D) & J^P(D^*) \\ 1 & 0^{\mp} & 1^{\mp} \\ \vec{S} \cdot \vec{q} & 1^{\mp} & 0^{\mp} \end{array} \right.$$

Squaring and summing over the polarization of the spin 1 particle we obtain:

$$|\text{Amp}|^2 \propto \left\{ \begin{array}{c} |\vec{\epsilon} \times \vec{P}|^2 \\ |\vec{P} \cdot \vec{\epsilon} \times \vec{q}|^2. \end{array} \right.$$

Summing over the virtual γ polarization (assuming unpolarized beams) we
obtain:

$$|\text{Amp}|^2 \propto \left\{ \begin{array}{c} 1 + |\vec{P} \cdot z|^2 \\ 1 - |\vec{P} \cdot \vec{q}|^2 - |\vec{z} \cdot \vec{P} \times \vec{q}|^2. \end{array} \right.$$

This summation will be reviewed in Appendix 2. The z unit vector points
along the annihilation axis.

It is convenient to express these distributions in terms of the lab
production and helicity frame decay angles. We orientate the helicity
frame with the z' axis along the D^0 momentum vector and the y' axis along

the reaction plane normal ($\hat{y}' \parallel \hat{z} \times \vec{P}$). We obtain:

$$\frac{d\sigma}{d\Omega d\Omega'} \propto \begin{cases} 1 + \cos^2\theta & (1) \\[2mm] \sin^2\theta(\cos^2\phi + \cos^2\theta \, \sin^2\phi) & (2) \end{cases}$$

where Θ refers to the polar production angle with respect to the annihilation axis and θ,ϕ are the K momentum spherical angles in the D helicity frame. The discrimination between these two expressions comes from the expected anistropy in the $D \to K\pi$ decay under the spin 1 D hypothesis. By cutting on D missing mass, a fairly clean sample of the reaction $e^+ e^- \to D\bar{D}^*$ can be obtained and a search for such anisotropies can be performed. Unfortunately two problems arise which complicate the procedure of comparing equations 1 and 2 to the data.

The first difficulty is the acceptance problem inevitable with a 2.6 π cylindrical detector with essentially no efficiency for detecting prongs within a cone of half-angle 49.5° on either end of the annihilation axis. The kinematics of D production near threshold can be characterized as a slowly moving D in the detector frame exploding into 2 fast prongs of 861 MeV/c momentum. Because of the low momentum of the D in the detector frame, one expects reasonably large acceptance for picking up the D decay products over the full range of $\cos\theta$ and $\cos\Theta$. One expects, however, considerable variation in the ϕ (in the helicity frame) acceptance with minima at 0° and 180° and maxima at 90° and 270°. In addition the geometrical acceptances in all three variables are coupled together. For example, acceptance is nearly ϕ independent for $\cos\theta$ near 1, but has zeros at $\sin\phi = 0$ when $\cos\theta = 0$. For this reason we shall always compare the experimental angular
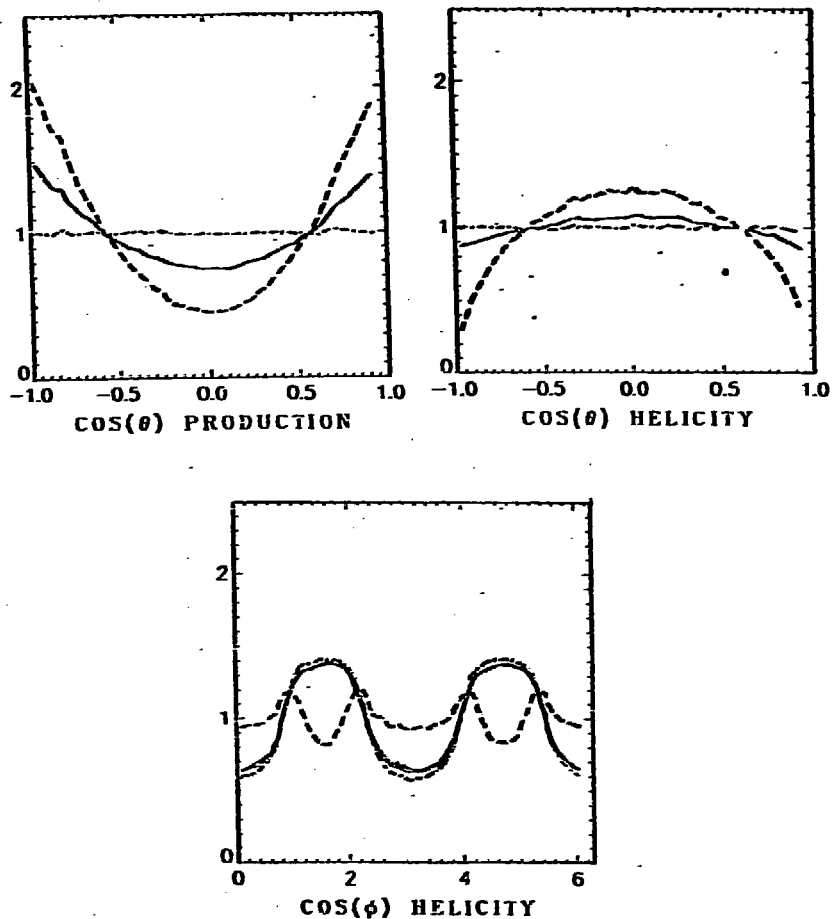
Fig. 2

Expected angular distributions for events generated according
to Eqn 1 (solid curve) , Eqn 2 (dashed curve), and isotropic decay
(dashed and dotted curve). This curves are the result of
of an integration of the angular distributions multiplied
by a simple efficiency factor which is explained in text.

distributions to distributions obtained by Monte Carlo simulations with the 2 sets of theoretical matrix elements.

In order to gauge the effects of pure geometrical efficiency in θ, θ, ϕ, we have performed integrations of the distributions of eqn. 1 and 2 multiplied by a simple, purely geometrical efficiency factor appropriate for D^0's produced near rest in the laboratory. For D^0's produced near rest, the K, π decay products are nearly anti-collinear in the detector frame, and the D will be detected if the polar angle of either the K or π momentum satisfies $|\cos\theta_{K,\pi}| < .65$. In the set of variables θ and (θ, ϕ) this polar angle is given by $|\cos\theta_{K,\pi}| = Q = |\cos\theta\cos\theta - \cos\phi\sin\theta\sin\theta|$. Hence our idealized efficiency is given by:

$$E(\theta, \theta, \phi) = \begin{cases} 0 & \text{if } Q > .65 \\ 1 & \text{of } Q < .65 \end{cases}$$

In Figure 2 we present the angular distributions obtained for eqn. (1) (solid curve), eqn. (2) (dashed curve), and a flat distribution in θ, θ, ϕ (dashed and dotted curve). The curves for a given angular variable are obtained by Monte Carlo integration over the remaining angular variables. All curves in a given plot are normalized to the same area. Fluctuations in the curves are due to statistical errors in the integration.

The coupling between the production and decay angular distributions is evident in Figure 2. Integration of eqn. (2) over the (θ, ϕ) decay variables (neglecting efficiency factors) shows that it has the same $1 + \cos^2\theta$ polar production distribution as eqn. (1). When efficiency factors are included, however, the distribution appears to be more like $1 + 3.7 \cos^2\theta$. Similarly eqn. (1) represents an isotropic D^0 decay

distribution; yet, when corrected for efficiency, one obtains a slightly parabolic distribution with a maximum at $\cos\theta = 1$. Because of the complexities of the θ, θ, ϕ coupling illustrated by the preceding, we shall always compare experimental θ, and θ distributions to Monte Carlo simulations which naturally incorporate these purely geometrical effects as well as more subtle effects such as kaon decay corrections and triggering biases.

Our second problem is concerned with the effects of secondary D^0's from from D^{*0} and D^{*+} decays. The presence of D^0's from D^* cascades dilutes the discrimination power between our two spin-parity hypotheses since the expected anisotropy in the decay of D^0 under the spin 1 assumption is destroyed if the given D^0 arises from a spinless D^* intermediate state. Secondary D^0's are from the three D^* cascade processes: $D^{*0} \rightarrow \pi^0 D^0$, $D^{*0} \rightarrow \gamma D^0$, and $D^{*+} \rightarrow \pi^+ D^0$, where D^*'s are produced via $e^+ e^- \rightarrow D\bar{D}^*$. Under either of our two spin-parity hypotheses, secondary D^0's will follow a joint production and decay distributions approximated by eqn. (1). Secondary D^0's from pion cascades will have polar angles within 5° of the polar angle of the D^0-D^* axis owing to the small Q value for the reaction $D^* \rightarrow \pi^0 D^0$. (From the recoil fits of Chapter 8 we find Q < 8 MeV for both charged and neutral D^* pionic cascades.) D^0's from D^{*0} radiative cascades follow a more isotropic polar distribution than eqn. (1) owing to the larger momentum of the D^0 in the D^* rest frame. Because of this larger relative momentum, however, D^0's from radiative D^* decays tend to have wide momentum distributions and thus are a minor source of contamination for a narrow recoil cut. It is clear from the preceding that one's ability to discriminate between the two spin-parity hypotheses depends critically

on the recoil of cut chosen to isolate primary D^0's in the reaction $e^+e^- \to D^0 D^{*0}$. Unfortunately we cannot resolve these D^0's from the secondary D^0's, so we must estimate the fraction of primaries within a given recoil cut from a fit to the recoil spectrum shape.

Throughout this analysis we use D^0's found within 35,000 multi-hadronic events collected at center-of-mass energies between 3.90 and 4.15 GeV. This spread of energies was used in order to include some of the "old" (pre-charm discovery) data collected while scanning the region near Ecm = 4.028 GeV. In order to combine data over a range of energies we employ a cut on D^0 recoil mass (M_{rec}) (computed with a fixed D^0 mass of 1865 MeV/c^2); $1970 < M_{rec} < 2030$ MeV/c^2. Because our previous analysis of the recoil system was in terms of the momentum distribution of D^0's at fixed energy (see Chapter 8), we note that this cut corresponds to a momentum region of $513 < P_{D^0} < 616$ MeV/c for data collected at a fixed energy of 4.028 GeV.

We estimate that (64 ± 4)% of D^0's satisfying this cut are primary D^0's. We shall try to justify this fraction and quoted error obtained from the results of the fit of Chapter 8 by demonstrating the fraction's sensitivity to the recoil fit parameters. The largest uncertainty in the primary fraction comes from the fraction of D^0's from the process $D^{*+} \to \pi^+ D^0$ which we shall call the feed-down process. In Figure 3 we show the various contributions to the D^0 momentum spectrum near 500 MeV/c for three different feed-down percentages. Here we define feed-down percentage as the fraction of events beneath the solid curve attributed to feed-down. Recoil fits, described in Chapter 8 attribute from 5% to 20% of events in the vicinity of 500 MeV/c to feed-down. The two heavy
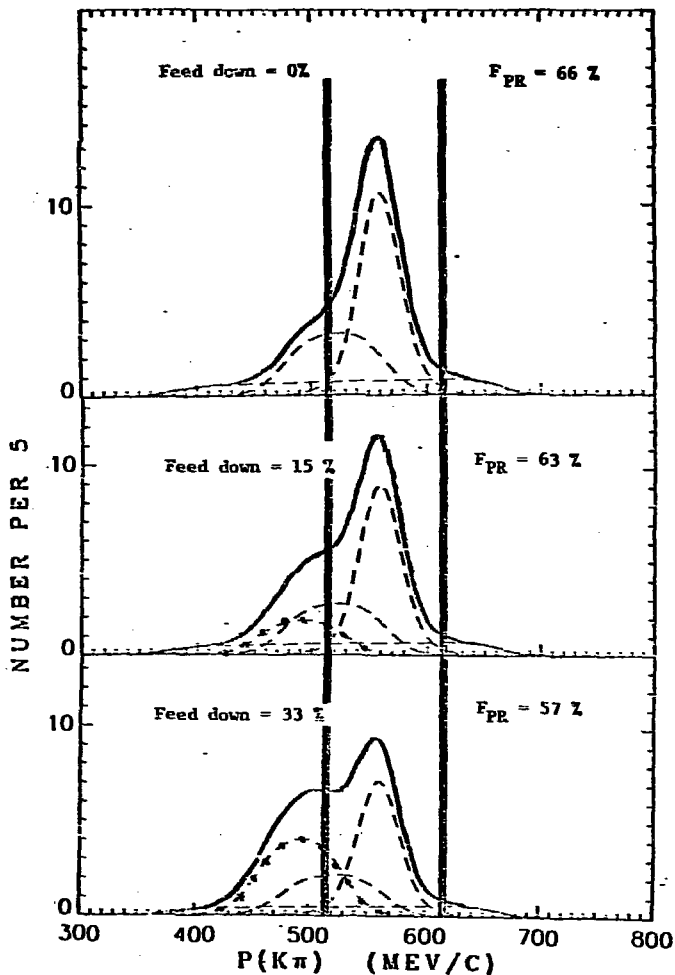
Fig. 3

Calculation of the primary fraction (F_{PR}) for three different feed down percentages. The two parallel vertical lines show the position of the recoil cut. The dotted line gives the feed down momentum spectrum. The dashed curves show the various purely neutral D^0 contributions.

vertical lines show the position of the recoil cut. The dashed curves represent D^0 production via $e^+e^- \rightarrow \bar{D}^*D^0$. (The most prominent dashed peak shows direct D^0 production, the broad ramp is from D^{*0} radiative cascade, and the smaller peak to the left of the direct peak is from D^{*0} pionic cascade.) The dotted curve shows the feed-down contribution. The fraction of primary D^0's within the recoil cut (F_{PR}) is shown to range from 66% to 57% as the feed-down is increased from 0 to 33%. This fraction is determined by a direct integration over the function illustrated in Fig. 3. The positions and shapes of the individual spectral contributions depend on the D^0, D^+, D^{*0}, and D^{*+} masses and the D^0 momentum resolution (estimated to be $\sigma = 20$ MeV/c from Monte Carlo simulation). Calculation of the spectral shape is discussed in Chapter 8.

We have computed these fractions using masses of 1865, 2006, 1875, and 2010 MeV/c^2 for the D^0, D^{*0}, D^+, and D^{*+}, respectively, and note that F_{PR} is stable to within 2% as these masses are varied within the extreme limits allowed by the fits. The relative area underneath the peaks due to D^{*0} cascade is determined by the D^{*0} radiative branching fraction $Br_\gamma = [\Gamma(D^{*0} \rightarrow \gamma D^0)]/[\Gamma(D^{*0} \rightarrow \gamma D^0) + \Gamma(D^{*0} \rightarrow \pi^0 D^0)]$. The values Br_γ allowed by the fit of Chapter 9 range from 45% to 75%. In Figure 3 we use the lower limit of 45% and note that varying Br_γ from 45 to 75% increases F_{PR} by 3%.

We see from the foregoing that the primary D^0 fraction depends on numerous factors but is acutely sensitive to only one, the percentage of feed-down. Our primary fraction estimate $F_{PR} = (64 \pm 4)\%$ was deduced from a composite of recoil fits described in Chapter 9. Although the

feed-down percentage is poorly determined by these fits, recoil fits preferring large amounts of feed-down tend to prefer a large Br_γ, which tends to compensate in the calculation of F_{PR} and allows for a relatively small F_{PR} error.

With all that out of the way, we present the data consisting of 153 $D^0 \rightarrow K\pi$ candidates produced with center-of-mass energy between 3.9 and 4.6 GeV and satisfying the recoil cut $1970 < M_{Rec} < 2030$ MeV/c^2. For this analysis we eschew the particle identification by time-of-flight technique described in Chapter 3. All neutral two-prong combinations are considered as potential D^0 candidates with the track having time-of-flight most consistent with the kaon hypothesis called the kaon. The other track is taken to be the pion. For ~40% of the real D^0's this amounts to little more than a random selection. For the production angular distribution this K-π ambiguity is irrelevant; however it could matter in analyzing the decay distribution of the kaon in the D^0 helicity frame. Fortunately it does not, since, for slow D^0's, K-π interchange effectively reverses the direction of the kaon in the D^0 helicity frame, and the angular distributions we are testing are invariant under this transformation.

Figures 4b and 4a show the observed $\cos\theta$ and $\cos\theta$ distributions for D^0 candidates satisfying the recoil cuts and the cut on invariant mass from 1820 to 1920 MeV/c^2. Superimposed on these distributions are suitably normalized distributions for our two spin-parity hypotheses. Both curves are computed from a Monte Carlo program incorporating the effects of efficiency, resolution, and D^0 secondaries, as well as a 15%
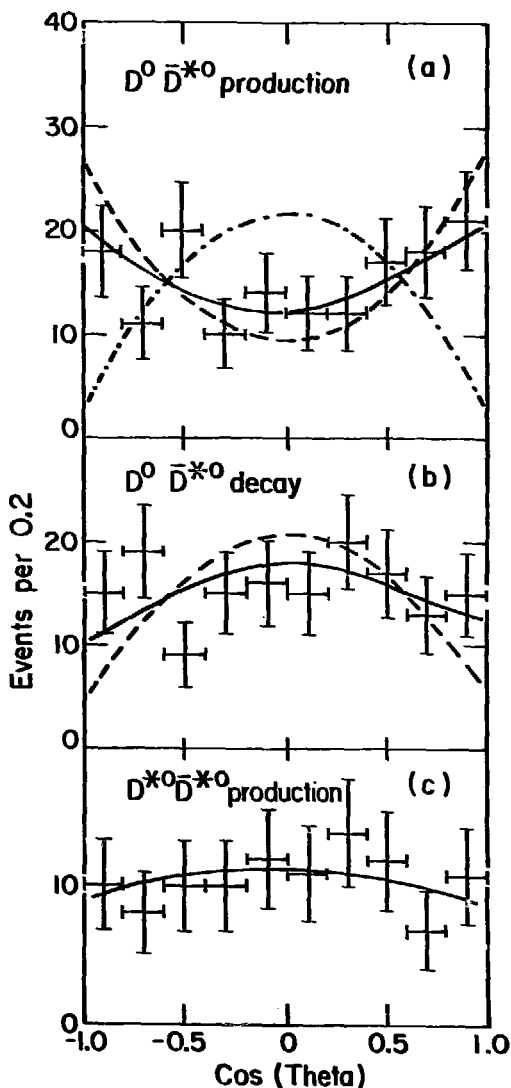
Fig. 4

Comparison of the data to the various
model distributions for the three spin
assignments $S(D^0) = 0, S(D^{*0}) = 1$ (solid
curve) ; $S(D^0) = 1$, $S(D^{*0}) = 0$ (dashed curve);
and $S(D^0) = 0$, $S(D^{*0}) = 0$ (dashed and
dotted curve) .

background of uncorrelated (i.e. non-D^0) neutral 2-prong combinations. The 15% background is estimated from the Kπ invariant mass plot (see Fig. 5). We have used isotropic backgrounds in both production and decay and have checked this assumption with background events from sidebands in the Kπ invariant mass plot. In both portions of Figure 4 the solid curve is computed from eqn. (1) and the dashed curve is computed from eqn. (2). In Figure 4a we have included a dashed and dotted curve showing a $\sin^2\theta$ distribution appropriate for the case of spinless D^0's and D^{*0}'s, corrected for acceptance, background, and the presence of secondaries. The χ^2 for these various curves are summarized below:

$$\chi^2/\text{Degree of Freedom}$$

S_D	S_{D^*}	Production	Decay
0	1	5.6/9 (76%)	8.2/9 (51%)
1	0	11.0/9 (28%)	23/9 (0.6%)
0	0	74.0/9	

Confidence levels are in ( ).

These χ^2 and confidence levels do not reflect uncertainty in the model distributions (due to uncertainty in F_{PR} for example).

Clearly the conventional hypothesis of spin 0 D^0 - spin 1 D^{*0} is favored. One is tempted to combine the production and decay χ^2 in order to maximize the statistical discrimination between the two serious hypotheses. However, caution must be applied owing to the correlation between the production and decay angular distributions created by the geometrical acceptance. It would also be desirable to use ϕ information
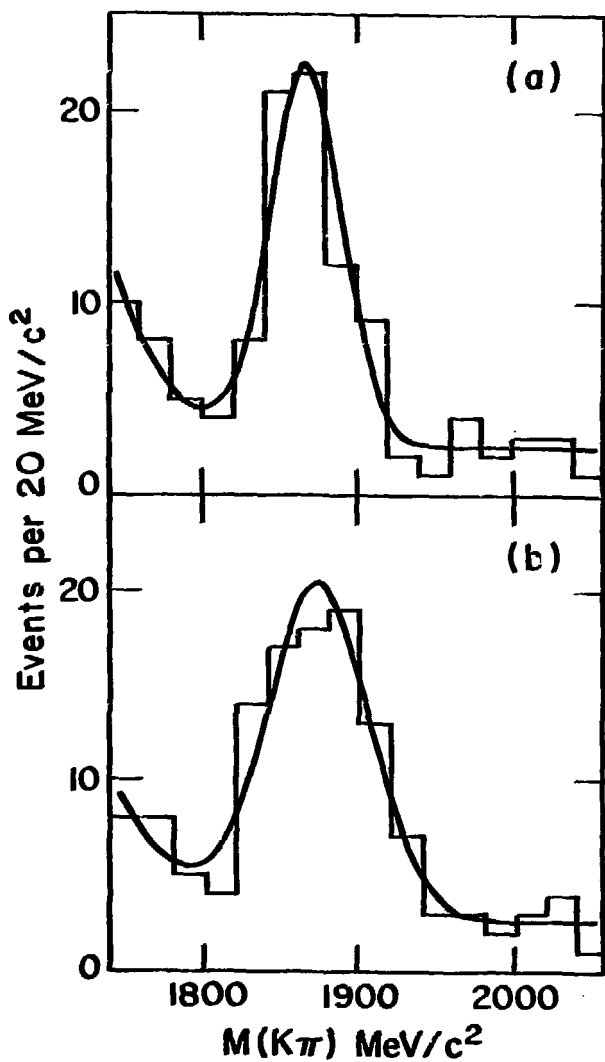
Fig. 5

The Kπ invariant mass distribution for
events in the angular region given by
$I_5 < 0.32$ (Fig. a) and $I_5 > 0.32$ (Fig. b).

to discriminate between eqns. (1) and (2). This information is less useful than one might initially assume, due to the strong efficiency variation in ϕ. Lastly it is important to include uncertainties in background estimation and primary fraction when evaluating the statistical discrimination between our two spin-parity hypotheses. For these reasons, we have devised an alternative statistical test modeled after the technique used to establish parity violation in Chapter 5.

The technique displays the invariant mass plot for events satisfying the recoil mass cut and having variables within one of two angular regions chosen to insure discrimination between eqns. (1) and (2) by dividing the space of angular variables by a surface of constant $I_3 = \sin^2\theta(\cos^2\phi+\cos^2\theta\sin^2\phi)$. Figures 5a and 5b show the $K^{\mp}\pi^{\pm}$ invariant mass distributions for events satisfying $I_3 < 0.32$ and $I_3 > 0.32$ respectively. The fit of Figs. 5a and 5b, consisting of a Gaussian signal over an exponentially falling background, gives 58 ± 8 and 73 ± 10 signal events respectively. Defining an asymmetry variable A_s equal to the difference in the number of signal events over their sum, we obtain $A_s = 0.11\pm0.10$, which is in good agreement with the value of 0.11 ± 0.01 expected for spin 0 D's and spin 1 D*'s and inconsistent with 0.41 ± 0.03, the value obtained for spin 1 D's and spin 0 D*'s ($\chi^2 \approx 8.3$, CL = 3.5×10^{-3}). The errors on the expected asymmetries under the two hypotheses reflect the errors on the fraction of primary D^0's.

Corroborating evidence for this spin hypothesis can be obtained from a study of the D^{*0} polar distribution for the reaction $e^+e^- \rightarrow D^{*0}\bar{D}^{*0}$.

The D^* polar distribution for this reaction is of the form

$$(d\sigma)/(d\cos\theta^*) \propto 1 + \alpha \cos^2\theta^* \tag{3}$$

where unique predictions for α cannot be made by symmetry arguments except for spin 0 where $\alpha \simeq -1$. Because D^* decays involve either neutrals, as in the cases $D^{*0} \to \pi^0 D^0$, $D^{*0} \to \gamma D^0$, or very low momentum ($p < 60$ MeV/c) pions, as in $D^{*+} \to \pi^+ D^0$, one must infer the D^* polar distribution from the polar distribution of the observed D^0.

In Figure 4c we present the production polar distribution for D^0's from the reaction $e^+ e^- \to D^* \bar{D}^*$ chosen by selecting D^0 invariant masses from 2139 to 2156 MeV/c^2 (at a fixed Ecm of 4.028 GeV this corresponds to a momentum region from 120 to 220 MeV/c). From the fit of Chapter 8 we estimate that 15% of D^0's satisfying this selection are background, with 75% of the legitimate D^0's arising from D^* pionic cascades and 25% arising from radiative D^* decay.

A fraction of the D^0's which we attribute to D^* pionic cascade are presumably due to the feed-down process $e^+ e^- \to D^{*+} D^{*-}$, $D^{*+} \to \pi^+ D^0$. As in the case of $e^+ e^- \to D \bar{D}^*$, the feed-down fraction is highly uncertain. If, however, we assume that the D^{*+} and D^{*0} are members of the same isomultiplet, the feed-down fraction is irrelevant because $e^+ e^- \to D^{*+} D^{*-}$ has the same angular distribution as $e^+ e^- \to D^{*0} \bar{D}^{*0}$.

The D^0 polar production distribution from D^* pionic cascades closely follows eqn. (3) owing to the low D^*, D^0 relative momentum. The 15% background D^0 contribution is consistent with an isotropic $\cos\theta$ distribution as determined from a D^0 background sample taken from sidebands in the $K\pi$ invariant mass plot. The D^0 contribution from D^{*0} radiative decays will be a broad convolution over eqn. (3) owing to the larger D, D^* relative momentum.

In computing this convoluted version of eqn. (3) we assume that the D^* momentum lies <u>uniformly</u> on a cone of half angle δ which depends on the

momentum of the observed $D^0 (P_D)$ via the expression:

$$\cos\delta = \frac{1}{2P_{D^*}P_D} \left\{ 2E_{D^*}E_D - M_{D^*}^2 - M_D^2 \right\}$$

where M_{D^*}, M_D are the masses of the D^* and D^0 and:

$$E_{D^*} = \frac{1}{2} Ecm; \quad E_D = \sqrt{P_D^2 + M_D^2}; \quad P_{D^*} = \sqrt{E_{D^*}^2 - M_{D^*}^2}.$$

Under these assumptions, the D^* polar angle (θ^*) and the D^0 polar angle (θ) are related via the expression:

$$F(\cos\theta, \phi, P_D) \equiv \cos\theta^* = \cos\delta \cos\theta - \sin\theta \sin\delta \cos\phi$$

where ϕ ranges uniformly from 0 to 2π and gives the orientation of the D^* momentum on the surface of the cone around the D momentum. For a given value of α in eqn. (3), the D^0 $\cos\theta$ distribution $(dn/d\cos\theta)$, can then be computed from the D^0 momentum spectrum contribution for the process $D^{*0} \to \gamma D^0 (dn/dP_D)$ via:

$$\frac{dn}{d\cos\theta} = \frac{1}{4\pi} \left(\frac{3}{3+\alpha} \right) \int_{120 \text{ MeV/c}}^{220 \text{ MeV/c}} dP_D \frac{dn}{dP_D} \int_0^{2\pi} d\phi \left\{ 1 + \alpha F^2(\cos\theta, \phi, P_D) \right\}. \quad (4)$$

In the limit of perfect D^0 momentum resolution and isotropic $D^* \to \gamma D^0$ decay: $(dN)/(dP_D) \propto P_D$. For the purposes of this fit we use this form analytically convoluted with a Gaussian resolution function as obtained in Chapter 8. In Figure 6 we compare a linear combination of eqns. (3) and (4) to a full Monte Carlo simulation predicated on no background, Br_γ = 50%, and α = -1. The relative amounts of eqns. (3) and (4) are fixed by the known Br_γ, leaving no free parameters. The full Monte Carlo includes the effects of resolution and efficiency.
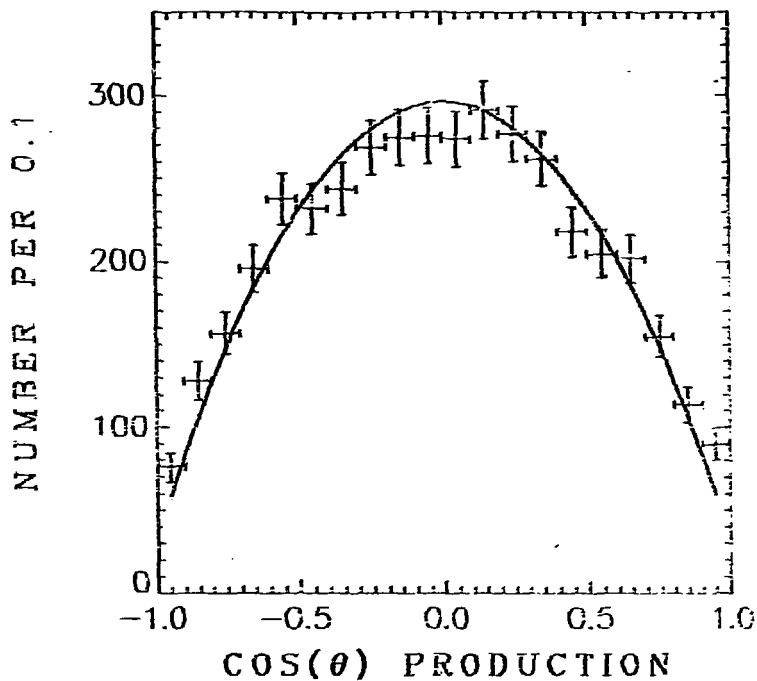
Fig. 6

Comparison of the semi-analytic distribution computed
with Eqn 4 to a complete Monte Carlo calculation
of the process $e^+ e^- \rightarrow D^* \bar{D}^*$. Both distributions
are computed assuming $\alpha = -1$.

We estimate that $\alpha = -0.30 \pm 0.33$ by fitting the data of Fig. 4c to a linear combination of eqn. (3) for pionic decays, eqn. (4) for radiative decays, and an isotropic background. The curve superimposed on Fig. 4c represents the above fit. This result is 2.1 standard deviations from the value expected for spinless D^*'s. It is, however, in agreement with $\alpha = -.20$. The values are computed assuming the virtual γ couples directly to the charge of the charmed quark (Suzuki 76) (Cabibbo 61).

In summary, we have shown that the production and decay angular distributions for D^0's produced near threshold via the reaction $e^+e^- \rightarrow D^0\bar{D}^{*0} + \bar{D}^0 D^{*0}$ are incompatible with D^0, D^* spin-parity assignments of $1^{\mp}$, $0^{\mp}$ and compatible with $0^{\mp}$, $1^{\mp}$. In addition the angular distribution of D^{*0}'s produced in reaction $e^+e^- \rightarrow D^{*0}\bar{D}^{*0}$ is incompatible with a spinless D^* on the 2 standard deviation level. These two results show consistency with the conventional spin-parity assignments 0^- and 1^- for low-lying charmed mesons, and argue strongly against the alternative assignment where the D^{*0} is a pseudoscalar and the D^0 is a vector meson.

10. SUMMARY AND CONCLUSIONS

In this thesis we have presented compelling evidence for the existence of the (D^0, D^+) isodoublet of charmed mesons. Both mesons were initially observed in electron - positron annihilation at center of mass energies near 4.1 GeV. The established decay modes for the D^0 are $K^-\pi^+$, $K_s\pi^+\pi^-$, and $K^-\pi^+\pi^+\pi^-$. To date , the only established D^+ decay mode is $K^-\pi^+\pi^+$. The masses of the D^0 and D^+ are 1863 $\pm$ 3 MeV/c^2 and 1874 $\pm$ 5 MeV/c^2 respectively. Both mesons appear consistent with having zero natural width.

The new mesons were discovered at center-of- mass energies associated with considerable and complicated structure in the total hadronic cross section. This energy domain can be characterized as the region directly after the onset of narrow resonances (the Ψ and Ψ') in $e^+ e^-$ annihilation and right before the onset of broad resonances such as the Ψ'' (4415) . A popular interpretation of the psion family of resonances is that they are $c \bar{c}$ bound states which, because of the operation of the phenomenological OZI rule, prefer to decay into final states containing charmed mesons. Under this interpretation, psions with masses below 3726 MeV/c^2 (the D pair threshold) could only decay into OZI suppressed final states, and would thus be narrow ; while more massive psions could decay into final states containing a $D \bar{D}$ pair and would thus be broad. The discovery of narrow, new mesons in the transition region between the narrow and broad psions certainly lends credence to the $c \bar{c}$ bound state interpretation of the psi family. Measurements (Piccolo 77) of the inclusive D^0 and D^+ production cross sections at Ecm = 4.028

and 4.415 GeV for the three observed D^O decay modes indicate, however, that the observed D production cross section is small. They find that the observed D^O production cross section at 4.028 and 4.415 GeV is 2.5 ± 0.4 nb and 2.1 ± 0.6 nb respectively. Hence if one attributes the total excess cross section observed in $e^+ e^-$ annihilation at these energies to D production, the observed D cross section must be only about 10% of the produced D cross section. This suggests that D's often decay into final states containing at least one neutral particle.

We have presented evidence that the new mesons possess a new quantum number which is conserved in strong and electromagnetic interactions. The new mesons were first discovered at energies exceeding twice their mass, thus suggesting that they must be pair produced. No evidence for the new mesons appears in the copious data collected while investigating the Ψ and Ψ' . Our analysis of the recoil spectrum against the new mesons shows directly that the new particles are always produced in association with systems of greater or equal mass. Finally, in Chapter 5, we presented evidence for parity non-conservation in the decays of the new mesons based on a study of the $D^+ \to K^- \pi^+ \pi^+$ Dalitz plot. This result implies that the new mesons decay weakly and must carry a new quantum number which forbids their strong or electromagnetic decay.

We see from the decay modes of the new mesons that this new quantum number is most likeley charm -- as originally formulated by Glashow, Illiopoulous and Miaimi (Glashow 71). The structure of the weak current in their theory imples the selection rule $\Delta C = \Delta S$ for Cabibbo enhanced non - leptonic decays. This selection rule when applied to the decays of

the D^0 or D^+ means these mesons will preferentially decay into final states containing a single kaon. This law is satisfied by all of the known D^+ and D^0 decay modes. The application of this rule to the decay of the D^+ is particularly striking. The $\Delta C = \Delta S$ selection rule states that a state of positive charm and charge will decay into a final state of negative strangeness and positive charge. Such final states are known as exotic final states since they cannot be due to the decay of a meson constructed from a quark - antiquark combination of the conventional three quarks. No compelling evidence for resonances decaying strongly into exotic final states have yet been established, hence the observation of a state decaying into $K^- \pi^+ \pi^+$ is rather surprising except in the context of a weakly decaying charmed object where it is natural. Upper limits have been established for the $\Delta C \neq \Delta S$ decays of the new mesons such as $\pi^+ \pi^-$, $K^- \pi^- \pi^+$ etc., which are in accordance with the expected Cabibbo supression factor (Piccolo 77).

Other than discovering the F^+ (the charmed isosinglet state) or observing the Cabibbo suppressed decay $D^0 \to \pi^+ \pi^-$ and using it to measure Cabibbo's angle, there is little more that could be done to convince the skeptic that charmed mesons have indeed been produced in $e^+ e^-$ annihilation. We thus adopt the viewpoint espoused by De Rujula, " Either charm has been found, or these mesons are the world's greatest imposters ! " (De Rujula 76 b)

An analysis of the recoil spectrum against the new mesons produced at Ecm = 4.028 GeV has revealed the existence of a higher massed pair of charmed mesons, the D^{*0} (2006) and the D^{*+} (2008). These heavier states can be naturally accomodated in a charmed meson spectroscopy as a ^3S

combination of $c \bar{u}$ or $c \bar{d}$. The lighter charmed mesons would then be ^1S $c \bar{u}$ or $c \bar{d}$ quark combinations. This spectroscopic assignment implies that the D is a pseudoscalar and the more massive D^* is a vector. This is a natural spin assignment in light of experience with the old mesons (i.e. the pseudoscalar π, and K are lighter tha their respective vector particles, the ρ and K^*), and is borne out experimentally as discussed in Chapter 9. One of the heavier states, the D^{*+} (2008) has been directly observed via the sequence $D^{*+} \to \pi^+ D^0$, $D^0 \to K^- \pi^+$. This observation has resulted in a very accurate determination of the D^{*+}, D^0 mass difference ($M_D^{*+} - M_D^0 = 145.3 \pm .5$ MeV/c^2), and a very restrictive limit on the D^{*+} width ($\Gamma < 2.4$ MeV/c^2, at the 90% C.L.).

Because charm is conserved in the strong and electromagnetic interaction, $D^{*'}s$ must nearly always decay into final states containing a D. The closeness of the D and D^* mass limits these decays to the two types $D^* \to \gamma D$ and $D^* \to \pi D$. For the D^{*0}, the decay $D^{*0} \to \pi^- D^+$ is kinematically forbidden, and the decays $D^{*0} \to \gamma D^0$ and $D^{*0} \to \pi^0 D^0$ occur comparably. Our analysis of the D^0 momentum spectrum indicates:

$$\frac{\Gamma (D^{*0} \to \gamma D^0)}{\Gamma (D^{*0} \to \pi^0 D^0)} = 1.2 \pm 0.1$$

The only clearly established D^{*+} decay mode is $D^{*+} \to \pi^+ D^0$. The decay $D^{*+} \to \gamma D^+$ certainly exists, but it is expected on theoretical grounds (Ono 77) to occur at a considerably smaller rate than $D^{*0} \to \gamma D^0$. Because of the uncertainty of the D^+ mass ($M_{D^+} = 1874 \pm 5$ MeV/c^2) we cannot say whether or not the reaction $D^{*+} \to \pi^0 D^+$ is

kinematically allowed. There is some evidence for this mode in the D^+ momentum spectrum at Ecm = 4.028 GeV , but it is statistically insignificant. Using a rather technical set of assumptions concerning the isospin character of the charm production vertex and the relation between the D^{*+} and D^{*o} radiative decay widths, we estimated Br ($D^{*+} + \pi + D^o$) = .60 $\pm$ .15 . These assumptions are discussed in Chapter 8.

In Chapter 8 , we presented evidence that at Ecm = 4.028 GeV, D's are nearly always produced via the charged and neutral versons of the reactions :

$$e^+ e^- \rightarrow D \bar{D} \qquad (1)$$
$$\bar{D}^* D + \bar{D} D^* \qquad (2)$$
$$D^* \bar{D}^* \qquad (3)$$

The relative rates for the neutral version of reactions 1 , 2, and 3 is 1.0 $\pm$ .60 , 7.6 $\pm$ 1.6 , and 8.0 $\pm$ 2.0 respectively. These rates indicate considerably more D^* production than one would naively expect on the basis of phase space and spin counting arguments (De Rujula 76a). Perhaps this observation bears on the nature of the rather narrow cross section enhancement at 4.028 GeV.

Finally, we have obtained upper limits on D^o - $\bar{D}^o$ mixing. In Chapter 7, we presented evidence that less than 13 % of D^o's mix into $\bar{D}^o$'s within the D^o lifetime (90% C.L.) . Current theories (Weinberg 77) indicate that the first order charm changing neutral currents would be expected to create complete D^o - $\bar{D}^o$ mixing. Hence this observation implies that neutral currents conserve charm as well as strangeness.

APPENDIX I: Modeling the Time-of-Flight Tagging Algorithm

We wish to model the efficiency and effectiveness of the time-of-flight tagging algorithm described in the text. We begin by computing the probability that a kaon is tagged as a kaon as a function of kaon momentum. The kaon will be tagged as a pion if either time-of-flight information is missing or it has a flight time more consistent with the pion rather than the kaon mass hypothesis. We denote the probability of no-time-of-flight as $P_{\overline{TOF}}$, and the probability of time-of-flight inconsistency as P_{inc}, then: $P_{K,K} = 1 - P_{TOF} - P_{inc} + P_{\overline{TOF}} P_{inc}$ (1)

where $P_{K,K}$ is the probability that a K is tagged as a K.

Assuming flight times are normally distributed with resolution ($\sigma \simeq .45$ ns), we compute P_{inc} for kaons of momentum p as:

$$P_{inc} = \frac{1}{2} \left[1 - erf\left(\frac{T_K - T_\pi}{2\sqrt{2}\,\sigma} \right) \right] \tag{2}$$

where:

$$erf(x) = \frac{2}{\sqrt{\pi}} \int_0^x e^{-y^2} dy$$

and

$$T_{\pi,K} = \frac{5.5\ ns}{P} \sqrt{P^2 + M^2_{\pi,K}}\ .$$

The value 5.5 ns is the polar averaged flight time for high momentum prongs.

Time-of-flight information may be missing because of intrinsic counter inefficiency or inefficiency due to kaon decay. Hence

$$P_{\overline{TOF}} = D + (1-\epsilon) - D(1-\epsilon) \tag{3}$$

where $D = 1 - \exp[-R_c/(7.5p)]$ (using notation developed on the section describing the simulation program, $R_c = 1$ m) and ε is the trigger counter efficiency ($\varepsilon = .90$). The solid curve of Figure 1 of chapter 3 is computed from eqn. (1) with eqns. (2) and (3).

We turn to the modeling of the probability that a pion of momentum p will be tagged as a kaon ($P_{\pi,K}$). This can occur if timing information is present and seems to be more consistent with the kaon rather than pion hypothesis. Hence:

$$P_{\pi,K} = \varepsilon P_{inc} \tag{4}$$

where P_{inc} is again computed from eqn. (2). This function is shown as the dashed curve of Figure 1.

APPENDIX II. Derivation of Angular Distributions

Used in This Thesis

The purpose of this appendix is to derive the angular production and
decay distributions alluded to throughout this thesis. The results we
obtain here have application in the study of threshold charm meson
production via the process $e^+e^- \to D\,D^* + \bar{D}\,D^*$ where D^*'s can cascade to
D's via pion or γ emission. The general problem addressed here is the
production of a vector (V) and pseudoscalar (P_1) final state by e^+e^-
annihilation, with the vector decaying into a new pseudoscalar (P_2) by
pion or γ emission. We indicate this sequence of processes with the
diagram:
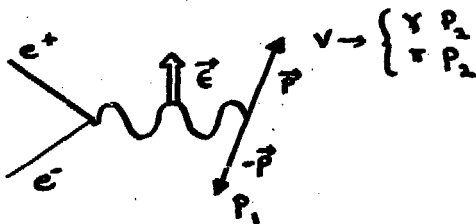
These results will hold equally well if the parity of V, P_1, and P_2 are
reversed. We will assume parity conservation at the production vertex
and in the radiative decay process. It will be unnecessary to assume
parity conservation for the pion decay process. We shall compute these
angular distributions by constructing rotationally invariant, non-relativ-
istic amplitudes in terms of the available vectors at each vertex. A
non-relativistic treatment whould be valid for charm production near
threshold (E_{cm} = 4.028 GeV) where the velocity of the D^* is approximately

0.3 c. All expressions computed by this technique can also be obtained by the use of pure angular momentum arguments using the helicity formalism.

We begin by introducing some notation for our general problem. Let:

$\hat{z}$ = the direction of the positron momentum along the annihilation axis (unit vector).

$\vec{\varepsilon}$ = transverse polarization vector of the timelike, virtual photon.

$\hat{p}$ = direction of the vector particle momentum in the overall CM frame (unit vector).

$\vec{S}$ = Cartesian representation of the vector particle's spin (i.e.

$$\vec{S} = [(J_x + iJ_y)/\sqrt{2} , (J_x - iJ_y)/\sqrt{2} , J_z]).$$

$\hat{q}$ = direction of the second pseudoscalar in the vector particle's rest frame (unit vector).

and if needed

$\vec{\varepsilon}$ = transverse polarization of the final state, real photon.

We are assuming, as discussed in Chapter   that $e^+e^- \to \,!\, V$ proceeds via a single, timelike, transverse photon.

1. Construction of the Production and Decay Amplitudes

We wish to construct our production amplitude out of the three 3-vectors $\hat{p}$, $\vec{\varepsilon}$, and $\vec{S}$. We require that the amplitude be rotationally invariant (i.e. scalar or pseudoscalar) and be linear in the fields of the timelike photon, pseudoscalar, and vector particle. This linearity requirement is naturally fulfilled in amplitudes deduced from a field theoretic Lagrangian, and operationally means our amplitude be linear in $\vec{S}$ and $\vec{\varepsilon}$. These considerations restrict the production amplitude to the three forms:

$$\hat{p} \cdot \vec{\varepsilon} \times \vec{S} \qquad\qquad \vec{\varepsilon} \cdot \vec{S} \qquad\qquad (\hat{p} \cdot \vec{\varepsilon})(\hat{p} \cdot \vec{S})$$

(Forms such as $\hat{P} \cdot \vec{\epsilon}$ or $\hat{P} \cdot \vec{S}$ are not linear in both $\vec{\epsilon}$ and $\vec{S}$.) Parity conservation applied at the production vertex implies that our amplitudes do not change signs under the transformation: $\hat{P} \to -\hat{P}$, $\vec{\epsilon} \to -\vec{\epsilon}$, $\vec{S} \to \vec{S}$, which leaves the unique amplitude: $\hat{P} \cdot \vec{\epsilon} \times \vec{S}$.

Identical considerations apply to the $V \to \gamma P_2$ decay amplitude which must be of the analogous form $\hat{q} \cdot \vec{\epsilon}' \times \vec{S}$. The linearity condition applied to the amplitude for $V \to \pi P$ requires a form proportional to $\vec{S}$. The only other vector around is $\hat{q}$, hence the decay amplitude must be of the form $\hat{q} \cdot \vec{S}$ irrespective of parity considerations. We thus obtain joint production and decay amplitudes given by:

$$M_{joint} \propto \begin{array}{ll} \hat{P} \cdot \vec{\epsilon} \times \vec{S} \;\; \vec{S} \cdot \hat{q} & \text{for } V \to \pi P \\ \hat{P} \cdot \vec{\epsilon} \times \vec{S} \;\; \hat{q} \cdot \vec{\epsilon}' \times \vec{S} & \text{for } V \to \gamma P. \end{array}$$

To average conveniently over the observed spin of the vector particle, we cyclically permute the triple scalar products and obtain:

$$M \propto \begin{array}{l} [\hat{P} \times \epsilon]^{\alpha} \; \langle \vec{S}^{\alpha} \vec{S}^{\beta} \rangle \; \hat{q}^{\beta} \\ [\hat{P} \times \vec{\epsilon}]^{\alpha} \; \langle \vec{S}^{\alpha} \vec{S}^{\beta} \rangle \; [\hat{q} \times \vec{\epsilon}']^{\beta} \end{array}$$

where averaging is denoted by the angle brackets ($\langle\,\rangle$), α and β run from 1 to 3 and refer to vector components, and we use the convention that repeated indices imply summation. For massive vector particles, this spin average is independent of the vector particle's momentum and hence of the form: $\langle S^{\alpha} S^{\beta} \rangle \propto \delta^{\alpha\beta}$. Thus:

$$M \propto \begin{array}{lll} \hat{P} \times \vec{\epsilon} \cdot \hat{q} & \text{(eqn. A1)} & \text{for } V \to \pi P_2 \\ \hat{P} \times \vec{\epsilon} \cdot \hat{q} \times \vec{\epsilon}' & \text{(eqn. A2)} & \text{for } V \to \gamma P_2. \end{array}$$

In order to compute angular distributions for production by unpolarized electron and positron annihilation we will need to average (actually sum) over $\vec{\epsilon}$. In the SPEAR Detector there is no way to monitor photon polarization; hence we will average over $\vec{\epsilon}'$ as well.

2. Photon Polarization Averaging

The photon polarization summation technique involves use of the quantity $\langle \epsilon^\alpha \epsilon^\beta \rangle$. This quantity is a tensor which can only depend on the photon momentum (k) and hence is of the form $\overline{\epsilon^\alpha \epsilon^\beta} \equiv T_k^{\alpha\beta} = A\delta^{\alpha\infty} + B\vec{k}^\alpha \vec{k}^\beta$. Any overall multiplicative factors in $T_k^{\alpha\beta}$ are irrelevant for our analysis; hence we arbitrarily set A = 1. The transversality condition $\vec{k}^\alpha \vec{\epsilon}^\alpha = 0$ implies $\vec{k}^\alpha \vec{T}^{\alpha\beta} = 0$ or $[1 + B\vec{k} \cdot \vec{K}]K^\beta = 0$. Thus $T_R^{\alpha\beta} = \delta^{\alpha\beta} - \hat{k}^\alpha \hat{k}^\beta$ where $\hat{k} = \vec{k}/|\vec{k}|$.

3. The Angular Distribution for $e^+e^- \rightarrow P_1 V; V \rightarrow \pi P_2$

We begin with the simple case first. Squaring eqn. (A1) and averaging over $\vec{\epsilon}$, we obtain:

$$|M|^2 = \langle (\hat{P} \times \vec{\epsilon} \cdot \hat{q})^2 \rangle$$
$$= [\hat{P} \times \hat{q}]^\alpha \langle \epsilon^\alpha \epsilon^\beta \rangle [\hat{P} \times \hat{q}]^\beta$$
$$= [\hat{P} \times \hat{q}]^\alpha T_z^{\alpha\beta} [\hat{P} \times \hat{q}]^\beta.$$

This last step follows from the fact that $\vec{\epsilon}$ is transverse to the e^+e^- annihilation axis. Using the expression for $T_z^{\alpha\beta}$ obtained in the last section we find:

$$|M|^2 = [\hat{P} \times \hat{q}^{\,\alpha}][\delta^{\alpha\beta} - \hat{z}^\alpha \hat{q}^\beta] [\hat{P} \times \hat{q}]^\beta$$
$$= |\hat{P} \times \hat{q}|^2 - |\hat{z} \cdot \hat{P} \times \hat{q}|^2.$$

It is useful to express the above expression in terms of the 3 production and decay angles θ and (θ, ϕ), where θ is the $\hat{P}$ polar angle and (θ, ϕ) are the $\hat{q}$ spherical angles in the vector particle's helicity frame. We orientate the helicity frame with its polar axis (z' axis) along the vector particle's momentum and its x' axis along the reaction plane normal (such that $\hat{x}' = \hat{z} \times \hat{P}$). By direct computation we find:

$$\frac{d^3\sigma}{d\cos\theta \; d\cos\theta \; d\phi} \propto |M|^2 \; [\sin^2\theta \; [\cos^2\phi + \cos^2\theta \; \sin^2\phi]. \qquad \text{eqn. A3}$$

This distribution is appropriate to the process $e^+e^- \to DD^*$; $D^* \to \pi D$ where the D is a pseudoscalar and the D^* is a vector as expected and demonstrated in Chapter   This result is used in Chapter   for the proper simulation of the D^0 momentum spectrum for D's produced via that two step process. The same distribution is also used in Chapter   for the process $e^+e^- \to \bar{D}^*D$; $D \to K\pi$ for vector D's and pseudoscalar D^*'s in order to rule out this spin-parity assignment.

4. The Angular Distribution for the Process $e^+e^- \to P_1V$; $V - \gamma P_2$

We begin with a few manipulations of eqn. (A2):

$$M \propto \hat{P} \times \vec{\epsilon} \cdot \hat{q} \times \vec{\epsilon}' = (\hat{P} \cdot \hat{q})(\vec{\epsilon} \cdot \vec{\epsilon}) - (\hat{P} \cdot \vec{\epsilon}')(\hat{q} \cdot \vec{\epsilon}).$$

Squaring and writing out selected dot products in terms of repeated indices, we obtain:

$$|M|^2 \propto (\hat{P} \cdot \hat{q})^2(\vec{\epsilon}^i \; \vec{\epsilon}'^i)(\epsilon^j \; \epsilon'^j) - 2\hat{P} \cdot \hat{q}(\vec{\epsilon}^i \; \vec{\epsilon}'^i)(\hat{P}^j \; \vec{\epsilon}'^j)(\hat{q}^k \; \vec{\epsilon}^k)$$
$$+ (\hat{P}^i \; \vec{\epsilon}'^i)(\hat{P}^j \; \vec{\epsilon}'^j)(\hat{q}^k \; \vec{\epsilon}^k)(\hat{q}^\ell \; \vec{\epsilon}^\ell).$$

Averaging over $\vec{\epsilon}$ and $\vec{\epsilon}'$ and noting that $\vec{\epsilon}'$ is transverse to the q axis, we find:

$$|M|^2 \propto (\hat{P} \cdot \hat{q})^2 \, T_z^{ij} \, T_q^{ij} - 2\hat{P} \cdot \hat{q} \, P^j \, T_q^{ji} \, T_z^{ik} \, q^k$$

$$+ (P^i \, T_q^{ij} \, P^j)(q^k \, T_z^{k\ell} \, q^\ell).$$

Inserting our forms for the tensors T_z^{ij} and T_q^{ij} and simplifying gives the expression:

$$|M|^2 \propto 1 - (\hat{z} \cdot \hat{q})^2 + 2(\hat{P} \cdot \hat{q})(\hat{z} \cdot \hat{q})(\hat{z} \cdot \hat{P}).$$

This expression can be written as:

$$\frac{d^3\sigma}{d\cos\theta \; d\cos\Theta \; d\phi} \propto 1 + \cos^2\theta \, \cos^2\Theta - \cos^2\phi \, \sin^2\theta \, \sin^2\Theta. \qquad \text{eqn. A4}$$

Eqn. (A4) is obviously appropriate to the process $e^+e^- \rightarrow \bar{D}D^*$; $D^* \rightarrow \gamma D$.

REFERENCES

Abrams, G. S. et al., 1974, Phys. Rev. Lett. **33**, 1453.

Altarelli, G., Cabibbo, N., and Maiani, L., 1975, Phys. Rev. Lett. **35**, 635.

Aubert, J. J. et al., 1974, Phys. Rev. Lett. **33**, 1404.

Augustin, J.-E. et al., 1974, Phys. Rev. Lett. **33**, 1406.

Barish, B. et al., 1975, Phys. Rev. Lett. **36**, 939.

Benvenuti, A. et al., 1975, Phys. Rev. Lett. **34**, 419.

Biddick, C. J. et al., 1977, Phys. Rev. Lett. **38**, 1324.

Blietschau, J. et al., 1976, Phys. Lett. **60B**, 207.

Boyarski, A. B. et al., 1975, Phys. Rev. Lett. **34**, 1357.

Brochard, S. and Mathur, V., 1976, Phys. Rev. Lett. **36**, 1287.

Cabibbo, N. and Gatto, R., 1961, Phys. Rev. **124**, 1577.

Cazzoli, E. G. et al., 1975, Phys. Rev. Lett. **34**, 1125.

Cline, D., 1977, Annual Reviews of Nuclear Science (to be published).

Close, F. E., 1976, Phys. Lett. **65B**, 55.

Commins, E., 1973, Weak Interactions (McGraw-Hill, Inc., New York), p. 81.

De Rujula, A., Georgi, H., and Glashow, S. L., 1976a, Phys. Rev. Lett. **37**, 398.

De Rujula, A., 1976b, XVIII International Conference on High Energy Physics, Tbilisi, U.S.S.R.

De Rujula, A., Georgi, H., and Glashow, S. L., 1977, Phys. Rev. Lett. **38**, 317.

Feldman, G. et al., 1977, Phys. Rev. Lett. **38**, 1313.

Friedman, J., 1971, Journal of Computational Physics **7**, 201.

Gaillard, M. K., Lee, B., and Rosner, J., 1975, Rev. Mod. Phys. **47**, 277.

Glashow, S. L., Iliopoulos, J., and Maiani, L., 1970, Phys. Rev. **D2**, 1285.

Goldhaber, G., et al., 1976, Phys. Rev. Lett. 37, 255.

Hollebeek, R., 1975, Lawrence Berkeley Laboratory publication no. LBL-3874,
   Ph.D. thesis.

Jackson, J. D., 1976, Proceedings of Summer Institute on Particle Physics,
   SLAC report no. 198, 147.

Jean-Marie, B. et al., 1976, Phys. Rev. Lett. 36, 291.

Kingsly, R. L., 1976, Phys. Lett. 63B, 329.

Knapp, B. et al., 1976, Phys. Rev. Lett. 37, 882.

Lane, K. and Eichten, 1976, Phys. Rev. Lett. 37, 477.

Lüth, V. et al., 1975, Phys. Rev. Lett. 35, 1.24.

Lüth, V., 1977, Phys. Lett. (to be publis'ed).

Niu, K. et al., 1971, Prog. Theor. Phys. 46, 1644.

Ono, S., 1976, Phys. Rev. Lett. 37, 655.

Perl, M. et al., 1976, Phys. Lett. 63B, 466.

Piccolo, M. et al., 1977, submitted to Phys. Lett.

Schwitters, R. and Strauch, K., 1975, Annual Reviews of Nuclear Science,
   (Palo Alto, California, Annual Reviews, Inc.), p. 89.

Siegrist, J. et al., 1976, Phys. Rev. Lett. 36, 700.

Stevenson, M. L. et al., 1962, Phys. Rev. 125, 687.

Suzuki, M., 1976, Phys. Rev. Lett. 37, 1164.

Trilling, G., 1976, Proceedings of Summer Institute on Particle Physics,
   SLAC report no. 198, 437.

Vanucci, F. et al., 1977, Phys. Rev. D15, 1814.

von Krogh, J. et al., 1976, Phys. Rev. Lett. 36, 710.

Weinberg, S. and Glashow, S., 1977, Phys. Rev. D15, 1958.

Weinberg, S., 1967, Phys. Rev. Lett. 19, 1264.

Whitaker, J., 1976, Lawrence Berkeley Laboratory publication no. LBL-5518,

    Ph.D. thesis.

Zemach, C., 1974, Phys. Rev. B133, 1201.

Zipse, J., 1976, Lawrence Berkeley Laboratory publication no. LBL-4281,

    Ph.D. thesis.